RL-TR-95-159
In-House Report
June 1995

EFFICIENT SOLUTION FOR ELECTROMAGNETIC SCATTERING USING THE DUAL-SURFACE MAGNETIC-FIELD INTEGRAL EQUATION FOR BODIES OF REVOLUTION

James L. Schmitz

19960529 081

**Rome Laboratory
Air Force Materiel Command
Griffiss Air Force Base, New York**

DTIC QUALITY INSPECTED 1

DISCLAIMER NOTICE
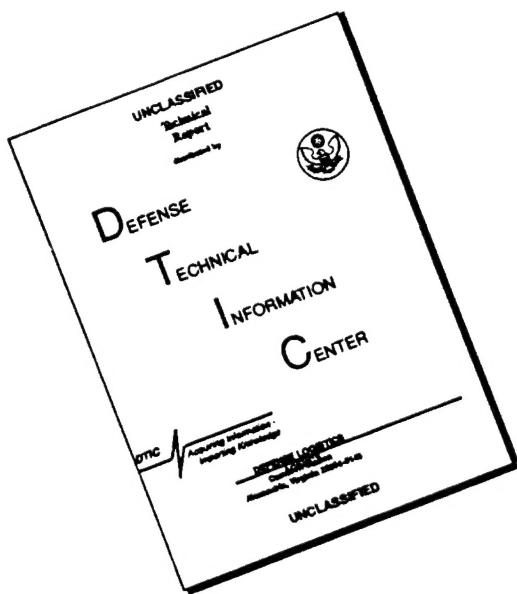
This report has been reviewed by the Rome Laboratory Public Affairs Office (PA) and is releasable to the National Technical Information Service (NTIS). At NTIS it will be releasable to the general public, including foreign nations.

RL-TR-95-159 has been reviewed and is approved for publication.

APPROVED:

JOHN F. LENNON
Acting Chief, Applied EM Division
Electromagnetic & Reliability Directorate

FOR THE COMMANDER:
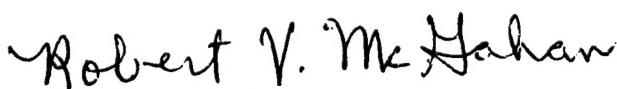
ROBERT V. McGAHAN
Acting Director
Electromagnetic & Reliability Directorate

1. AGENCY USE ONLY (Leave blank)	2. REPORT DATE June 1995	3. REPORT TYPE AND DATES COVERED In-house Report Sep 93 to Mar 94

4. TITLE AND SUBTITLE

Efficient Solution for Electromagnetic Scattering Using the Dual-Surface Magnetic-Field Integral Equation for Bodies of Revolution

5. FUNDING NUMBERS

PE - 61102F
PR - 2304
TA - I4
WU -02

6. AUTHOR(S)

Schmitz, James L.

7. PERFORMING ORGANIZATION NAME(S) AND ADDRESS(ES)

Rome Laboratory/ERCS
31 Grenier St
Hanscom AFB, MA 01731-3010

8. PERFORMING ORGANIZATION REPORT NUMBER

RL-TR-95-159

9. SPONSORING / MONITORING AGENCY NAME(S) AND ADDRESS(ES)

10. SPONSORING / MONITORING AGENCY REPORT NUMBER

11. SUPPLEMENTARY NOTES

12a. DISTRIBUTION / AVAILABILITY STATEMENT

Approved for Public Release; Distribution Unlimited.

12b. DISTRIBUTION CODE

13. ABSTRACT (Maximum 200 words)

The dual-surface magnetic-field integral equation (DMFIE) eliminates the spurious resonances from the magnetic-field integral equation (MFIE) for plane-wave scattering from bodies of revolution. The numerical predictions of scattering from a right circular cylinder were excellent using as little as seven segments per wavelength and simple pulse-basis and impulse-testing functions.

The total solution time for electrically large bodies is reduced dramatically using the FFT and conjugate gradient (CG) method. The solution times using Gaussian elimination were proportional to $(d/\lambda)^3$ for axial incidence for a scatterer of equal width and length, d, and proportional to $(d/\lambda)^4$ at broadside incidence. For broadside incidence, matrix-fill time was reduced using the FFT to a $(d/\lambda)^3 \log_2(d/\lambda)$ functional dependence, and CG reduced the solution time to $(d/\lambda)^3$. Therefore, the total CPU time for electrically large bodies of revolution is proportional to $(d/\lambda)^3$ for axial incidence and $(d/\lambda)^3 \log_2(d/\lambda)$ for broadside incidence.

The MFIE and the original DMFIE do not correctly produce the dominant current for scatterers with narrow tips, and these equations yielded incorrect results for bodies with these features. In coding the exact solution to scattering from the tip of an infinite cone into the computer program, the DMFIE was shown to calculate scattering from bodies with narrow tips accurately.

14. SUBJECT TERMS

Radar cross section   Bistatic RCS   Surface integral equations
Dual-surface integral equations   Bodies of revolution   Scattering

15. NUMBER OF PAGES 76

16. PRICE CODE

17. SECURITY CLASSIFICATION OF REPORT UNCLASSIFIED	18. SECURITY CLASSIFICATION OF THIS PAGE UNCLASSIFIED	19. SECURITY CLASSIFICATION OF ABSTRACT UNCLASSIFIED	20. LIMITATION OF ABSTRACT SAR

Contents

Illustrations

Acknowledgements

Efficient Solution For Electromagnetic Scattering Using the Dual-Surface Magnetic-Field Integral Equation For Bodies of Revolution

1   INTRODUCTION

Conventional solutions of the magnetic-field integral equation (MFIE) fail to produce a unique solution at frequencies equal to the resonant frequencies of the interior cavity.[1,2] These spurious resonances severely corrupt the numerical solution of the MFIE. Yaghjian[3] proved that the original MFIE allows spurious resonances at these frequencies because it does not restrict the tangential electric field to zero on the surface of the scatterer. Tobin, Yaghjian, and Bell(Woodworth)[4] derived the dual-surface magnetic-field integral equation (DMFIE) and applied it to a three-dimensional, multi-wavelength, perfectly conducting body. This numerical solution showed that the DMFIE did indeed eliminate the spurious resonances associated with the interior cavity modes. The proof of uniqueness and derivation for both the dual-surface electric-field integral equation (DEFIE) and magnetic-field integral equation appeared in Woodworth and Yaghjian.[5]

Mautz and Harrington[6] used the combined-field integral equation solution (CFIE) to eliminate the spurious resonances associated with the interior cavity modes. The CFIE,

[1] Murray, F.H. (1931) Conductors in an electromagnetic field, *Am. J. Math.*, **53**:275-288.

[2] Maue, A.W. (1949) On the formulation of a general scattering problem by means of an integral equation, *Zeitschrift fur Physik*, **126(7/9)**:601-618.

[3] Yaghjian, A.D. (1981) Augmented electric and magnetic field integral equation, *Radio Science*, **16**:987-1001.

[4] Tobin, A.R., Yaghjian, A.D., and Bell M.M. (1987) Surface integral equations for multi-wavelength, arbitrarily shaped, perfectly conducting bodies, *Digest of the National Radio Science Meeting*, (URSI), Boulder CO

[5] Woodworth, M.B., and Yaghjian, A.D. (1991) Derivation, application and conjugate gradient solution of the dual-surface integral equations for three-dimensional, multi-wavelength perfect conductors, in *PIERS-5: Applications of the Conjugate Gradient Method to Electromagnetic and Signal Analysis*, Sarkar, T.K. and Kong, J.A., eds., Elsevier, ch. 4. Also, *J. Opt. Soc. Am. A*, **11**, April 1994.

[6] Mautz, J.R. and Harrington, R.F. (1987) H-field, E-field, and combined-field solutions for bodies of revolution, *Arch. Elecktron. Ubertragungstech. (Electron. Commun.)*, **32(4)**:157-164.

as the name implies, combines the solution of the MFIE with the electric-field integral equation (EFIE). Because the CFIE involves the MFIE and the EFIE operators, additional programing ability and computer run-time are required than with the original MFIE.

One application of the CFIE and DMFIE solutions is plane wave scattering from a body of revolution. As an alternative to the CFIE, a body of revolution solution was formulated using the DMFIE to determine if it was advantageous to use because of increased accuracy or decreased computer run-time.[7] The body of revolution formulation of the DMFIE solution parallels the body of revolution formulation in Mautz and Harrington.[6] However, the numerical solution to the body of revolution DMFIE uses a single pulse and impulse approximation for basis and testing functions instead of the triangular basis and testing functions used in Mautz and Harrington.[6] The CFIE solution requires a more complicated set of basis and testing functions because it includes the EFIE. The different basis and testing functions are necessary to accurately model the derivative of the surface current in the EFIE which is not present in the MFIE. Also, summations for the integration use a simple rectangular rule rather than the more complex Gaussian quadrature integration scheme.

The purpose of this report is to present the development of the DMFIE for a perfectly conducting body of revolution and its capability for solving electrically large bodies using the fast Fourier transform (FFT) and conjugate gradient (CG) methods. Also presented is the implementation of the dominant tip current variation required to solve bodies with sharp tip-like structures (such as conespheres with half-cone angles less than 20°) using the MFIE and DMFIE. Results are presented with and without the FFT and CG methods. Comparisons of monostatic radar cross section for the original DMFIE, the DMFIE with modified dominant tip current implementation, and measurements are presented for various scatterers with tips.

2 STATEMENT OF PROBLEM

It is desired to determine the scattered far field from a perfectly conducting body of revolution excited by a plane wave. Figure 1 shows the geometry and the coordinate system used for the body of revolution, where ρ, ϕ, and z are the cylindrical coordinates and t and ϕ form an orthogonal curvilinear coordinate system on the body of revolution surface S. $\hat{u}_t$ and $\hat{u}_\phi$ are orthogonal unit vectors in the t and ϕ directions, respectively. Figure 2 shows the coordinate system for plane wave scattering. $\vec{k}_t$ is the propagation vector for the incident plane wave, θ_t defines the transmit angle, θ_r and ϕ_r are the receiver spherical angles at which the scattered far field is observed, and $\vec{k}_r$ is the receiver propagation vector, which points from the receiver location to the origin. $\vec{k}_t$ is limited to the xz-plane ($\phi_t = 0$). Figure 2 shows the unit vectors $\hat{u}_\theta^t$, $\hat{u}_\phi^t$, $\hat{u}_\theta^r$, and $\hat{u}_\phi^r$ in the θ_t, y, θ_r, and ϕ_r directions respectively. The notation follows basically that of Mautz and Harrington.[6]

Considered separately is an incident plane wave (H^θ) defined by

[7]Schmitz, J.L. (1991)*Dual-Surface Magnetic-Field Integral Solution for Bodies of Revolution*, RL-TR-91-139, Hanscom AFB, MA, ADA260725.
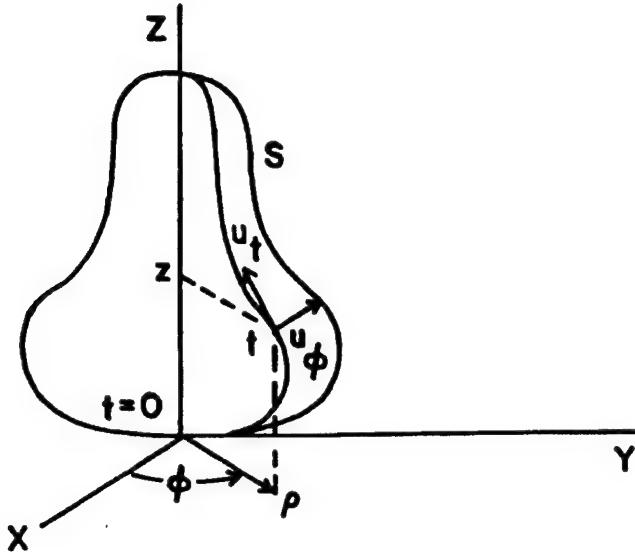
Figure 1. Body of Revolution and Coordinate System.

$$\vec{H}_{inc} = (\vec{k}_t \times \hat{u}_\phi^t)e^{-j\vec{k}_t \cdot \vec{r}} \tag{1}$$

and an incident plane wave (H^ϕ) defined by

$$\vec{H}_{inc} = (-\vec{k}_t \times \hat{u}_\theta^t)e^{-j\vec{k}_t \cdot \vec{r}} \tag{2}$$

where $\vec{H}_{inc}$ is the incident magnetic field, $\vec{r}$ is the position vector from the origin, k is the free space wavenumber, and the $e^{j\omega t}$ time dependence has been suppressed. The incident plane wave gives rise to electric currents directed in both the ϕ and t directions on the surface S as well as scattered far fields in the θ_r and ϕ_r directions.

3 MAGNETIC-FIELD INTEGRAL EQUATION

3.1 Formulation

Figure 3 illustrates an arbitrarily shaped perfectly conducting body with a plane wave incident on the body. By definition of the scattered magnetic field,

$$\vec{H}(\vec{r}) = \vec{H}_{sc} + \vec{H}_{inc}. \tag{3}$$

For the position vector $\vec{r}$ not on the surface S

3
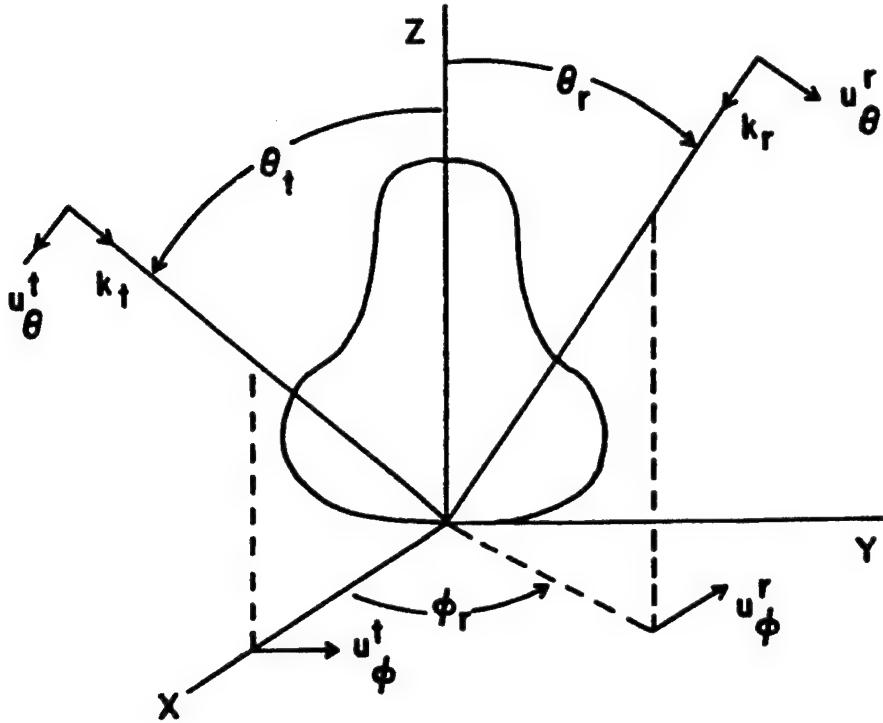
Figure 2. Plane Wave Scattering by a Conducting Body of Revolution.

$$\vec{H}_{sc}(\vec{r}) = \frac{1}{\mu_o} \nabla \times \vec{A}_{sc}(\vec{r}) \tag{4}$$

where

$$\vec{A}_{sc}(\vec{r}) = \frac{\mu_o}{4\pi} \int_S \frac{\vec{J}(\vec{r}')}{|\vec{r} - \vec{r}'|} e^{-jk|\vec{r} - \vec{r}'|} \, dS'. \tag{5}$$

Substituting for $\vec{A}_{sc}(\vec{r})$ in Eq. (5), the scattered magnetic field becomes

$$\vec{H}_{sc}(\vec{r}) = \frac{1}{4\pi} \int_S \vec{J}(\vec{r}') \times \nabla'\psi \, dS' \tag{6}$$

where

$$\psi = \frac{e^{-jk|\vec{r} - \vec{r}'|}}{|\vec{r} - \vec{r}'|}. \tag{7}$$

For $\vec{r}$ inside the sphere, $\vec{H}(\vec{r})$ equals zero, and thus

$$\vec{H}_{sc}(\vec{r}) = -\vec{H}_{inc}(\vec{r}). \tag{8}$$

Substituting $\vec{H}_{sc}(\vec{r})$ from Eq. (8) into Eq. (6) we obtain

4
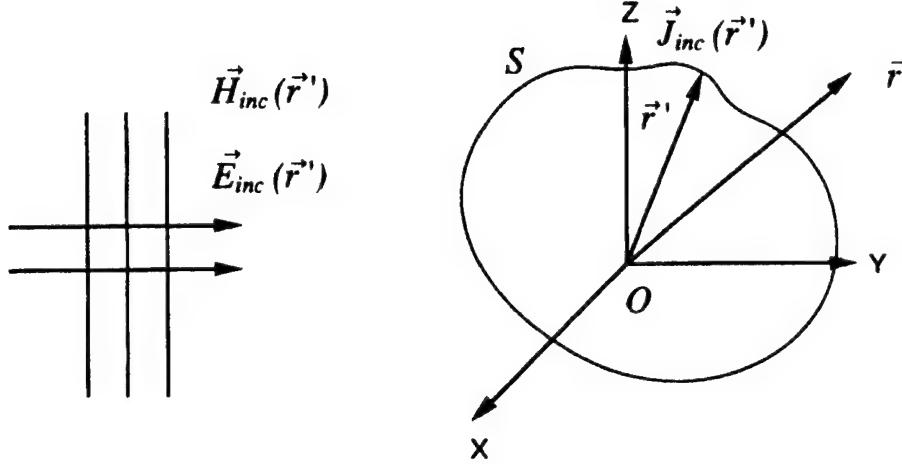
Figure 3. Geometry of Perfect Conductor for Plane Wave Scattering.

$$-\vec{H}_{inc}(\vec{r}) = \frac{1}{4\pi} \int_S \vec{J}(\vec{r}') \times \nabla'\psi \, dS' \quad (\vec{r} \text{ inside S}). \tag{9}$$

As $\vec{r}$ approaches S from inside the surface, Eq. (9) becomes[3]

$$\hat{n} \times \vec{H}_{inc}(\vec{r}) = \frac{\vec{J}(\vec{r})}{2} + \frac{1}{4\pi} \oint_S \left(\frac{1 + jk|\vec{r} - \vec{r}'|}{|\vec{r} - \vec{r}'|^3} \right) e^{-jk|\vec{r}-\vec{r}'|} \hat{n} \times [(\vec{r} - \vec{r}') \times \vec{J}(\vec{r}')] dS' \tag{10}$$

for $\vec{r}$ on S, where we have used the vector relationship

$$\vec{J}(\vec{r}') \times \nabla'\psi = -\left(\frac{1 + jk|\vec{r} - \vec{r}'|}{|\vec{r} - \vec{r}'|^3} \right) e^{-jk|\vec{r}-\vec{r}'|} (\vec{r} - \vec{r}') \times \vec{J}(\vec{r}'). \tag{11}$$

The outward normal $\hat{n}$ is defined as $\hat{n} = \hat{u}_\phi \times \hat{u}_t$. Using the notation in Reference 6 and letting

$$\vec{J}(\vec{r}') = \hat{u}'_t J^t(t', \phi') + \hat{u}'_\phi J^\phi(t', \phi') \tag{12}$$

where $\hat{u}'_t$ and $\hat{u}'_\phi$ are unit vectors in the t' and ϕ' directions respectively, Eq. (10) expands to

5

$$\hat{u}_t \left(\frac{J^t(t,\phi)}{2} + \frac{k^3}{4\pi} \int \rho' dt' \int_0^{2\pi} d\phi' G J^t(t',\phi'+\phi)\{[(\rho'-\rho)\cos v' \right.$$

$$- (z'-z)\sin v']\cos\phi' - 2\rho\cos v' \sin^2(\frac{\phi'}{2})\}$$

$$+ \frac{k^3}{4\pi} \int \rho' dt' \int_0^{2\pi} d\phi' G J^\phi(t',\phi'+\phi)(z'-z)\sin\phi' \Bigg)$$

$$+ \quad \hat{u}_\phi \left(\frac{J^\phi(t,\phi)}{2} + \frac{k^3}{4\pi}\rho' dt' \int_0^{2\pi} d\phi' G J^t(t',\phi'+\phi)\{[\rho'\sin v\cos v' \right. \tag{13}$$

$$- \rho\sin v'\cos v - (z'-z)\sin v\sin v']\sin\phi'\}$$

$$+ \frac{k^3}{4\pi} \int \phi' dt' \int_0^{2\pi} d\phi' G J^\phi(t',\phi'+\phi)\{[(\rho'-\rho)\cos v$$

$$- (z'-z)\sin v]\cos\phi' + 2\rho'\cos v\sin^2(\frac{\phi'}{2})\} \Bigg)$$

$$= \quad \hat{n} \times \vec{H}_{inc}$$

where

$$G = \frac{1+jkR}{k^3 R^3} e^{-jkR} \tag{14}$$

and

$$R = \sqrt{(\rho-\rho')^2 + (z-z')^2 + 4\rho\rho'\sin^2(\frac{\phi'}{2})}. \tag{15}$$

In Eq. (13), both $\hat{n}$ and $\vec{k}_t$ are to be evaluated on S at t and ϕ. The angle between $\hat{u}_t$ and the z-axis, v, is positive when $\hat{u}_t$ points away from the z-axis and is negative when $\hat{u}_t$ points toward the z-axis. The primed variables are functions of t' and therefore are evaluated at t'.

We want to take advantage of the geometry of the body of revolution by separating the ϕ and t dependence of $\vec{J}_t$ and $\vec{J}_\phi$. To accomplish this, $\vec{J}_t$ and $\vec{J}_\phi$ are expanded in a Fourier series in ϕ:

$$J^t(t,\phi) = \sum_{n=-\infty}^{\infty} j_n^t(t) e^{jn\phi} \tag{16}$$

$$J^\phi(t,\phi) = \sum_{n=-\infty}^{\infty} j_n^\phi(t) e^{jn\phi} \tag{17}$$

6

$$J^t(t', \phi' + \phi) = \sum_{n=-\infty}^{\infty} j_n^t(t') e^{jn(\phi'+\phi)} \tag{18}$$

$$J^\phi(t', \phi' + \phi) = \sum_{n=-\infty}^{\infty} j_n^\phi(t') e^{jn(\phi'+\phi)}. \tag{19}$$

The $\hat{u}_t$ and $\hat{u}_\phi$ components of Eq. (13) will be evaluated using the orthogonal properties of sinusoids and the following integral definition of Bessel functions.

$$J_m(x) = \frac{1}{2\pi j^m} \int_0^{2\pi} e^{jx\cos\phi - jm\phi} d\phi. \tag{20}$$

$$\text{for } m = 0, \pm 1, \pm 2, \ldots$$

Rewriting Eq. (13), we have for the $\hat{u}_t$ component of the H^θ incident plane wave

$$
\begin{aligned}
\frac{j_n^t(t)}{2} &+ \frac{k^3}{4\pi} \int dt' \rho' j_n^t(t') \int_0^{2\pi} d\phi' e^{jn\phi'} G\{[(\rho' - \rho)\cos v' \\
&- (z' - z)\sin v']\cos\phi' - 2\rho\cos v'\sin^2(\frac{\phi'}{2})\} \\
&+ \frac{k^3}{4\pi} \int dt' \rho' j_n^\phi(t') \int_0^{2\pi} d\phi' e^{jn\phi'} G(z' - z)\sin\phi' \\
&= -\frac{k}{2}\cos\theta_t e^{jkz\cos\theta_t} j^n [J_{n+1}(k\rho\sin\theta_t) + J_{n-1}(k\rho\sin\theta_t)]
\end{aligned}
\tag{21}
$$

and the $\hat{u}_\phi$ component

$$
\begin{aligned}
\frac{j_n^\phi(t)}{2} &+ \frac{k^3}{4\pi} \int dt' \rho' j_n^t(t') \int_0^{2\pi} d\phi' e^{jn\phi'} G[\rho'\sin v\cos v' \\
&- \rho\sin v'\cos v - (z' - z)\sin v\sin v']\sin\phi'\} \\
&+ \frac{k^3}{4\pi} \int dt' \rho' j_n^\phi(t') \int_0^{2\pi} d\phi' e^{jn\phi'} G\{[(\rho' - \rho)\cos v \\
&- (z' - z)\sin v]\cos\phi' + 2\rho'\cos v\sin^2(\frac{\phi'}{2})\} \\
&= ke^{jkz\cos\theta_t}\{2\pi\cos v\sin\theta_t j J_n(k\rho\sin\theta_t) - \\
&\qquad \sin v\cos\theta_t \pi j^{m+1}[J_{n+1}(k\rho\sin\theta_t) - J_{n+1}(k\rho\sin\theta_t)]\}.
\end{aligned}
\tag{22}
$$

For the H^ϕ incident wave we have for the $\hat{u}_t$ component

$$\frac{j_n^t(t)}{2} + \frac{k^3}{4\pi} \int dt' \rho' j_n^t(t') \int_0^{2\pi} d\phi' e^{jn\phi'} G\{[(\rho' - \rho)\cos v'$$

$$- (z' - z)\sin v']\cos\phi' - 2\rho\cos v' \sin^2(\frac{\phi'}{2})\}$$

$$+ \frac{k^3}{4\pi} \int dt' \rho' j_n^\phi(t') \int_0^{2\pi} d\phi' e^{jn\phi'} G(z' - z)\sin\phi'$$

$$= \frac{k}{2} e^{jkz\cos\theta_t} j^{n+1}[J_{n+1}(k\rho\sin\theta_t) - J_{n-1}(k\rho\sin\theta_t)]$$

$$\tag{23}$$

and for the $\hat{u}_\phi$ component

$$\frac{j_n^\phi}{2} + \frac{k^3}{4\pi} \int dt' \rho' j_n^t(t') \int_0^{2\pi} d\phi' e^{jn\phi'} G[\rho'\sin v\cos v'$$

$$- \rho\sin v'\cos v - (z' - z)\sin v\sin v']\sin\phi'$$

$$+ \frac{k^3}{4\pi} \int dt' \rho' j_n^\phi(t') \int_0^{2\pi} d\phi' e^{jn\phi'} G\{[(\rho' - \rho)\cos v$$

$$- (z' - z)\sin v]\cos\phi' + 2\rho'\cos v \sin^2(\frac{\phi'}{2})\}$$

$$= \frac{k}{2}\sin v\, e^{jkz\cos\theta_t}[j^{n-2} J_{n+1}(k\rho\sin\theta_t) - j^n J_{n-1}(k\rho\sin\theta_t)].$$

$$\tag{24}$$

The t' and ϕ' integrations can be converted to direct summations. With the t' integral divided into discrete segments, the value of the integrand is evaluated at the center of each segment and then summed over the number of t'-segments. The ϕ' integral is divided into small patches, again approximating the integrand at the center of each patch. In moment method terminology, this equates to using pulse basis functions and unit impulse testing functions. The well-behaved condition of the magnetic-field integral equation allows such simple basis and testing functions to be used.

Rewriting Eqs. (21) and (22) with the t' and ϕ' integrations represented as summations, we have

$$\frac{j_{nl}^t}{2} + \triangle t \sum_{\substack{m=1 \\ m\neq l}}^{M} K_n^{tt}(t_l, t_m) j_{nm}^t + \triangle t \sum_{\substack{m=1 \\ m\neq l}}^{M} K_n^{t\phi}(t_l, t_m) j_{nm}^\phi = S_n^t(t_l, \theta_t)$$

$$\tag{25}$$

$$\text{for } l = 1, 2, \ldots$$

and

8

$$\frac{j_{nl}^\phi}{2} + \triangle t \sum_{\substack{m=1 \\ m \neq l}}^{M} K_n^{\phi t}(t_l, t_m) j_{nm}^t + \triangle t \sum_{\substack{m=1 \\ m \neq l}}^{M} K_n^{\phi\phi}(t_l, t_m) j_{nm}^\phi = S_n^\phi(t_l, \theta_t) \tag{26}$$

$$\text{for } l = 1, 2, \ldots M$$

where n is the mode number, l is the number of the t-segment, and m the segment number for the t' integration. The first superscript indicates the direction of the current and the second superscript indicates the vector component. M is the maximum number of t- and t'-segments, and $\triangle t$ is the length of the t-segment.

For a given $t(l)$ and $t'(m)$ the only unknown quantities in Eqs. (25) and (26) are j_n^t and j_n^ϕ. Thus for a given n, t, and t', Eqs. (25) and (26) can be represented as

$$
\begin{bmatrix}
K_{11}^{tt} & \cdots & K_{1M}^{tt} & K_{11}^{t\phi} & \cdots & K_{1M}^{t\phi} \\
\vdots & \cdots & \vdots & \vdots & \cdots & \vdots \\
K_{M1}^{tt} & \cdots & K_{MM}^{tt} & K_{M1}^{t\phi} & \cdots & K_{MM}^{t\phi} \\
K_{11}^{\phi t} & \cdots & K_{1M}^{\phi t} & K_{11}^{\phi\phi} & \cdots & K_{1M}^{\phi\phi} \\
\vdots & \cdots & \vdots & \vdots & \cdots & \vdots \\
K_{M1}^{\phi t} & \cdots & K_{MM}^{\phi t} & K_{M1}^{\phi\phi} & \cdots & K_{MM}^{\phi\phi}
\end{bmatrix}
\begin{bmatrix}
j_1^t \\ \vdots \\ j_M^t \\ j_1^\phi \\ \vdots \\ j_M^\phi
\end{bmatrix}
=
\begin{bmatrix}
S_1^t \\ \vdots \\ S_M^t \\ S_1^\phi \\ \vdots \\ S_M^\phi
\end{bmatrix}
\tag{27}
$$

where K and S are known functions of t, t', ϕ', and t and θ_t, respectively and the $j's$ are the unknown Fourier series coefficients of the current.

The superscripts of the j and S variables indicate the vector component and the subscripts indicate the segment. This square matrix equation can be solved for j_n^t and j_n^ϕ for each n, and the currents can be found from j_n^t and j_n^ϕ by using Eqs. (16) to (19).

Evaluating the ϕ' integration in Eqs. (21) to (24) at $t = t'$ ($\rho = \rho'$ and $z = z'$) yields $R = 2\rho \sin(\phi'/2)$. Therefore, at $t = t'$, the phi integration does not converge. This lack of convergence is not due to the magnetic-field integral equation but to our separation of the ϕ' and t' integrations. To obtain convergence at $t = t'$, one must evaluate the $\phi't'$ area of integration more carefully. In Reference 7, it is shown that the ϕ' integration can be done properly, when the ϕ' integration is separated from the t' integration, if the modified Green's function

$$G = \frac{1}{k^3 R^2 R_c} + \frac{1}{k^3 R_a^3}[(1 + jkR_a)e^{-jkR_a} - 1] \tag{28}$$

replaces G in Eq. (14), where

$$R_c = \sqrt{(\triangle t/2)^2 + (\rho\phi')^2} \tag{29}$$

$$R_a = \sqrt{(\triangle t/2)^2/4 + (\rho\phi')^2} \tag{30}$$

and $\triangle t$ is the size of the t-segment.

3.2 Far Field

To obtain the scattered magnetic far field, let $r \gg r'$ in Eq. (6) to get

$$\vec{H}_{sc}(\vec{r}) = -\frac{jke^{jkr}}{4\pi r}\hat{r} \times \int_S \vec{J}(\vec{r}')e^{jk\hat{r}_r \cdot \vec{r}'}dS'. \tag{31}$$

Noting that

$$\hat{r} \times \hat{u}_\phi = -\cos(\phi - \phi')\hat{u}_\theta + \cos\theta\sin(\phi - \phi')\hat{u}_\phi \tag{32}$$

$$\hat{r} \times \hat{u}_t = \sin(\phi - \phi')\sin v'\hat{u}_\theta + \cos\theta\cos(\phi - \phi')\sin v'\hat{u}_\phi \tag{33}$$

$$\hat{r}_r \cdot \vec{r}' = \rho'\sin\theta_r\cos(\phi - \phi') + z'\cos\theta \tag{34}$$

allows Eq. (31) to be written as

$$H_{sc}^\theta(\vec{r}) = \frac{-jke^{jkr}}{4\pi r}\int_0^T \rho'dt'\int_0^{2\pi} d\phi'\{J^\phi(\phi', t')[-\cos(\phi - \phi')]$$
$$+ J^t(\phi', t')[\sin(\phi - \phi')\sin v']\}e^{jk[\rho'\sin\theta\cos(\phi - \phi') + z'\cos\theta]} \tag{35}$$

and

$$H_{sc}^\phi(\vec{r}) = \frac{-jke^{jkr}}{4\pi r}\int_0^T \rho'dt'\int_0^{2\pi} d\phi'\{J^\phi(\phi', t')[-\sin(\phi - \phi')\cos\theta]$$
$$+ J^t(\phi', t')[-\sin\theta\cos v' + \cos(\phi - \phi')\cos\theta\sin v']\} \tag{36}$$
$$e^{jk[\rho'\sin\theta\cos(\phi - \phi') + z'\cos\theta]}$$

where, according to Eqs., (16) and (17)

$$J^t(\phi', t') = \sum_{n=-\infty}^{\infty} j_n^t(t')e^{jn\phi'} \tag{37}$$

$$J^\phi(\phi', t') = \sum_{n=-\infty}^{\infty} j_n^\phi(t')e^{jn\phi'}. \tag{38}$$

The superscripts θ and ϕ in Eqs. (35) and (36) designate the component of the scattered field.

Substituting Eqs. (35) and (36) into Eq. (31) and using Eq. (20), Eq. (35) is rewritten as

10

$$H_{sc}^{\theta}(\vec{r}) = \frac{-jke^{jkr}}{4\pi r} \int_0^T \rho' dt' \sum_{n=-\infty}^{\infty} \left\{ j_n^{\phi}(t') e^{jn\phi} e^{jkz'\cos\theta} \pi j^{n+1} \right.$$

$$[J_{n+1}(k\rho'\sin\theta) - J_{n-1}(k\rho'\sin\theta)] + j_n^t(t') e^{jn\phi} e^{jkz'\cos\theta} \pi \sin v' j^n \qquad (39)$$

$$\left. [J_{n+1}(k\rho'\sin\theta) + J_{n-1}(k\rho'\sin\theta)] \right\}$$

and Eq. (36) as

$$H_{sc}^{\phi}(\vec{r}) = \frac{-jke^{jkr}}{4\pi r} \int_0^T \rho' dt' \sum_{n=-\infty}^{\infty} \left(j_n^{\phi}(t') e^{jn\phi} e^{jkz'\cos\theta} \pi \cos\theta j^n \right.$$

$$[J_{n+1}(k\rho'\sin\theta) - J_{n-1}(k\rho'\sin\theta)] \qquad (40)$$

$$+ j_n^t(t') e^{jn\phi} e^{jkz'\cos\theta} \pi j^n \{2\sin\theta\cos v' J_n(k\rho'\sin\theta) - \cos\theta\sin v' j$$

$$\left. [J_{n+1}(k\rho'\sin\theta) - J_{n-1}(k\rho'\sin\theta)]\} \right).$$

The radar cross section σ is defined as

$$\sigma = \lim_{r\to\infty} 4\pi r^2 \frac{|\vec{H}_{sc}|^2}{|\vec{H}_{inc}|^2} \qquad (41)$$

For a $\vec{H}_{\theta}$ incident wave Eq. (41) becomes

$$\sigma = \lim_{r\to\infty} 4\pi r^2 \frac{|H_{sc}^{\theta\theta}|^2 + |H_{sc}^{\theta\phi}|^2}{|\vec{H}_{inc}|^2} \qquad (42)$$

and for a $\vec{H}_{\phi}$ incident wave Eq. (41) becomes

$$\sigma = \lim_{r\to\infty} 4\pi r^2 \frac{|H_{sc}^{\phi\phi}|^2 + |H_{sc}^{\phi\theta}|^2}{|\vec{H}_{inc}|^2} \qquad (43)$$

where the first and second superscripts designate the components of the incident and scattered fields, respectively.

For the plane wave incident along the positive z-axis, only the ± 1 modes are needed in the Fourier series to represent $\vec{J}^t$ and $\vec{J}^{\phi}$. For an incident plane wave off the z-axis, the maximum number of modes $N_{\max}$ was chosen as

$$N_{\max} = (1.1kr\sin\theta_t + 2) \qquad (44)$$

where r is the maximum radius of the body of revolution measured from the z-axis.[8]

[8] Yaghjian, A.D. (1977) *Near Field Antenna Measurements on a Cylindrical Surface: A Source Scattering Matrix Formulation*, NBS Technical Note 696.
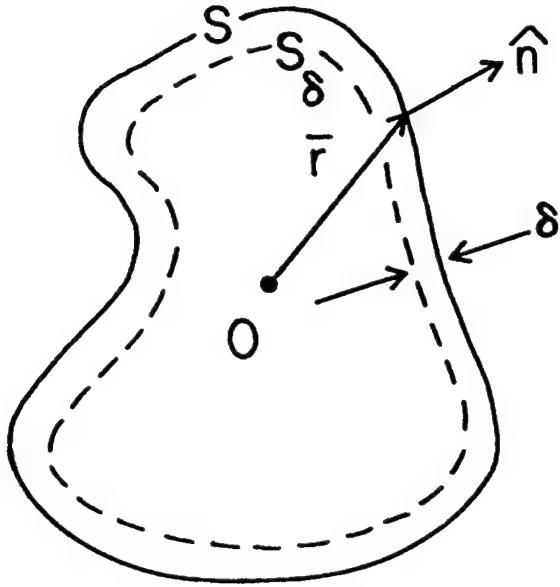
Figure 4. Geometry of Perfect Conductor for Dual-Surface Magnetic-Field Integral Equation.

Typically five to ten segments per wavelength are used for both the number of t-segments and phi-segments. The criterion for the number of phi-segments is based on having square patches for the phi integration. Other shaped patches were used, but the results proved most accurate for square or approximately square patches.

4 DUAL-SURFACE MAGNETIC-FIELD INTEGRAL EQUATION

4.1 Formulation

The following derivation of the DMFIE closely follows the work on the DMFIE presented by Woodworth and Yaghjian.[5] The DMFIE can be derived by beginning with Eq. (10), the "interior" or "extended" MFIE, which is rewritten here

$$-\vec{H}_{inc}(\vec{r}) = \frac{1}{4\pi} \int_S \vec{J}(\vec{r}') \times \nabla'\psi \, dS' \qquad (\vec{r} \quad \text{inside} \quad S). \qquad (45)$$

The current $\vec{J}(\vec{r})$ in Eq. (45) is uniquely determined at every frequency if Eq. (45) is satisfied for all $\vec{r}$ inside S.[9]

Figure 4 shows the surface S and a surface S_δ parallel to, and some distance $\delta > 0$, inside of S.

---

[9] Waterman, P.C. (1965) Matrix formulation of electromagnetic scattering, *Proc. IEEE*, **53**:805-812.

By adding $\alpha\hat{n}$ cross Eq. (64) at points $\vec{r}$ on S_δ to the corresponding points on S in the original MFIE, one obtains the DMFIE [5]:

$$\hat{n} \times \vec{H}_o(\vec{r}) = \frac{\vec{J}(\vec{r})}{2} - \hat{n} \times \frac{1}{4\pi} \oint_S \vec{J}(\vec{r}') \times \nabla'\psi_0(\vec{r}, \vec{r}')\, dS' \tag{46}$$

where

$$\vec{H}_0(\vec{r}) \equiv \vec{H}_{inc}(\vec{r}) + \alpha\vec{H}_{inc}(\vec{r} - \delta\hat{n}) \tag{47}$$

$$\psi_0(\vec{r}, \vec{r}') \equiv \psi(\vec{r}, \vec{r}') + \alpha\psi(\vec{r} - \delta\hat{n}, \vec{r}') \tag{48}$$

and, as usual

$$\psi = \frac{e^{-jk|\vec{r}-\vec{r}'|}}{|\vec{r} - \vec{r}'|}. \tag{49}$$

The DMFIE will have a unique solution for $\vec{J}$ at all real frequencies if α is imaginary and the positive real constant δ is less than approximately $\lambda/2$. For the body of revolution solution, α was chosen to be j $(\sqrt{-1})$, and δ was selected to equal $\lambda/4$.

The existing MFIE solution is easily modified to obtain the DMFIE. $\vec{H}_{inc}$ and ψ are now calculated at both the outer surface and an inner surface some distance δ inside. This requires that computer program be modified to simply evaluate these functions at $\vec{r} - \delta\hat{n}$ as well as at $\vec{r}$.

Figure 5 plots the normalized radar cross section, $\sigma/\pi a^2$, in the backscattering direction for a perfect electric conducting sphere as computed using the MFIE, the Mie series, and the DMFIE. The spurious resonances in the MFIE solution are eliminated by the DMFIE, which agrees well with the Mie series.

5 FFT AND CONJUGATE GRADIENT IMPLEMENTATION

5.1 FFT Method

As shown in Eqs. (21) to (24) the expansion of the current into a Fourier series allows the decoupling of the ϕ' and t' integrals in the integral equation, and allows the ϕ' integration to be performed for each term in the Fourier series. The ϕ' integration in Eqs. (21) to (24) can be rewritten as

$$\tilde{I}(n) = \int_0^{2\pi} A(t, t', \phi')Ge^{jn\phi'}d\phi' \tag{50}$$

where $A(t, t', \phi')$ is the portion of the equation independent of n. Eq. (50) has the form of a

13
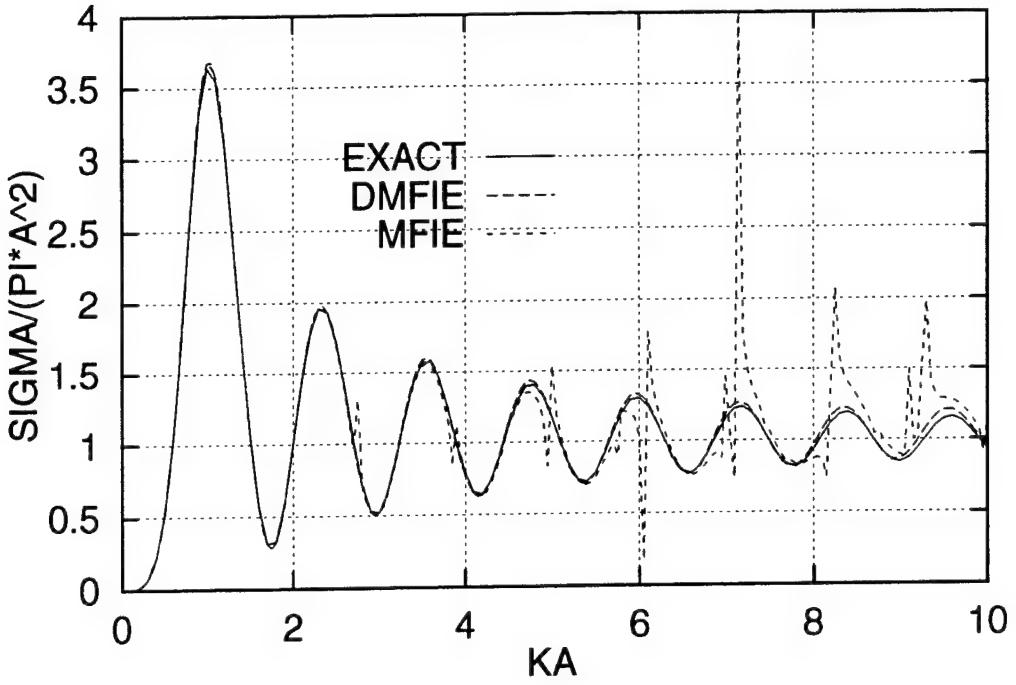
Figure 5. Backscattering Cross Section Versus ka of a PEC Sphere Computed with the Mie Series, MFIE, and DMFIE.

Fourier transform and can be computed efficiently using a FFT. [10] $\tilde{I}(n)$ must be computed at a discrete integer spacing of 1, (i,e. $n = 1, 2, 3, \ldots N_{\max}$) according to the criteria in Eq. (44), and so the FFT must be sampled at discrete intervals $\triangle\phi' = 2\pi/m$ where m is an integer. This allows the ϕ' integrations for all of the modes to be calculated simultaneously. The use of the FFT then reduces the computational time required to perform the integrations but increases the storage required to store the additional information. If the Fourier series requires M modes for convergence of the current, it is necessary to solve M systems of linear equations each with $2N$ unknowns.

5.2 Conjugate Gradient Method

The conjugate gradient iterative method is an efficient alternative to Gaussian elimination or LU decomposition for solving the large systems of linear equations, $A\mathcal{X} = \mathcal{Y}$. A version of the CG method, referred to as Case A by Sarkar and Arvas,[11] applies to a general square matrix A that is not defined to be symmetric, positive or negative definite. They start with an initial guess $\mathcal{X}_0$ and define

$$\mathcal{R}_0 = \mathcal{Y} - A\mathcal{X}_0 \tag{51}$$

[10] Gedney, S.D. and Mittra, R. (1990) The use of the FFT for the efficient solution of the problem of electromagnetic scattering by a body of revolution, *IEEE Trans. Antennas Propagat.*, **AP-38**:313-322.

[11] Sarkar, T.K., and Arvas, E. (1985) On a class of finite step iterative methods (conjugate directions) for the solution of an operator equation arising in electromagnetics, *IEEE Trans. Antennas Propagat.*, **AP-22**:1058-1066.

$$\mathcal{P}_0 = \mathcal{G}_0 = \mathcal{A}^*\mathcal{R}_0 \tag{52}$$

and iterate for $i = 1, 2, \ldots$:

$$a_i = \frac{||\mathcal{G}_{i-1}||^2}{||\mathcal{A}\mathcal{P}_{i-1}||^2} \tag{53}$$

$$\mathcal{X}_i = \mathcal{X}_{i-1} + a_i\mathcal{P}_{i-1} \tag{54}$$

$$\mathcal{R}_i = \mathcal{R}_{i-1} - a_i\mathcal{P}_{i-1} \tag{55}$$

$$\mathcal{G}_i = \mathcal{A}^*\mathcal{R}_i \tag{56}$$

$$b_i = \frac{||\mathcal{G}_i||^2}{||\mathcal{G}_{i-1}||^2} \tag{57}$$

$$\mathcal{P}_i = \mathcal{G}_i + b_i\mathcal{P}_{i-1} \tag{58}$$

where $||\mathcal{G}_0||^2 = \sum_j |c_j|^2$ is the inner product of a vector with itself and $|c_j|$ denotes the magnitude of the complex vector element c_j. The symbols $\mathcal{X}, \mathcal{Y}, \mathcal{R}, \mathcal{G}$, and $\mathcal{P}$ are vectors, a and b are scalars, and $\mathcal{A}^*$ denotes the Hermitian conjugate of the matrix $\mathcal{A}$. The CG method minimizes $||\mathcal{R}_i||^2$, where $\mathcal{R}_i$ is the residual vector, and gives a sequence of least square solutions ($\mathcal{X}_i$) to $\mathcal{A}\mathcal{X} = \mathcal{Y}$ such that the estimate $\mathcal{X}_i$ gets closer to $\mathcal{X}$ with each iteration. Iteration continues until the normalized residual error ($\epsilon \equiv ||\mathcal{R}_i||/||\mathcal{Y}||$) is reduced to a chosen value. For the stated problem, $\mathcal{X}$ is the vector of the unknown surface currents, $\mathcal{Y}$ is the vector of the incident field, and $\mathcal{A}$ matrix represents the operator on the right-hand side of Eq. (46).

The sequence $\mathcal{X}_i$ will converge to the exact solution $\mathcal{X}$ in a finite number of steps for any initial guess so long as the matrix is not singular and the round-off errors are negligible. An initial guess of $\mathcal{X}_0 = 0$, the null vector, was used. The use of the null vector allows the flexibility of stopping the iteration and restarting, using the current estimate of the solution as the new initial guess. Restarting eliminates round-off errors but requires an additional matrix multiplication, thus slowing convergence and increasing the solution run time.

The radar cross section of two right circular cylinders with equal diameter and length was computed using two different values of ϵ, 10^{-3} and 10^{-6}. The results, in Figures 6 and 7, show no difference in the radar cross section and so an $\epsilon = 10^{-3}$ was chosen as the cutoff value of the normalized residual.

As stated previously, the CG method in practice converges more rapidly than the theoretical limit of iterations. To demonstrate this for a body of revolution, the total number of iterations was divided by the total number of modes to obtain an average number of iterations for the problem solution. Figure 8 shows the slight increase in the average number of iterations required to compute the bistatic radar cross section of a right circular cylinder with the same diameter and length. This means that the total number of iterations required increases approximately linearly with electrical size of the cylinder.

15
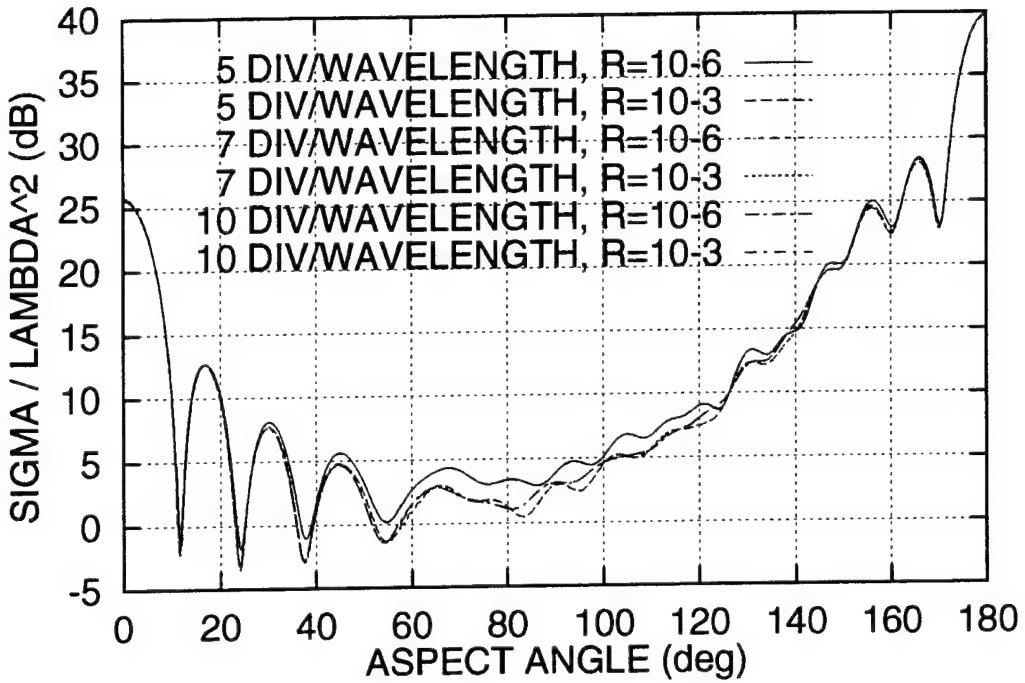
Figure 6. Bistatic Radar Cross Section of a 5λ by 5λ Right Circular Cylinder with Normalized Residual Error $= 10^{-3}$ and 10^{-6}; $\theta_t = 90°$.

The CG method was found to converge steadily for the well conditioned DMFIE body of revolution solution as seen in Figure 9.

5.3 Numerical Implementation

For axial incidence of the plane wave ($\theta_t = 0$ or $180°$), only the ± 1 Fourier modes are required. For an incidence angle of $0°$, the bistatic scattering of a $300\lambda \times 300\lambda$ right circular cylinder (6000 unknowns) was computed using Gaussian elimination to solve the set of linear equations for five segments per wavelength. The solution required 570 minutes of CPU time on the Cray C90 supercomputer and is shown in Figure 10. The size of the body was limited by the C90 queue restrictions, not the available RAM.

Off axis, the maximum number of Fourier modes m is given by Eq. (44). The number of unknowns N is proportional to d/λ, the electrical arc length along the generating curve. Using a right circular cylinder of equal length and width, for each m the matrix fill and solution times using Gaussian elimination are proportional to $(d/\lambda)^3$ For broadside incidence m is proportional to d/λ so the total matrix and fill solution times are proportional to $(d/\lambda)^4$. Using the FFT implementation discussed previously reduces the matrix fill time from a $(d/\lambda)^4$ to a $(d/\lambda)^3 \log_2(d/\lambda)$ functional dependence. The use of the CG iterative method allows one to reduce the $(d/\lambda)^4$ solution time to a $(d/\lambda)^3$ solution time. This means that the total computer time required for the body of revolution solution is asymptotically, for large d/λ, proportional to $(d/\lambda)^3$ for axial incidence and $(d/\lambda)^3 \log_2(d/\lambda)$ for broadside incidence. The FFT requires an increased amount of computer storage, but this is the

16
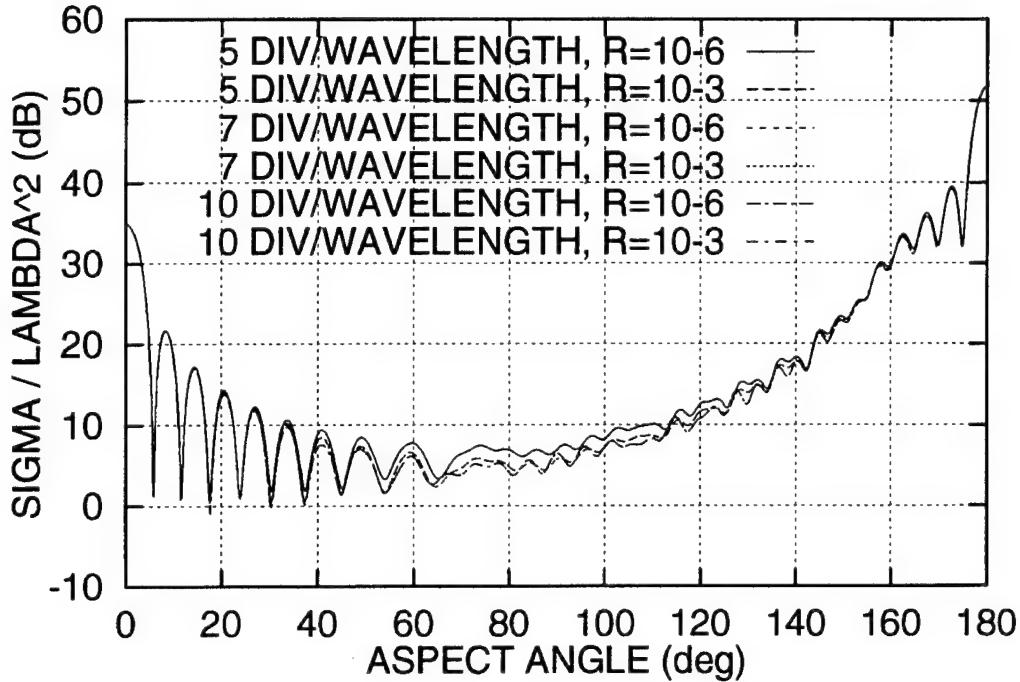
Figure 7. Bistatic Radar Cross Section of a 10λ by 10λ Right Circular Cylinder with Normalized Residual Error $= 10^{-3}$ and 10^{-6}; $\theta_t = 90°$.

trade-off one must tolerate to save computer time. The bistatic scattering of a $20\lambda \times 20\lambda$ right circular cylinder was computed at broadside incidence ($\theta_t = 90$ degrees). The size of the cylinder was limited by the available RAM on the Cray C90. The solution (Figure 11) required 10 minutes of CPU time for Gaussian elimination with no FFT, 3 minutes for Gaussian elimination with the FFT and approximately 2 minutes for the CG method with the FFT. Figure 12 shows the CPU time versus the cylinder radius for right circular cylinders with the same diameter and length using the FFT to decrease fill-time, CG to decrease solution time, and using strictly Gaussian elimination to reduce matrix solution time. The reduction of total solution time of electrically large bodies by the FFT and CG method is clearly demonstrated.
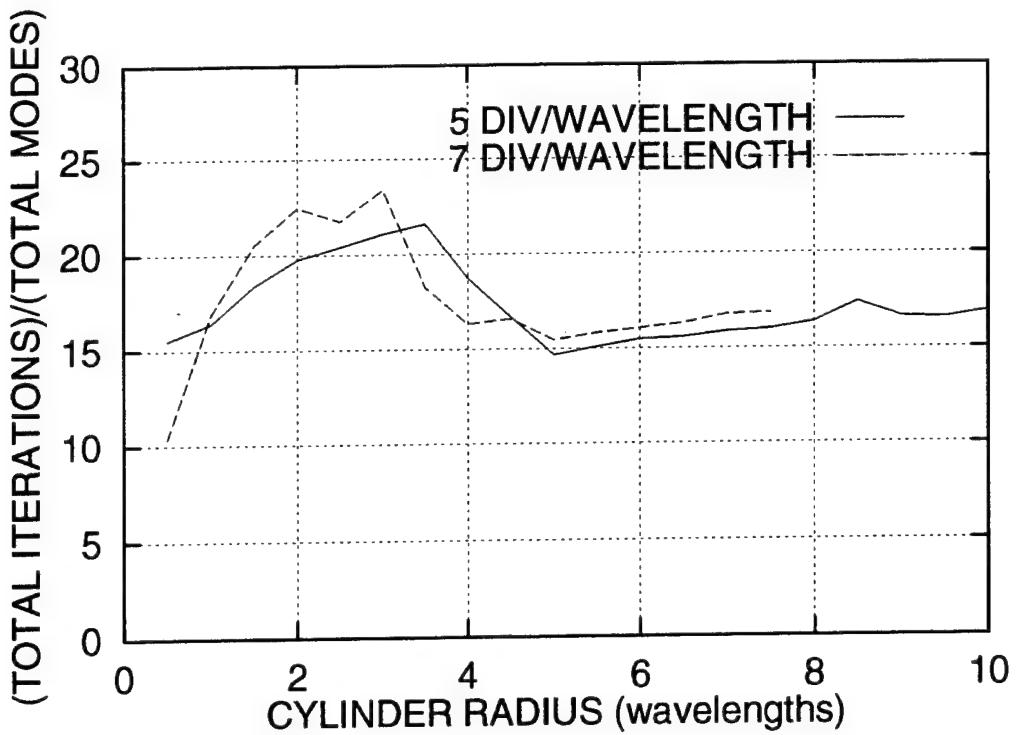
Figure 8. Comparison of the Average Number of Iterations Required for Solution of a Right Circular Cylinder for Five and Seven Divisions per Wavelength; $\theta_t = 90°$.
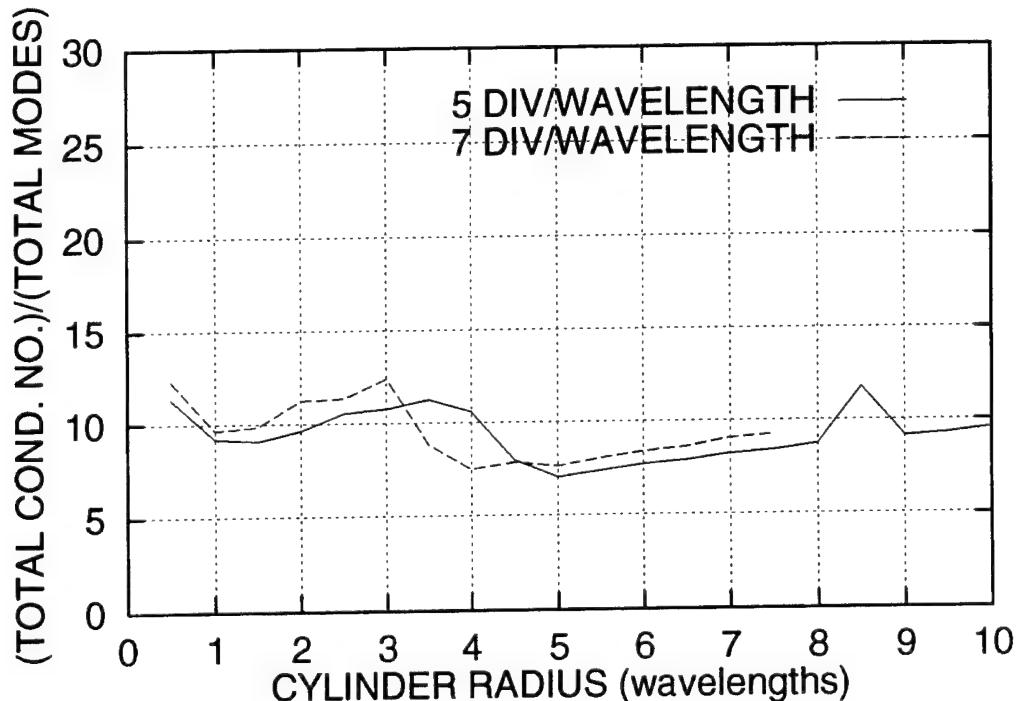
Figure 9. Condition Number versus Radius of a Right Circular Cylinder for Five and Seven Divisions per Wavelength; $\theta_t = 90°$.
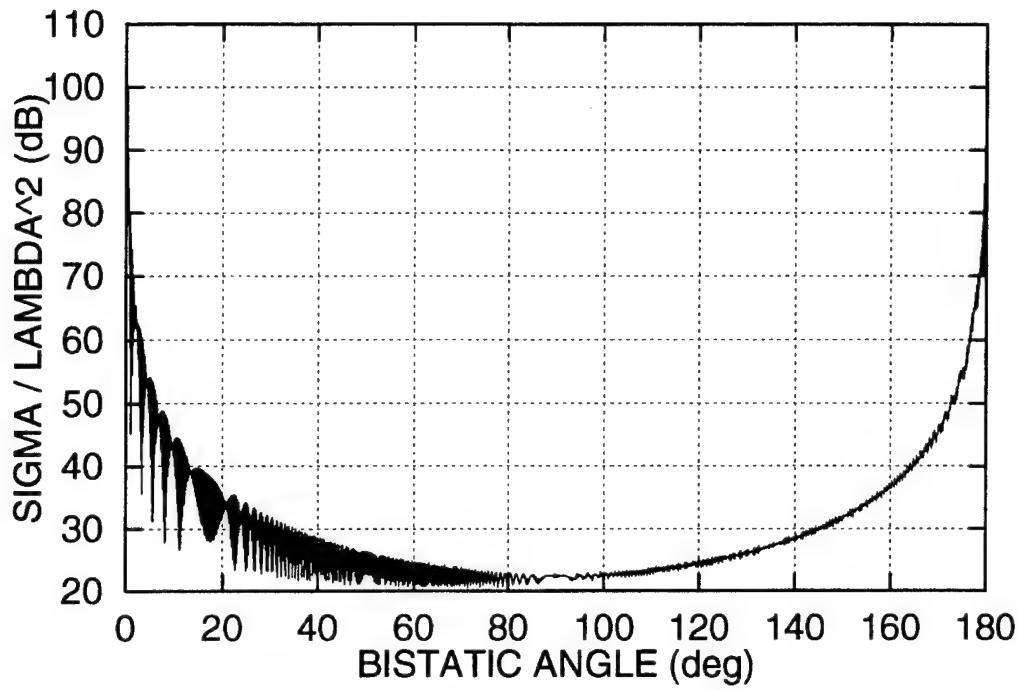
Figure 10. H-Plane Bistatic Radar Cross Section of a 300λ by 300λ Right Circular Cylinder with $\epsilon = 10^{-3}$; $\theta_t = 90°$.
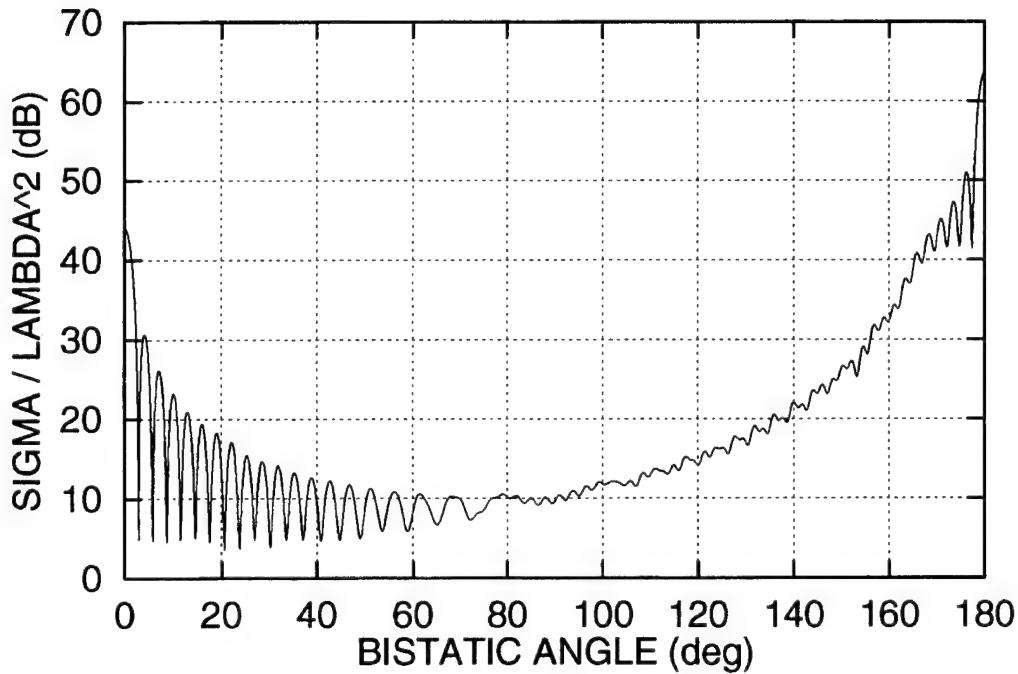
Figure 11. H-Plane Bistatic Radar Cross Section of a 20λ by 20λ Right Circular Cylinder with $\epsilon = 10^{-3}$; $\theta_t = 90°$.
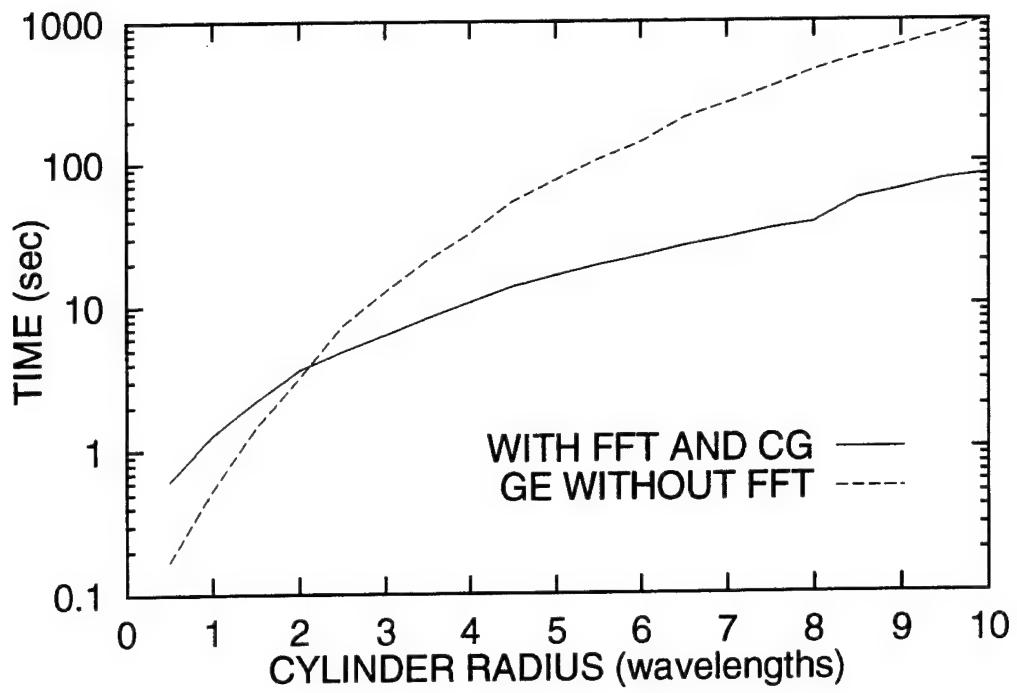
Figure 12. Comparison of CPU Times for FFT and CG Method and Gaussian Elimination for Right Circular Cylinders; $\theta_t = 90°$.

6 MODIFICATION OF THE DMFIE FOR BODIES WITH SHARP TIPS

6.1 Formulation

It is well documented that the original MFIE and thus the DMFIE degenerate toward an underdetermined system of linear equations for infinitesimal thin bodies.[5,12,13,14,15,16] Reference 15 describes the numerical implementation of the MFIE for an extremely thin body, a metallic disk with a thickness of $10^{-5}\lambda$. Reference 5 compares the measured and MFIE-computed values of the E- and H-plane RCS's for a perfectly conducting circular disk with a radius of 2λ and a thickness of $\lambda/20$. Reference 14 states that the MFIE is not applicable for thin or open bodies but does not define what the criterion is for a thin body. The claim that the MFIE is "useless for infinitely thin scatterers but finds its greatest use in large smooth conductors" is found in Reference 12.

Consider the RCS of the conesphere shown in Figure 13 computed using the DMFIE. Figures 14 and 15 show E-plane and H-plane monostatic RCS versus target aspect angle for the DMFIE and measurements.[17] Note the large discrepancy between the E-plane computed results and the measurements in the angular region from approximately $0 - 60°$, the illumination of the sphere portion of the conesphere. After measurement error was ruled out by the comparison of measurements from two different measurement facilities,[18] the number of divisions per wavelength in the t and ϕ coordinates were increased to ensure convergence of the numerical scheme. Figure 16 compares the E-plane DMFIE numerical results for 20, 30, and 80 divisions per wavelength. One sees the extremely slow convergence of numerical solution to the measured results.

The E- and H-plane DMFIE RCS results for the conesphere with 20 segments per wavelength were compared to the CFIE, MFIE, and EFIE results from CICERO,[19] a CFIE formulation for axially inhomogeneous bodies of revolution. The CICERO code uses triangular instead of pulse functions, which may account for the slight difference in the MFIE and DMFIE E-plane solutions. However, Figure 18 clearly demonstrates that the discrepancy is a result of the MFIE formulation, not the implementation of the DMFIE. The close agreement between the CFIE results and measurements suggests that the CFIE is the "correct" answer. The CFIE solution with 400 divisions per wavelength will be used as the "exact" reference solution.

---

[12] Poggio, A.J., and Miller, E.K. (1987) Solution of Three-Dimensional Scattering Problems, in *Computer Techniques for Electromagnetics*, Mittra, R., ed., Springer-Verlag, p. 168.

[13] Sadasiv, M.R., Wilton, D.R., and Glisson, A.W. (1982) Electromagnetic Scattering by Surfaces of Arbitrary Shape, *IEEE Trans. Antennas Propagat.*, **AP-30**:409-418.

[14] Glisson, A.W.,and Wilton, D.R., (1980) Simple and Efficient Methods for Problems of Electromagnetic Radiation and Scattering from Surfaces, *IEEE Trans. Antennas Propagat.*, **AP-28**:593-603.

[15] Sancer, M.I., McClary, R.L., and Glover, K.J. (1990) Electromagnetic Computation using Parametric Geometry, *Electromagnetics*, **10**:85-103.

[16] Phone discussion with D. Wilton, University of Houston, Houston, TX.

[17] Larose, C. and Shantnu, M., of David Florida Laboratory, Canadian Space Agency, Ottawa, Ontario, performed the RCS measurements. One measurement was performed from $0 - 360°$ in aspect angle, but the symmetry of the conesphere allows the measurement data from $180 - 360°$ to be plotted from $0 - 180°$ aspect angle

[18] Wing, R. and Cote, M., of Rome Laboratory, Hanscom AFB, MA, performed a second set of measurements on the conesphere.

[19] Putnam, J.M. and Medgyesi-Mitschang, L.N. (1987) *Combined Field Integral Equation Formulation for Axially Inhomogeneous Bodies of Revolution*, McDonnell Douglas Corporation Report No. QA003, Volume I: Final Technical Report, St. Louis, MO., Sandia National Laboratory Contract No. 33-4257.

Figure 13. Geometry for Conesphere.

The amplitude and phase of the scattered field for the first three modes were calculated, individually and collectively, over our aspect angular range of $0 - 80°$ for the MFIE and CFIE using CICERO. Figures 20 to 29 show the comparison of these results for the different formulations.[20] It was determined from these results that the zero order current mode is not properly modeled in the present DMFIE and MFIE formulations. This assumption was further verified by calculating the phase and amplitude of the currents for each mode at an incident angle of 20° with the CFIE solution. Figure 30 shows that at this incident angle only the zero and first order modes are significant contributors to the total current. The amplitude and phase of these two modes are shown in Figures 31-34 for the DMFIE, MFIE, and CFIE.

Reference 15 states that the cells on the opposite faces of a thin structure can become so close that the calculation of the matrix element containing the cells can break down numerically and give erroneous answers to the MFIE. The presented numerical solution in Reference 15 is a finer integration of these cells. This information prompted the modification of the DMFIE program to allow finer integration of the self ring, that is when $t = t'$, for the zero order mode, t-directed current. The self ring patch is divided into a predetermined number of tiny segments that are individually integrated and then coherently summed to obtain the self ring value. Figure 35 shows that finer integration of the self ring has little effect on the DMFIE solution. The only visible difference in the five results is located at the deep null at approximately 15°.

---

[20] This approach was suggested by J.M. Putnam of McDonnell Douglas Research Laboratories, St. Louis, MO.
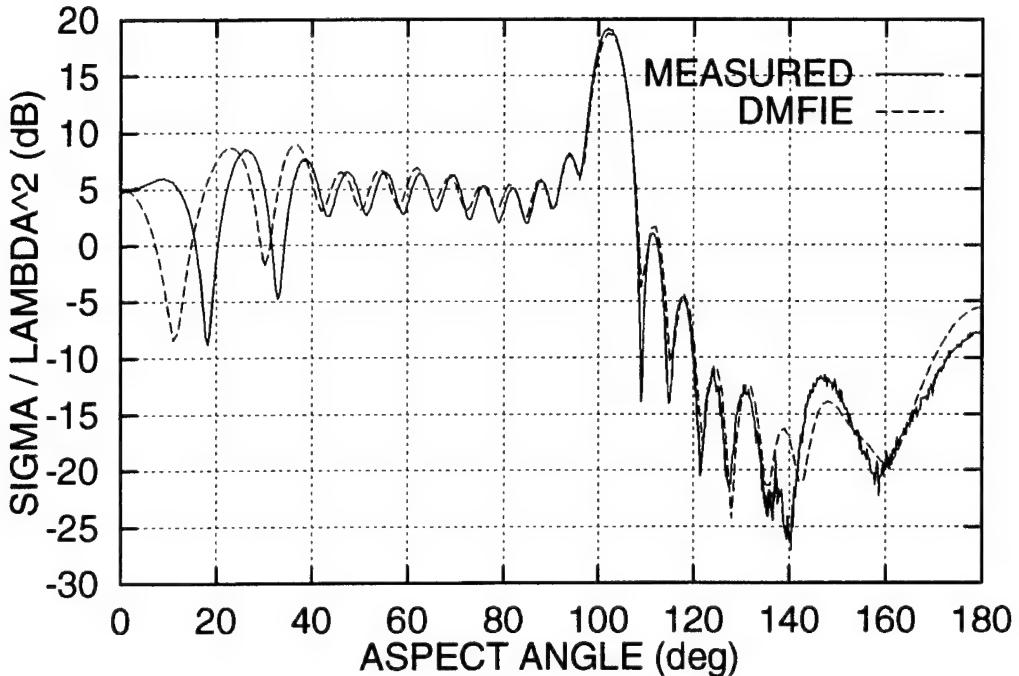
Figure 14. Comparison of the E-Plane Monostatic RCS of Conesphere for the DMFIE and Measurements; $ka = 6.36$.

Singularities of the tip of a circular cone have been documented by various authors.[21,22,23] Reference 21 concentrates on the circular cone shown in Figure A1 and is directly applicable to the conesphere problem. The static electromagnetic expression, explained in additional detail in Appendix A, was implemented for the self ring when the source point was at the tip patch and the field point up to twenty patches away on the cone portion of the conesphere. Figures 36-38 show the current and RCS, respectively, at an aspect angle of 20° for the implementation of this method and the CFIE. Figure 38 shows no considerable improvement in the RCS.

The next attempt at solving the problem was to use the exact tip current for a semi-infinite cone.[24] From Reference 24, it was determined that the $t-$directed zero order mode current at the tip of the cone has a Spherical Bessel function $j_\nu(t)$ variation where t is the radial distance from the tip of the cone in wavelengths. The mathematical and numerical details are presented in Appendix B. The $t-$directed current for mode zero is now approximated by

$$J^{tt} = D j_\nu(t) \tag{59}$$

[21] Van Bladel, J. (1983) Field singularities at the tip of a cone, *Proc. IEEE*, **71**:901-902.

[22] DeSmedt, R. and Van Bladel, J. (1986) Fields at the tip of a metallic cone of arbitrary cross section, *IEEE Trans. Antennas Propagat.*, **34**:865-870.

[23] Jackson, J.D. (1975) *Classical Electrodynamics*, Wiley, New York, 2nd ed., pp. 94-102.

[24] Trott, K.D. (1986) *A High Frequency Analysis of Electromagnetic Plane Wave Scattering by a Fully Illuminated Perfectly Conducting Semi-Infinite Cone*, Dissertation at Ohio State University, Columbus ,Ohio.
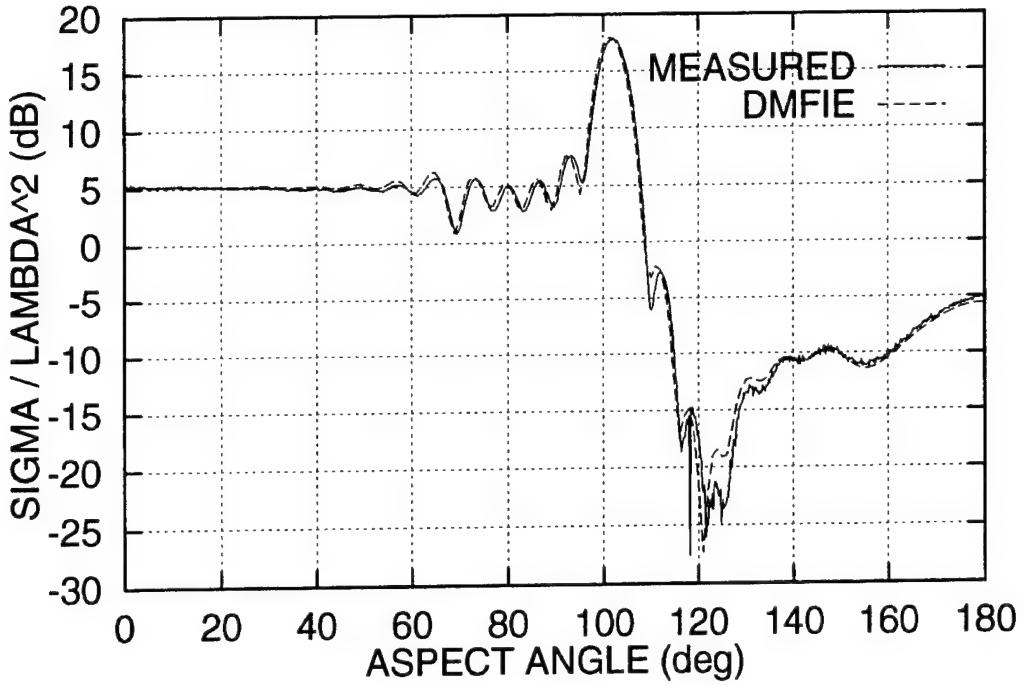
Figure 15. Comparison of the H-Plane Monostatic RCS of Conesphere for the DMFIE and Measurements; $ka = 6.36$.

where D is some constant. The program was then modified to use a Spherical Bessel function variation for the t-directed current for the segment at the tip of the conesphere with a segment length that corresponds to the location of the first maximum of the Spherical Bessel function. Figures 39 and 40 show the comparison of the current from the modified DMFIE, MFIE, and CFIE. One sees the improvement in the current. Figure 41 compares the original DMFIE, the modified DMFIE, the CFIE, and measurements. One now sees that the modified DMFIE, CFIE and measurements compare fairly well in the problem region.

We find that the failure to accurately model the current near the tip affects not only the current near the tip, but also many wavelengths away from the tip. Therefore, the expression in Eq. (31) for the scattered magnetic field, which shows that the current within a quarter wavelength of the tip has little effect on the RCS, does not account for enough of the physics of the problem. The conclusion is that for the conesphere where the t-directed current near the tip for mode zero has a strong effect for many wavelengths away from the tip, and thus a strong effect on the RCS, accurate modeling of the current must be performed.

24
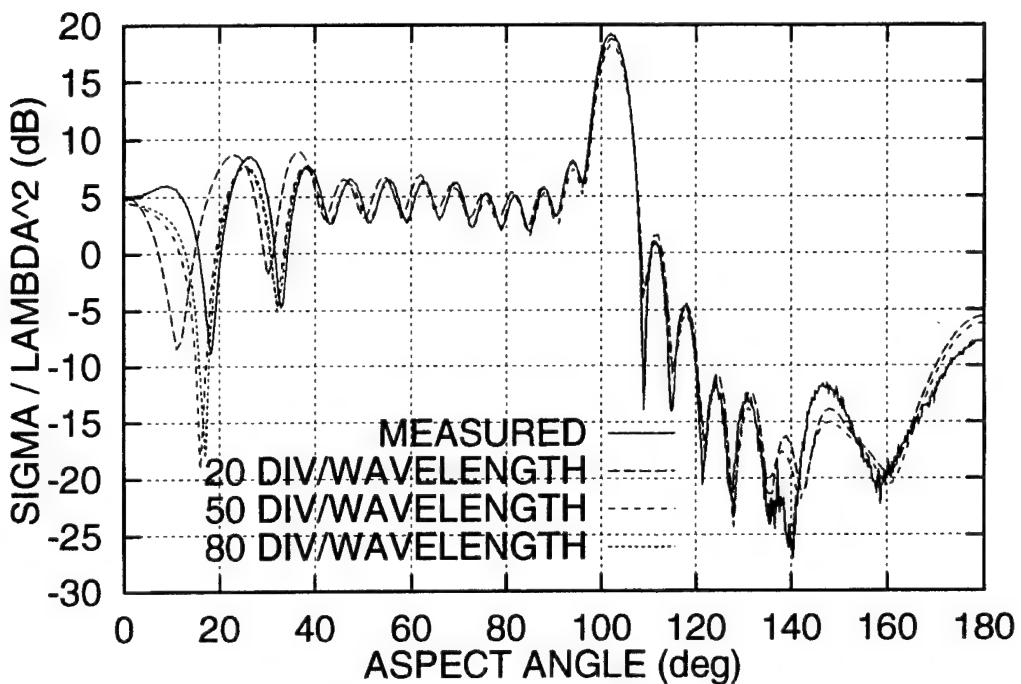
Figure 16. Comparison of the E-Plane DMFIE Monostatic RCS of Conesphere for 20, 50, and 80 Divisions per Wavelength with Measurements; $ka = 6.36$.
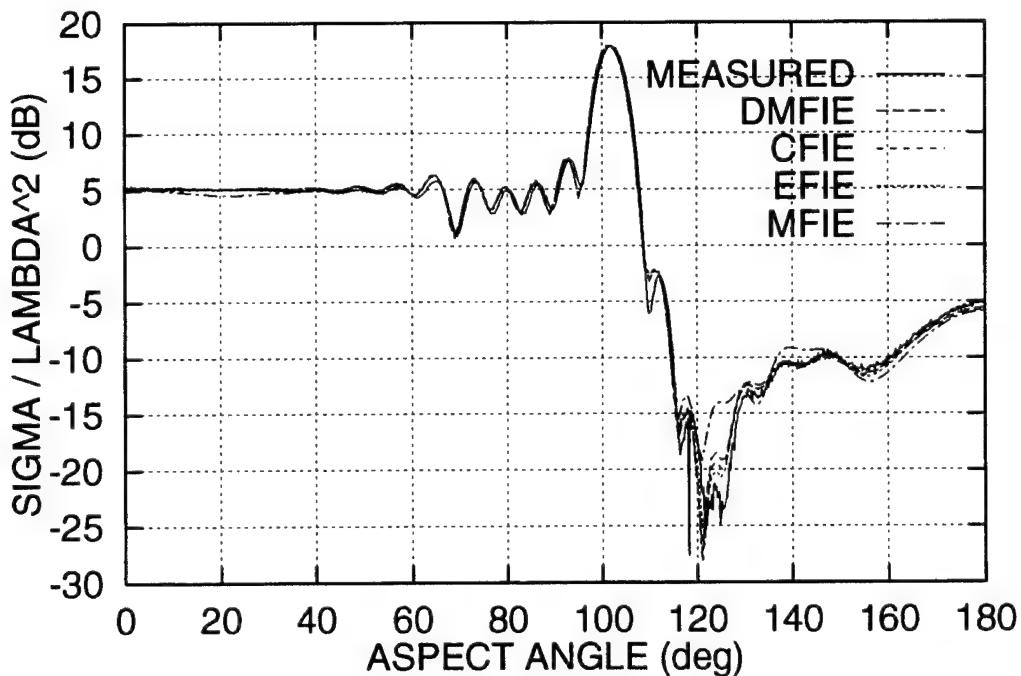

Figure 17. H-Plane Monostatic RCS of Conesphere for the DMFIE, MFIE, EFIE, CFIE, and Measurements; $ka = 6.36$.
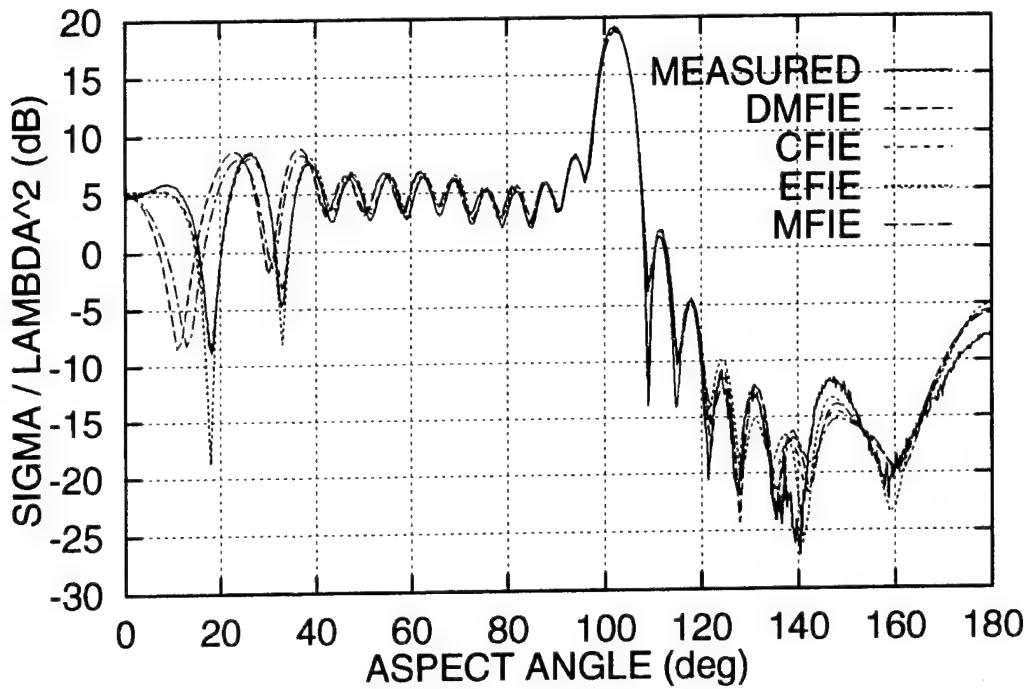
Figure 18. E-Plane Monostatic RCS of Conesphere for the DMFIE, MFIE, EFIE, CFIE, and Measurements; $ka = 6.36$.
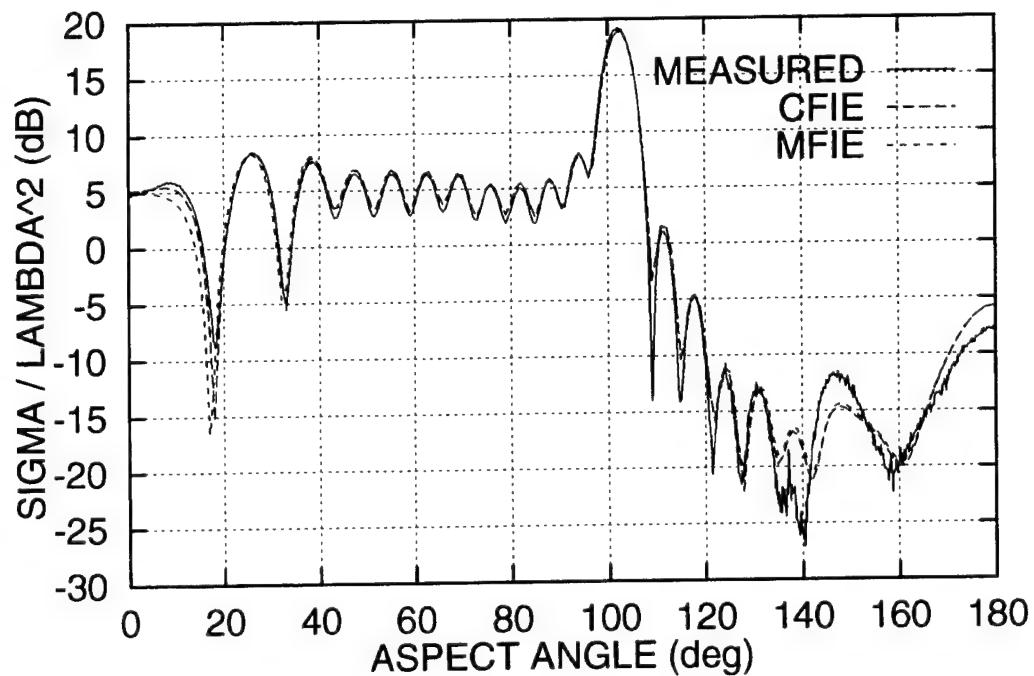

Figure 19. E-Plane Monostatic RCS of Conesphere for the MFIE, CFIE, and Measurements with 400 t-Divisions per Wavelength; $ka = 6.36$.
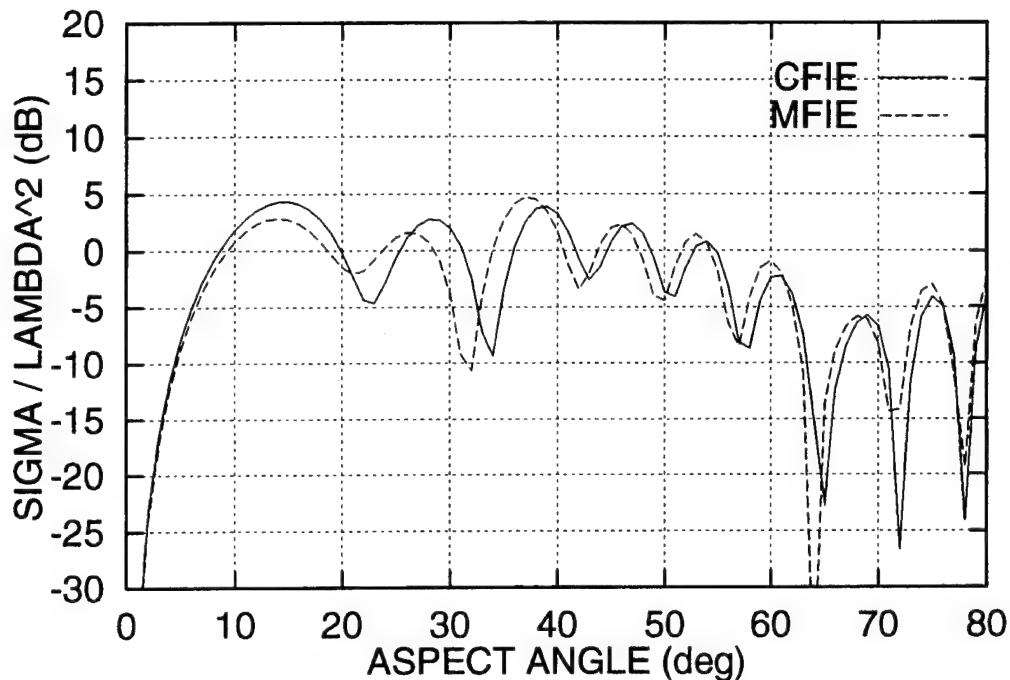
Figure 20. Amplitude of the E-Plane Scattered Field of Conesphere for the MFIE and CFIE; $ka = 6.36$, mode zero.
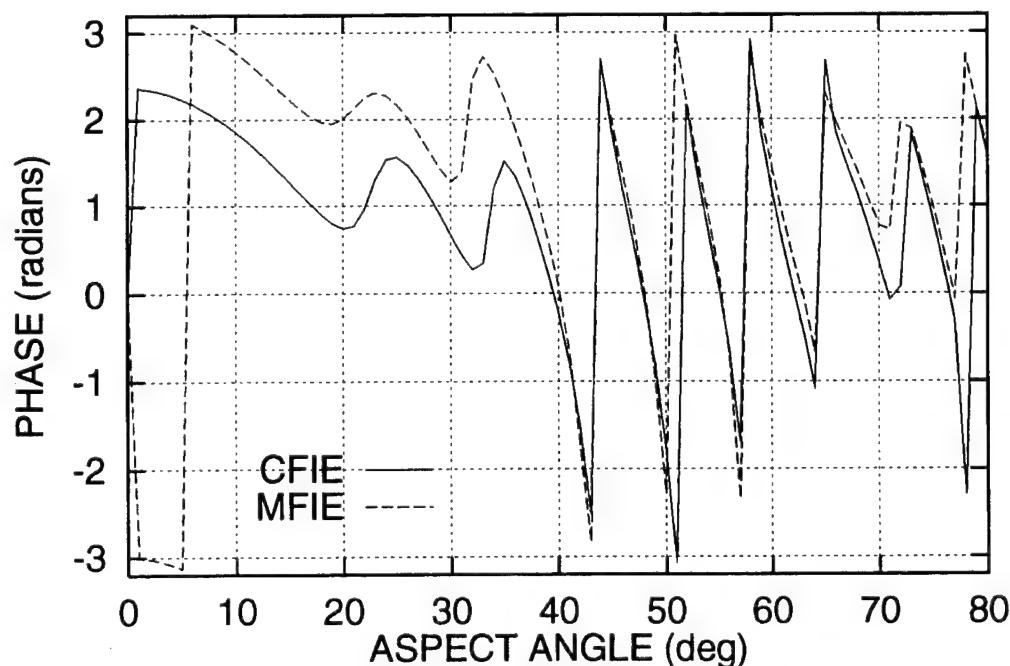

Figure 21. Phase of the E-Plane Scattered Field of Conesphere for the MFIE and CFIE; $ka = 6.36$, mode zero.
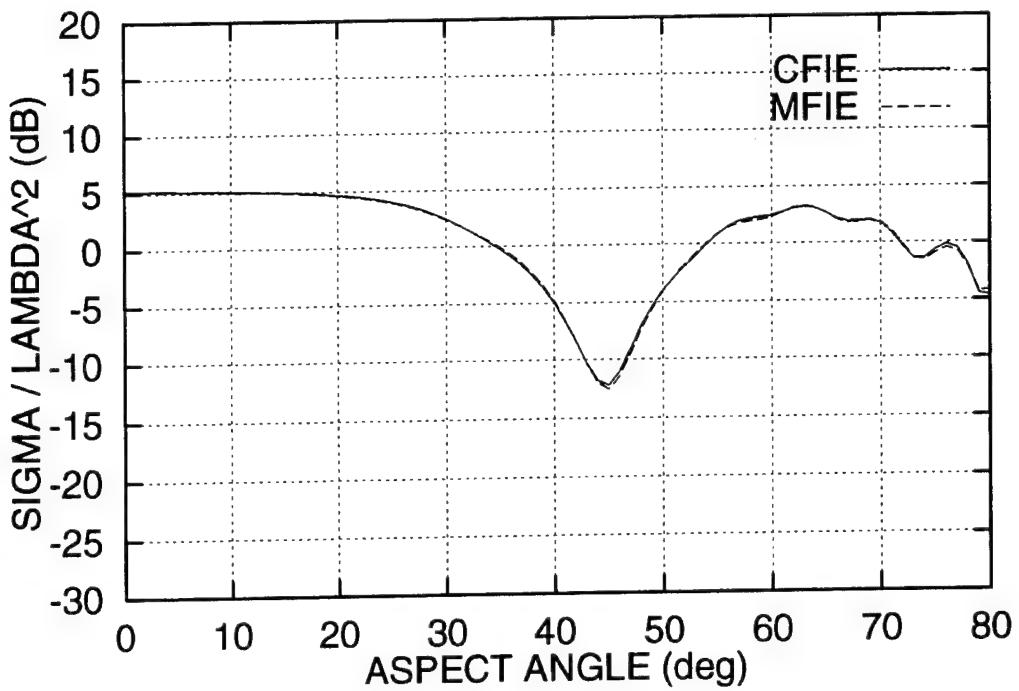
Figure 22. Amplitude of the E-Plane Scattered Field of Conesphere for the MFIE and CFIE; $ka = 6.36$, mode one.
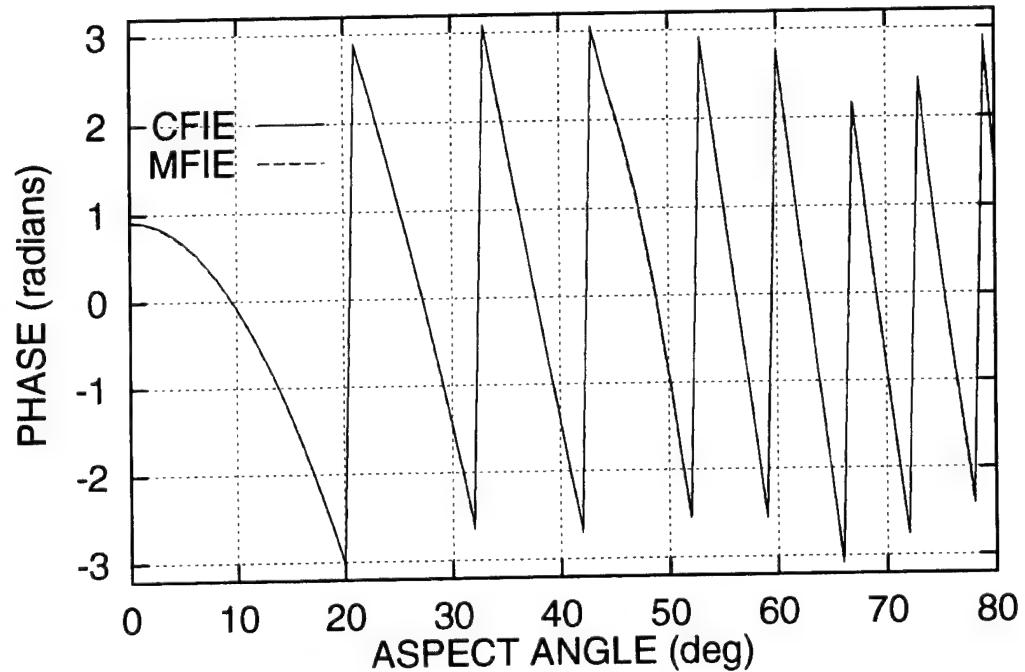
Figure 23. Phase of the E-Plane Scattered Field of Conesphere for the MFIE and CFIE; $ka = 6.36$, mode one.
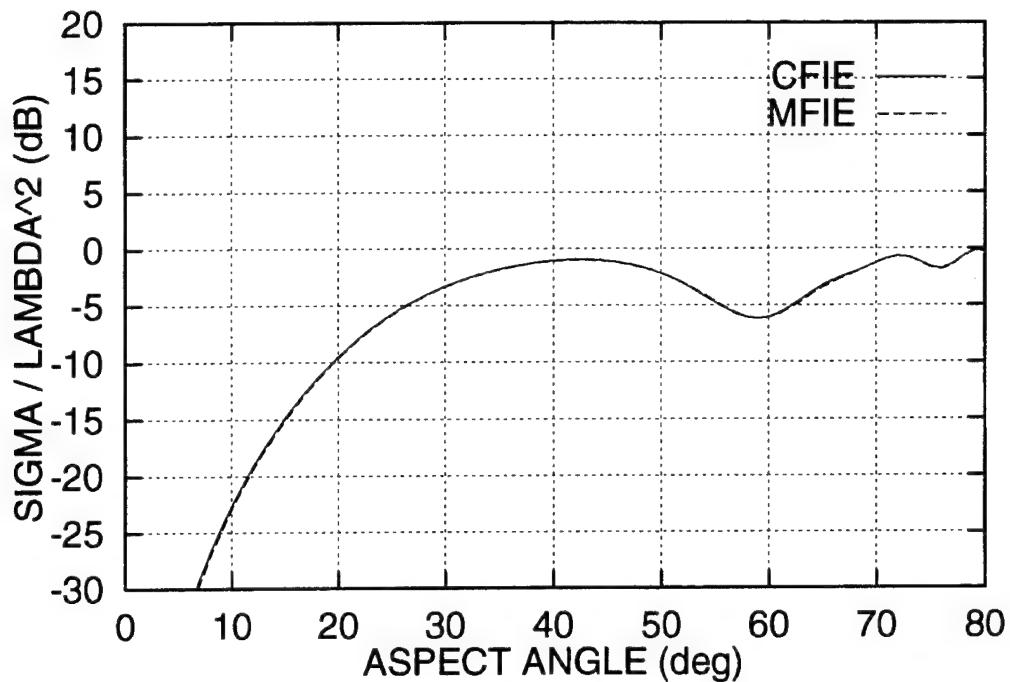
Figure 24. Amplitude of the E-Plane Scattered Field of Conesphere for the MFIE and CFIE; $ka = 6.36$, mode two.
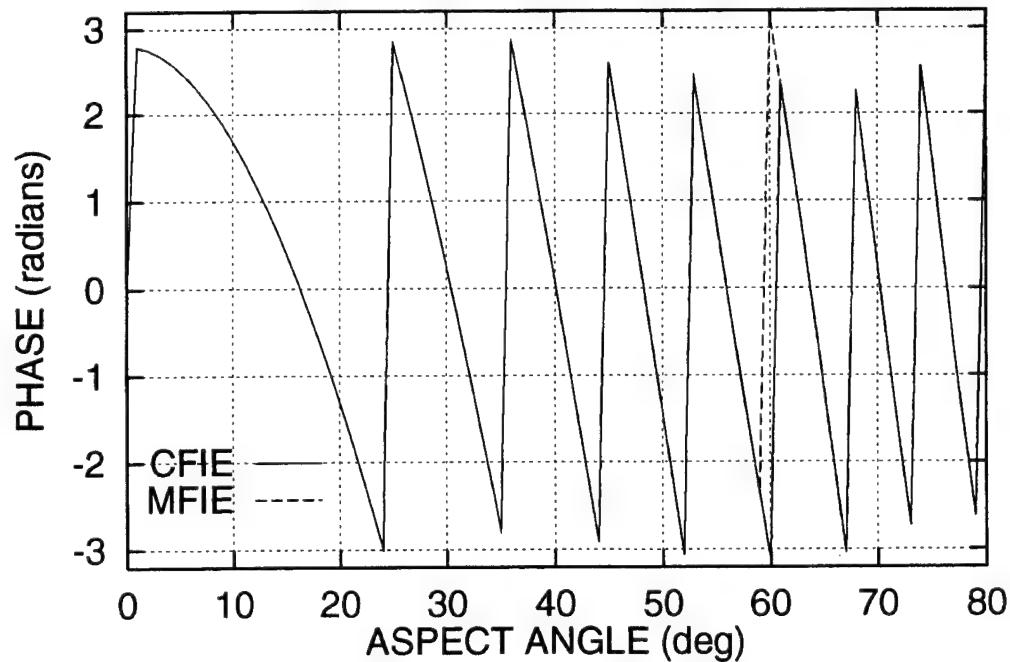

Figure 25. Phase of the E-Plane Scattered Field of Conesphere for the MFIE and CFIE; $ka = 6.36$, mode two.
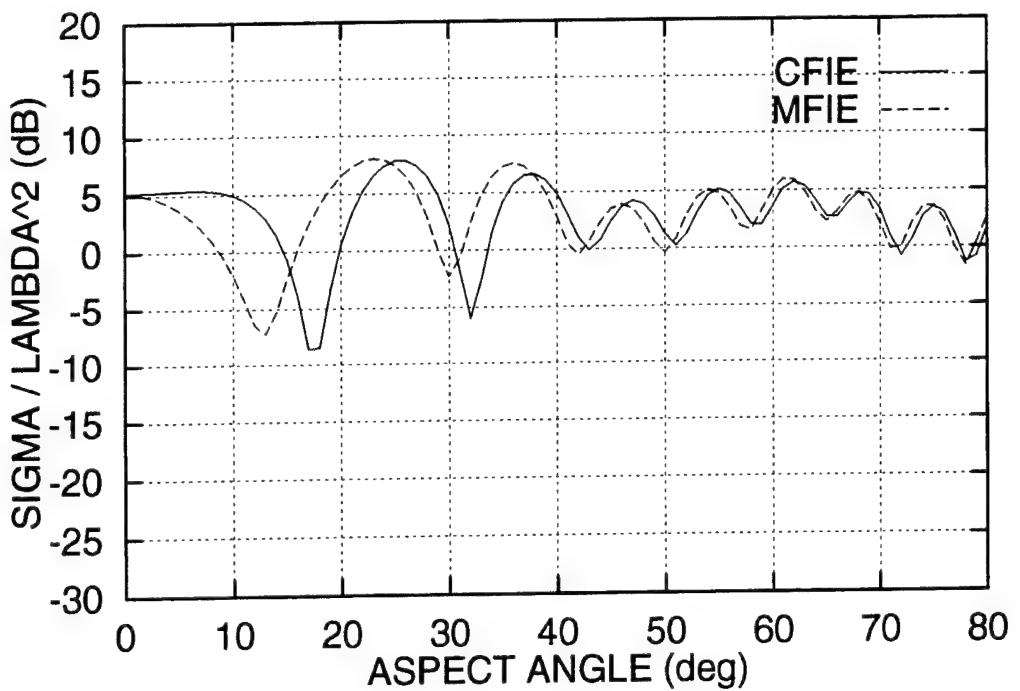
Figure 26. Amplitude of the E-Plane Scattered Field of Conesphere for the MFIE and CFIE; $ka = 6.36$, modes zero and one.
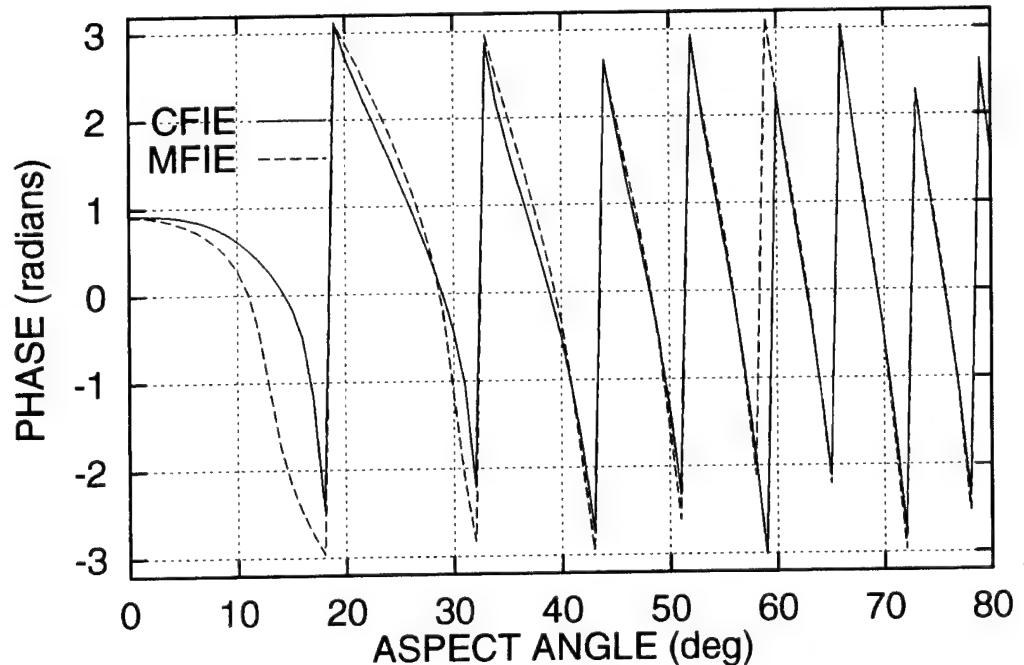

Figure 27. Phase of the E-Plane Scattered Field of Conesphere for the MFIE and CFIE; $ka = 6.36$, modes zero and one.
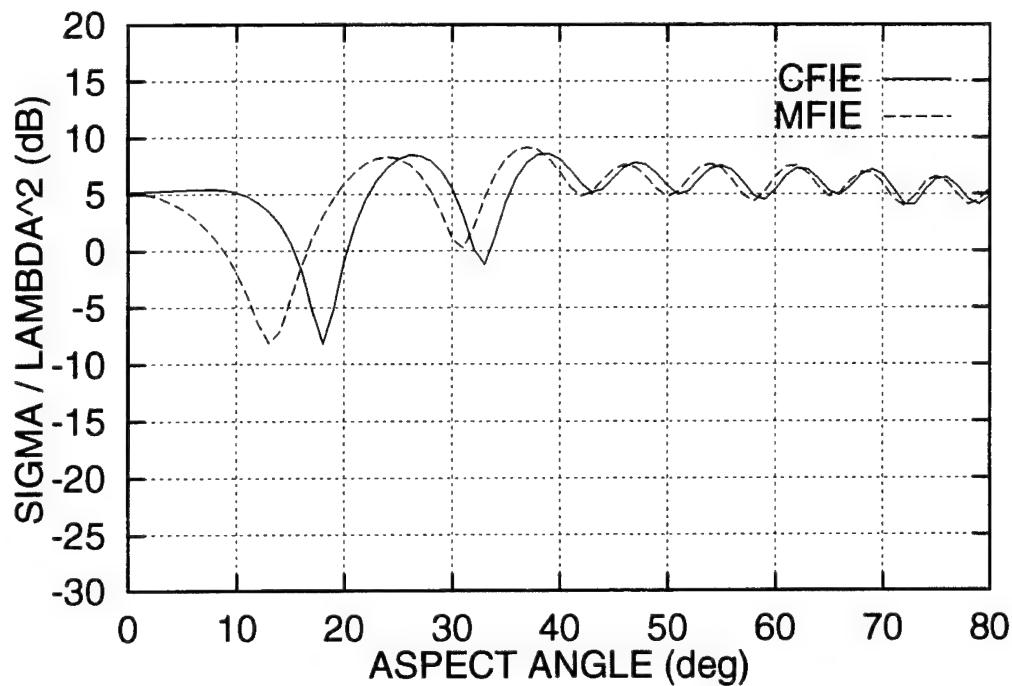
Figure 28. Amplitude of the E-Plane Scattered Field of Conesphere for the MFIE and CFIE; $ka = 6.36$, modes zero, one, and two.
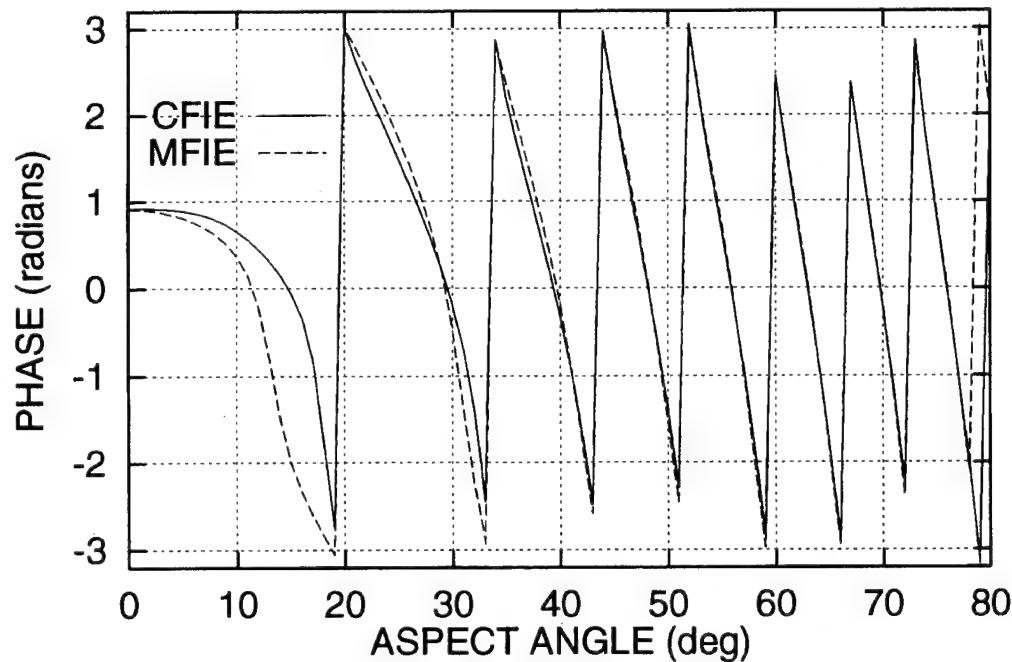

Figure 29. Phase of the E-Plane Scattered Field of Conesphere for the MFIE and CFIE; $ka = 6.36$, modes zero, one, and two.
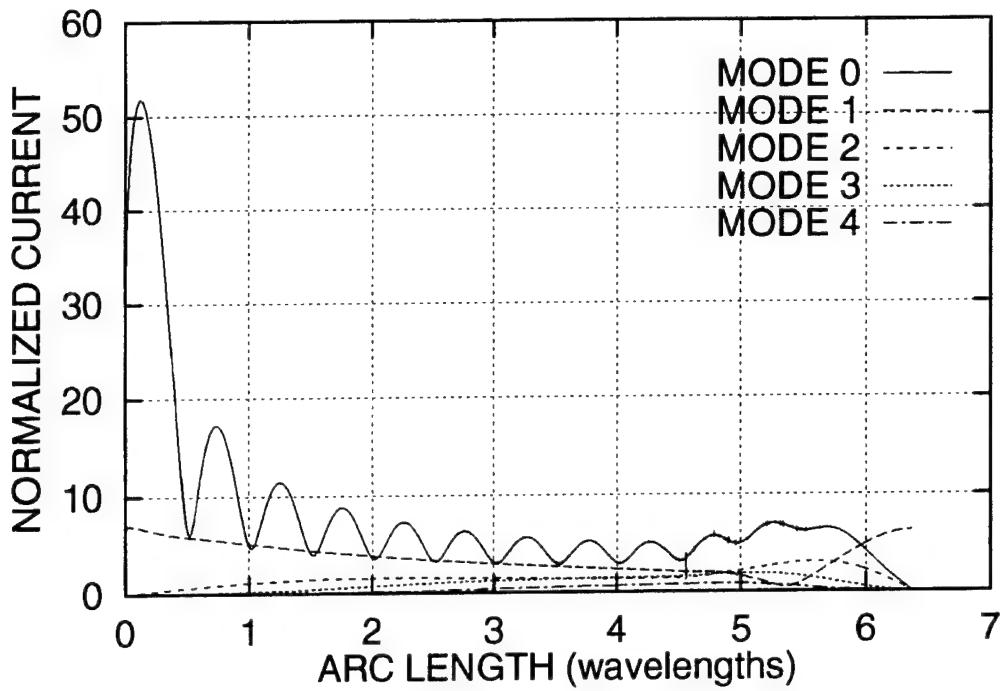
Figure 30. Amplitude of the E-Plane CFIE Solution Current for Conesphere; $ka = 6.36$, $\theta_t = 20°$, all modes.
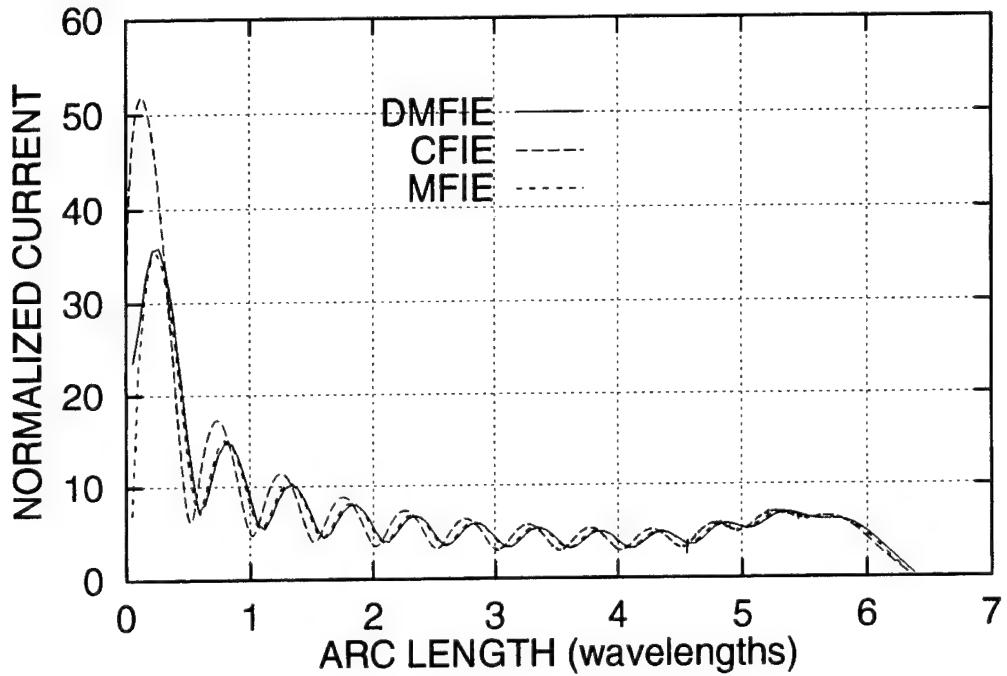
Figure 31. Amplitude of the E-Plane DMFIE, MFIE, and CFIE Solution Current for Conesphere; $ka = 6.36$, $\theta_t = 20°$, mode zero.
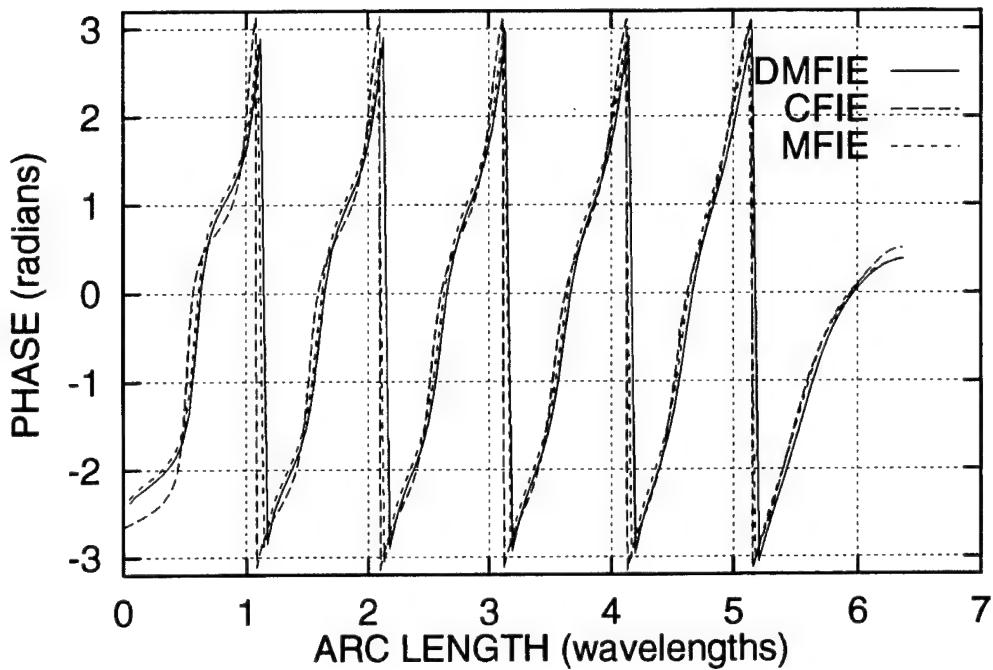
Figure 32. Phase of the E-Plane DMFIE, MFIE, and CFIE Solution Currents for Conesphere; $ka = 6.36$, $\theta_t = 20°$, mode zero.
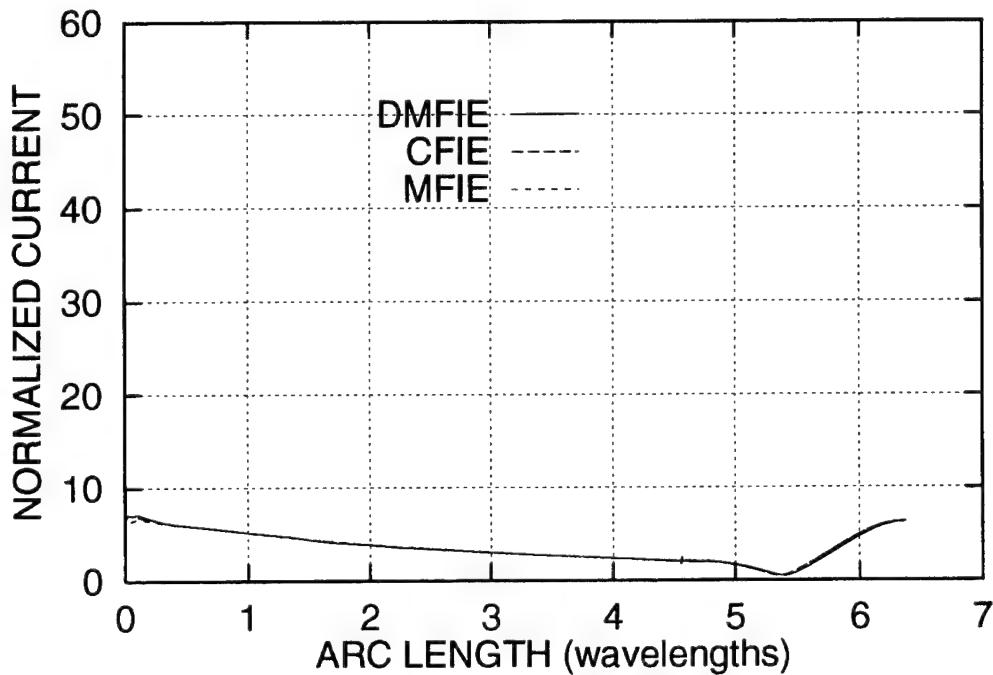
Figure 33. Amplitude of the E-Plane DMFIE, MFIE, and CFIE Solution Currents for Conesphere; $ka = 6.36$, $\theta_t = 20°$, mode one.
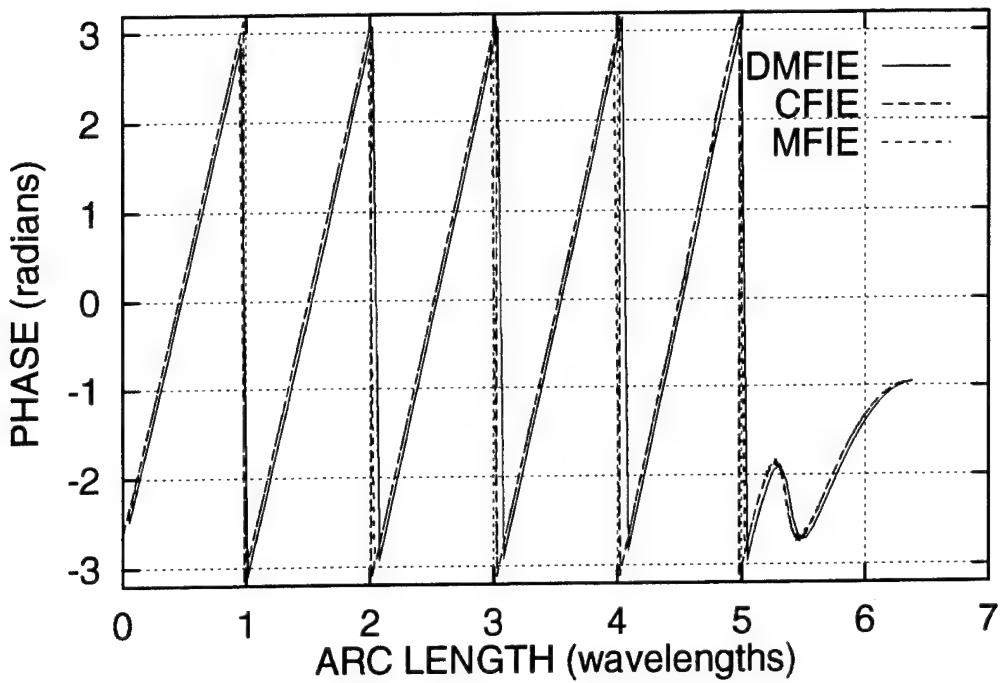
Figure 34. Phase of the E-Plane DMFIE, MFIE, and CFIE Solution Currents for Conesphere; $ka = 6.36$, $\theta_t = 20°$, mode one.
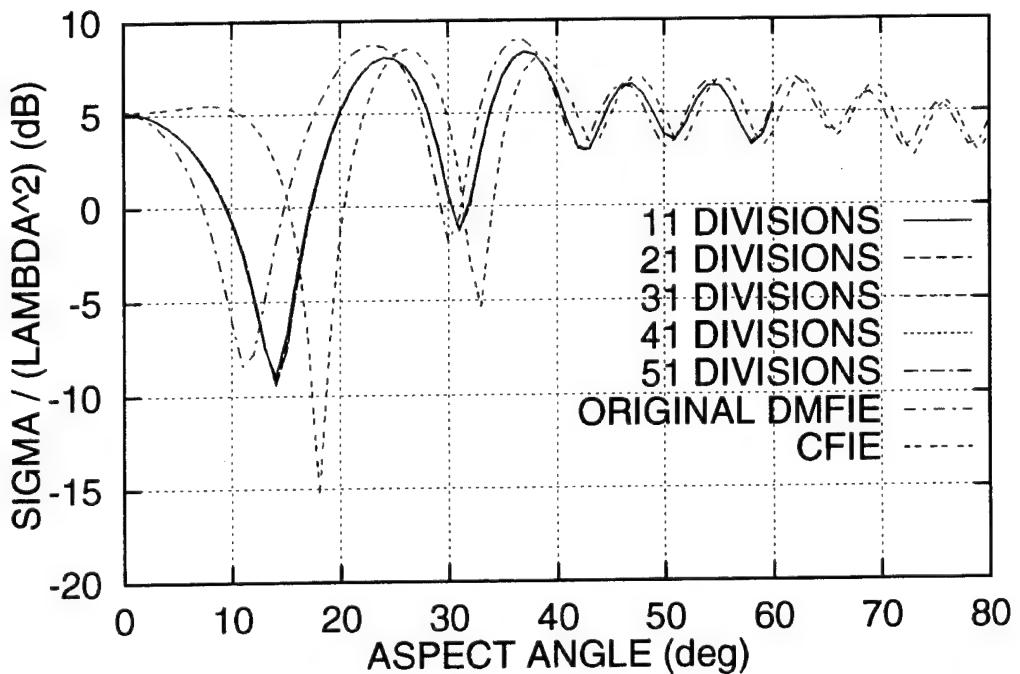
Figure 35. E-Plane Monostatic RCS with DMFIE Using Finer Integration on Self-Ring for t-Directed Current, Original DMFIE, and CFIE; $ka = 6.36$.
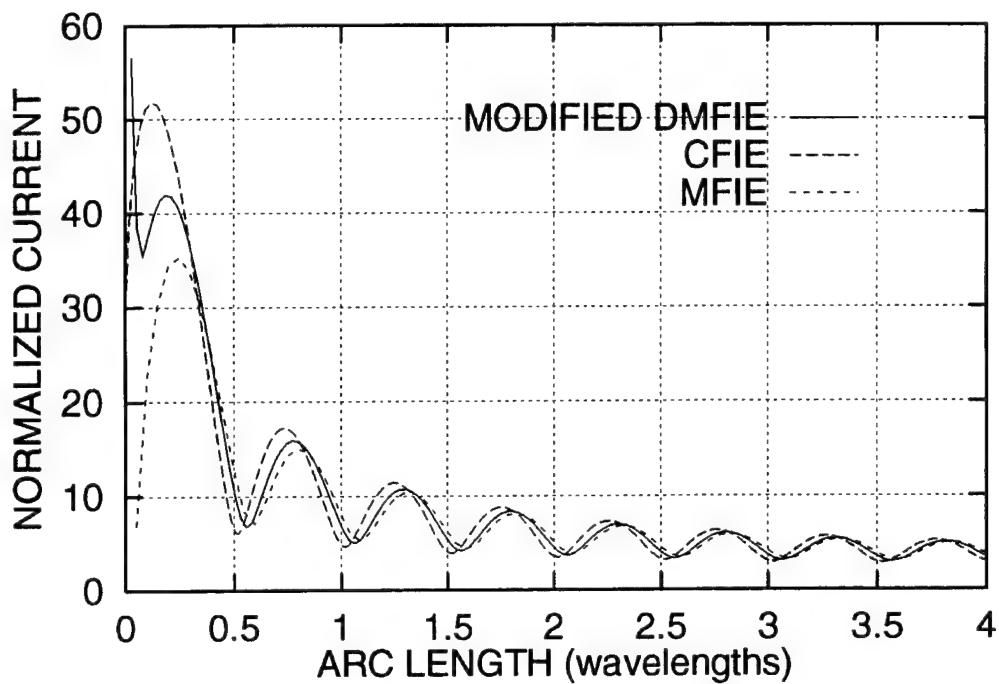
Figure 36. Amplitude of the E-Plane Modified DMFIE using t^{ν} Current Dependence, Currents of MFIE and CFIE Solutions for Conesphere; $ka = 6.36$, $\theta_t = 20°$, mode zero.
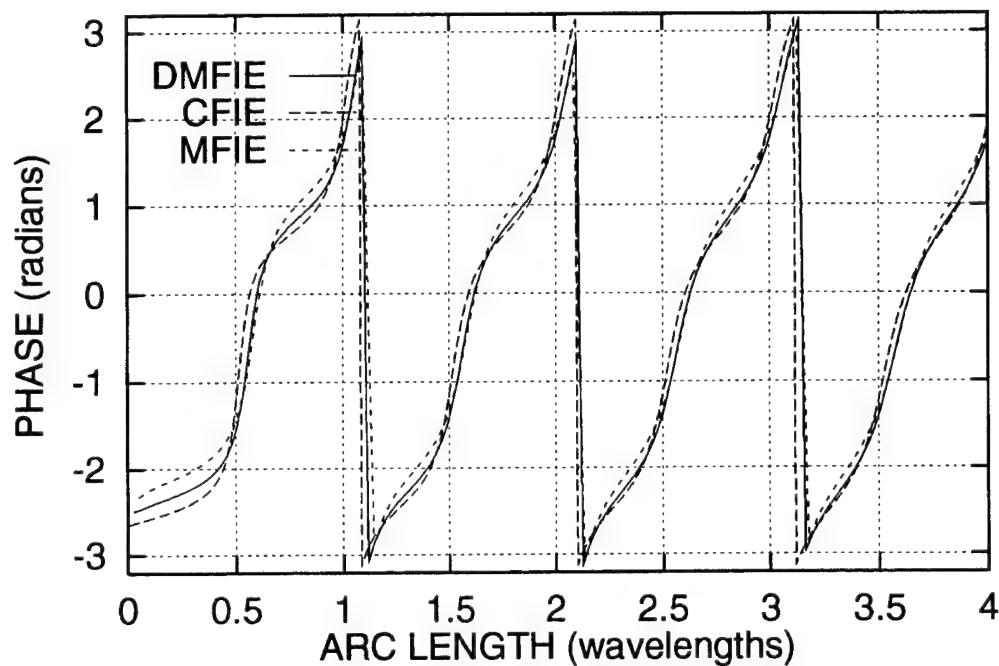
Figure 37. Phase of the E-Plane Modified DMFIE using t^{ν} Current Dependence, Currents of MFIE and CFIE Solutions for Conesphere; $ka = 6.36$, $\theta_t = 20°$, mode zero.
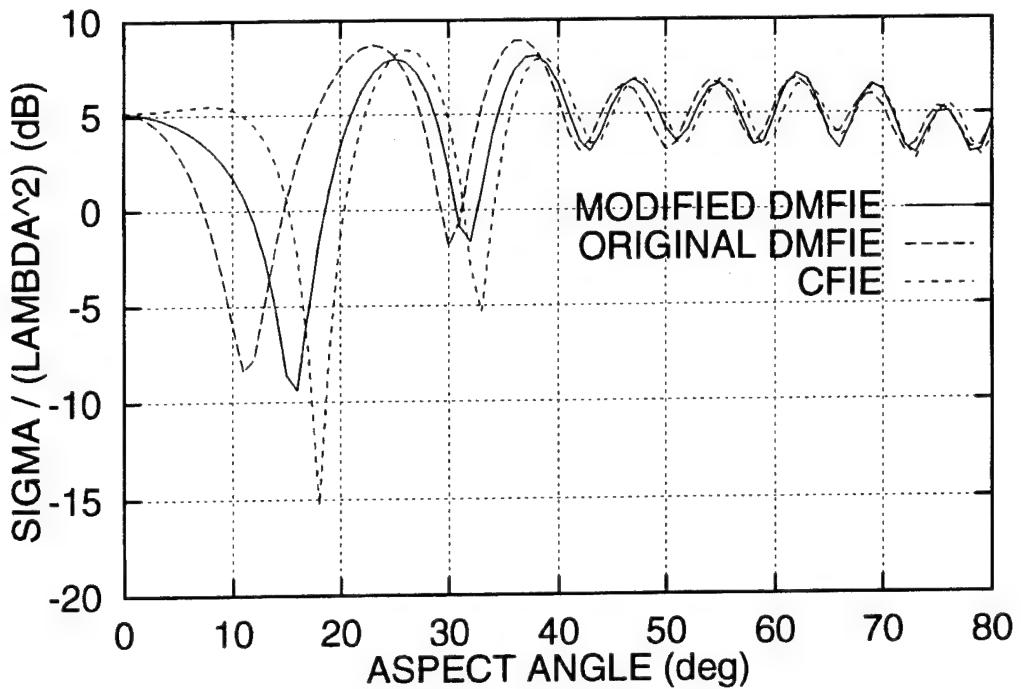
Figure 38. E-Plane Monostatic RCS for Conesphere for the Modified DMFIE using t^ν Current Dependence, Original DMFIE, and CFIE; $ka = 6.36$.
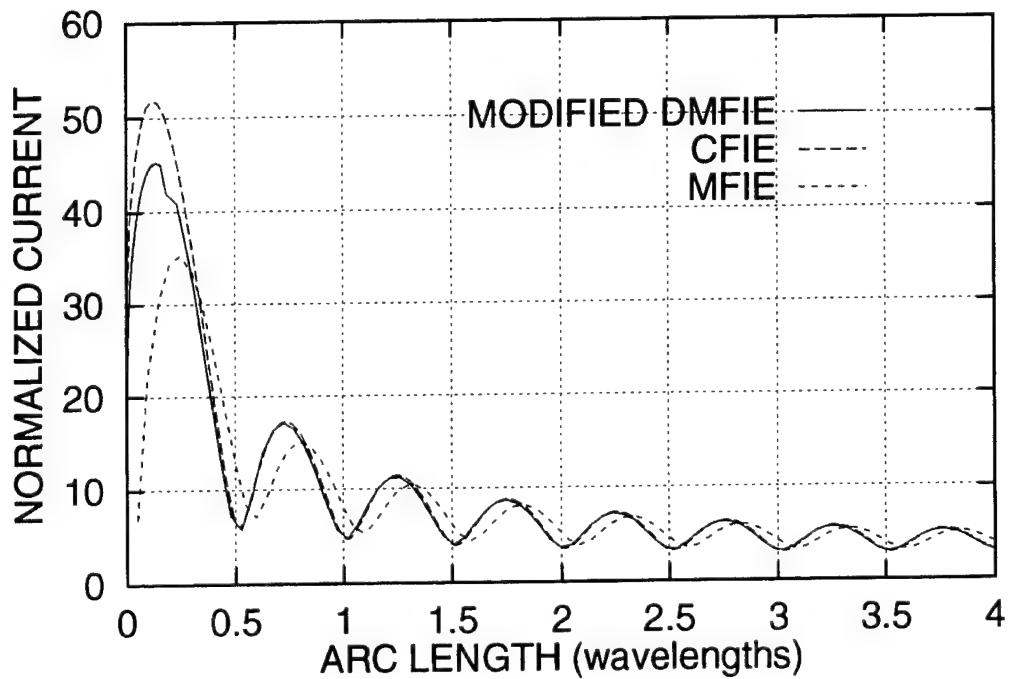
Figure 39. Amplitude of the E-Plane Modified DMFIE using j_ν Current Dependence, Currents for MFIE and CFIE Solutions for Conesphere; $ka = 6.36$, $\theta_t = 20°$, mode zero.
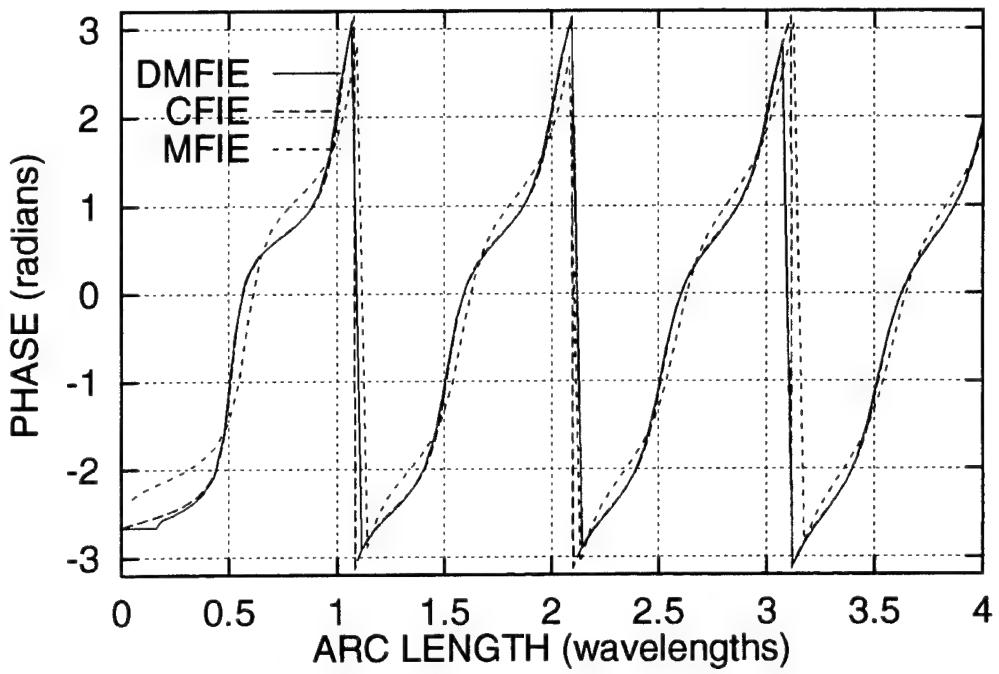
Figure 40. Phase of the E-Plane Modified DMFIE using j_ν Current Dependence, Currents for MFIE and CFIE Solutions for Conesphere; $ka = 6.36$, $\theta_t = 20°$, mode zero.
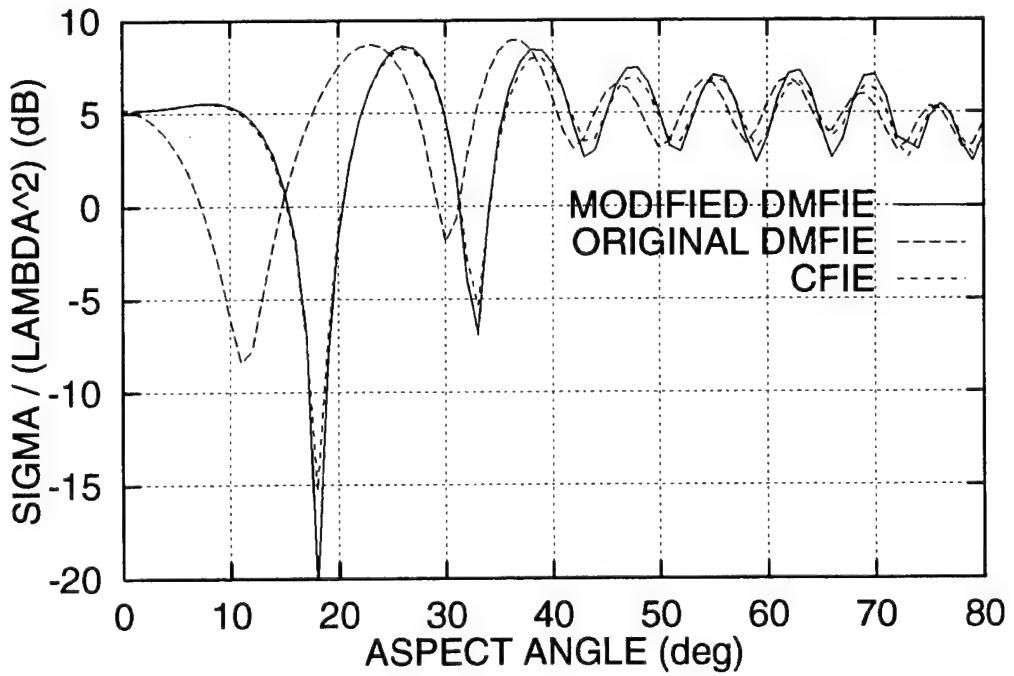
Figure 41. E-Plane Monostatic RCS for Conesphere for the Modified DMFIE using j_ν Current Dependence, Original DMFIE, and CFIE; $ka = 6.36$.
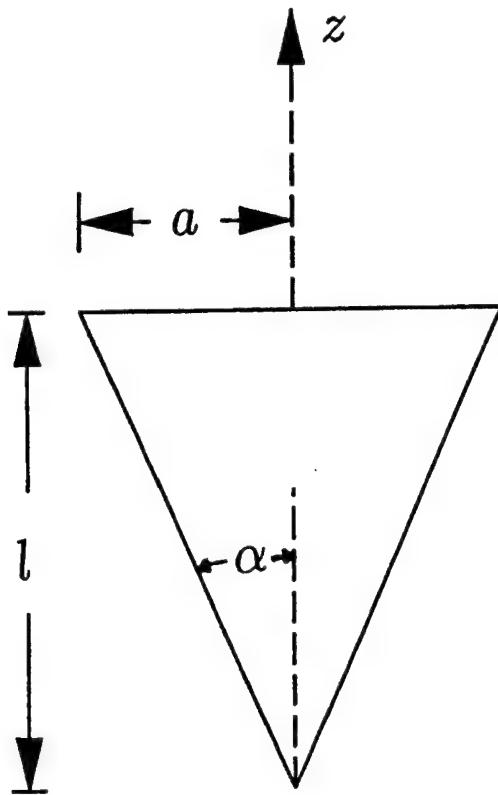
Figure 42. Geometry for Right Circular Cone

6.2 Numerical Implementation

The original DMFIE code was modified to include the Spherical Bessel function dependence of the tip current. The code was automated so that the operator can at will, use this Spherical Bessel function calculation of the better tip current for tipped scatterers. A subroutine was included to find the maximum of the Spherical Bessel function and set the length of the first segment on the tip of the scatterer to this electrical length. This program was then used to compute the RCS of conespheres and right circular cones of various values of ka.

Figure 42 shows the geometry and dimensions for the flat-backed right circular cone. In Figures 43-66, the RCS versus aspect angle for different electrical sized conespheres as well as flat-backed cones is presented. The CFIE results were computed with CICERO using 100 divisions per wavelength and the measurements performed as stated in Reference 17. The original and modified DMFIE results used 20 divisions per wavelength.

The results demonstrate that the flat-back cones seem to be less sensitive to the current at the tip of the cone than the conespheres for small cone half-angles. There is no difference between the two DMFIE results when the half-cone angle is greater than 15°, as
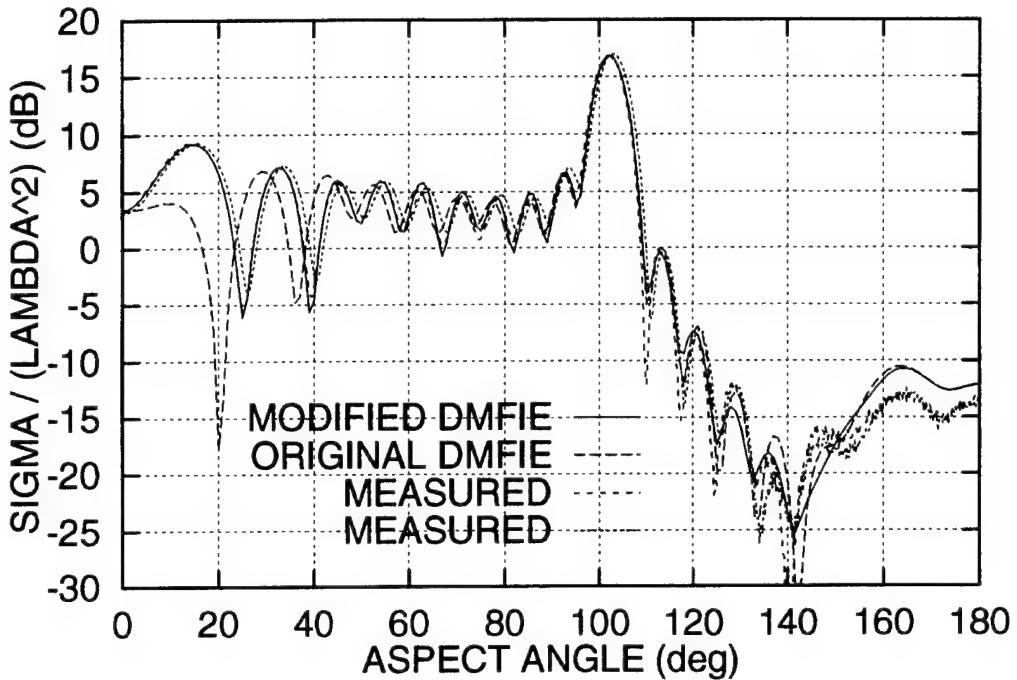
Figure 43. E-Plane Monostatic RCS for Conesphere for the Modified DMFIE using j_ν Current Dependence, Original DMFIE, and Measurements; $ka = 5.38$.

is expected. The conespheres, as demonstrated previously, are extremely sensitive to the modeling of the mode zero current.
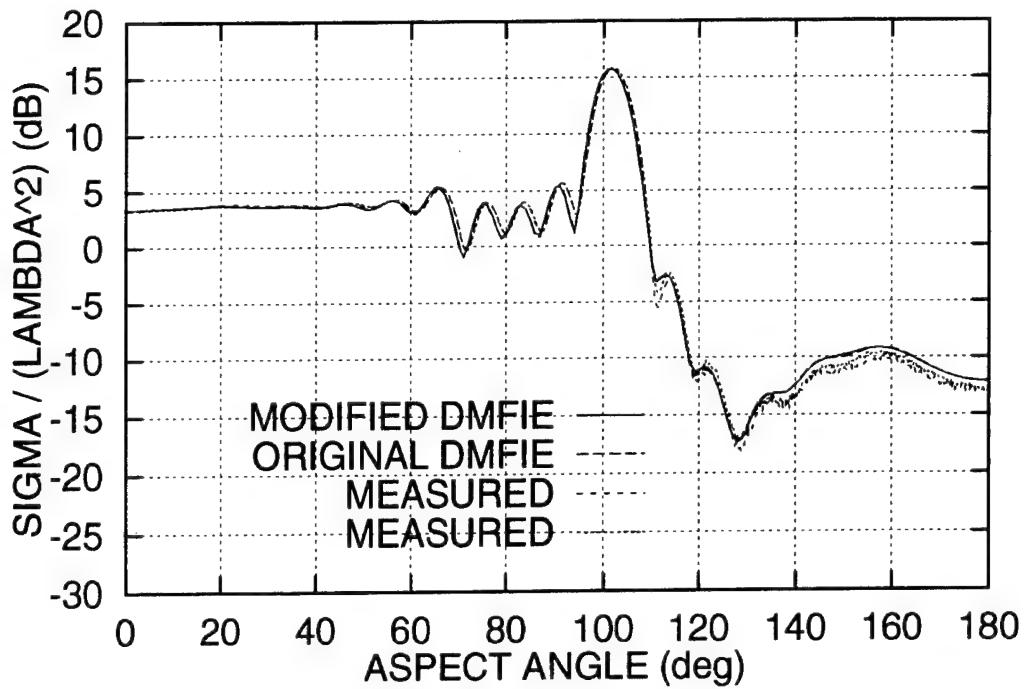
Figure 44. H-Plane Monostatic RCS for Conesphere for the Modified DMFIE using j_ν Current Dependence, Original DMFIE, and Measurements; $ka = 5.38$.
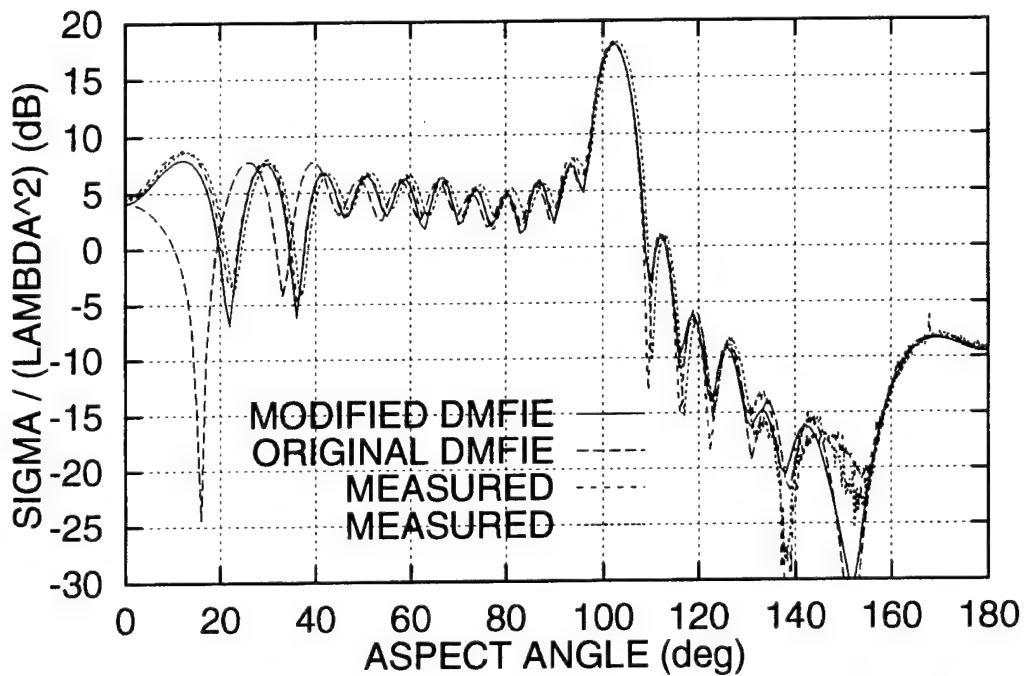
Figure 45. E-Plane Monostatic RCS for Conesphere for the Modified DMFIE using j_ν Current Dependence, Original DMFIE, and Measurements; $ka = 5.87$.
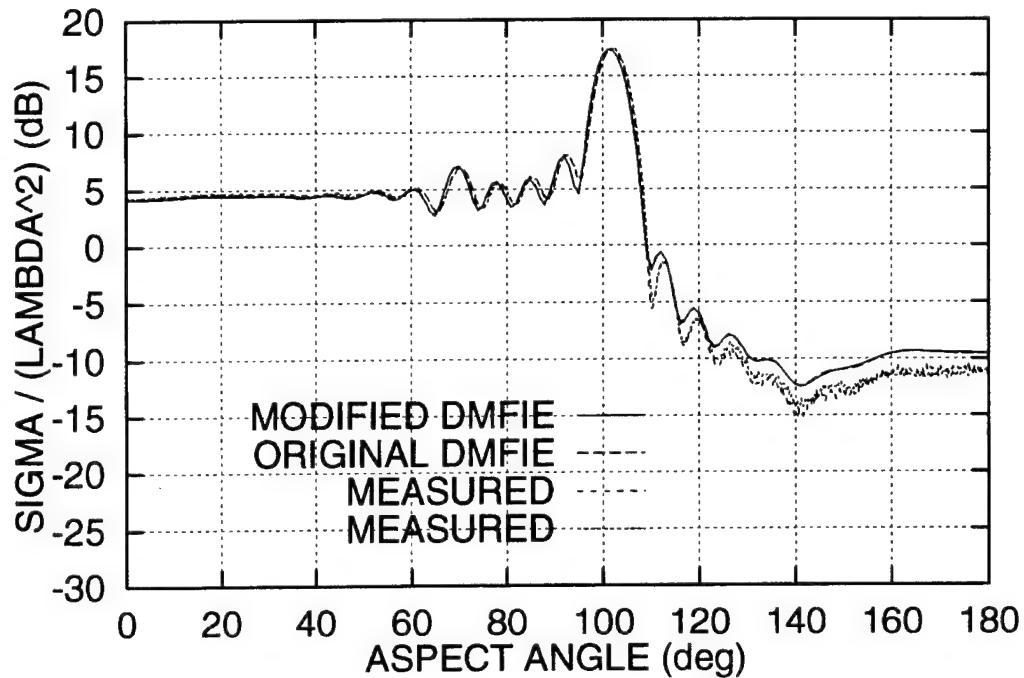
Figure 46. H-Plane Monostatic RCS for Conesphere for the Modified DMFIE using j_ν Current Dependence, Original DMFIE, and Measurements; $ka = 5.87$.
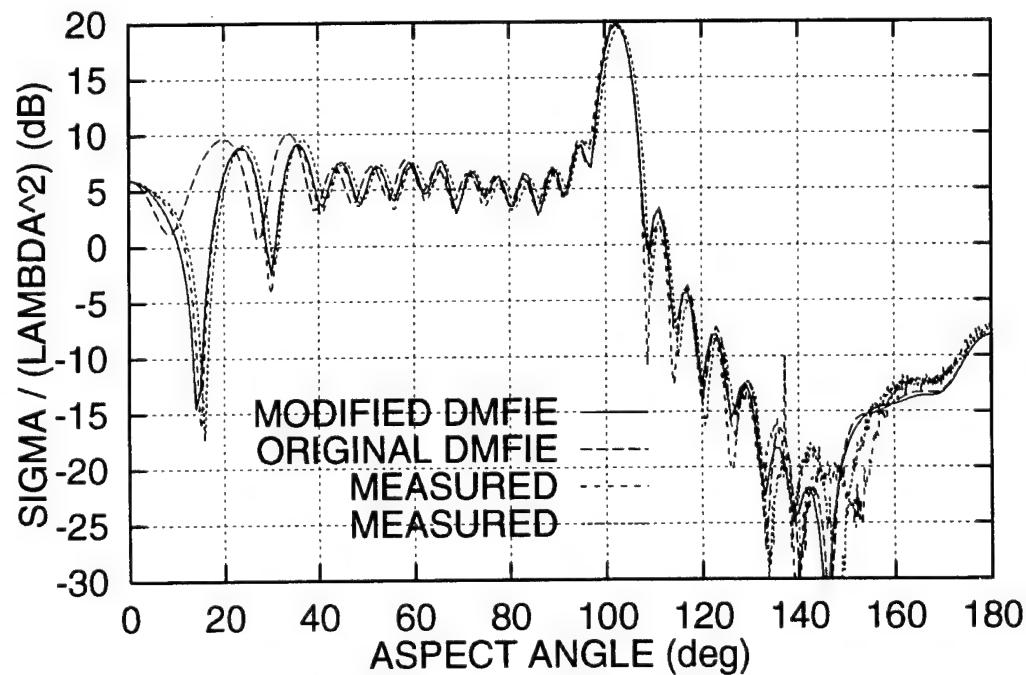
Figure 47. E-Plane Monostatic RCS for Conesphere for the Modified DMFIE using j_ν Current Dependence, Original DMFIE, and Measurements; $ka = 6.86$.

41
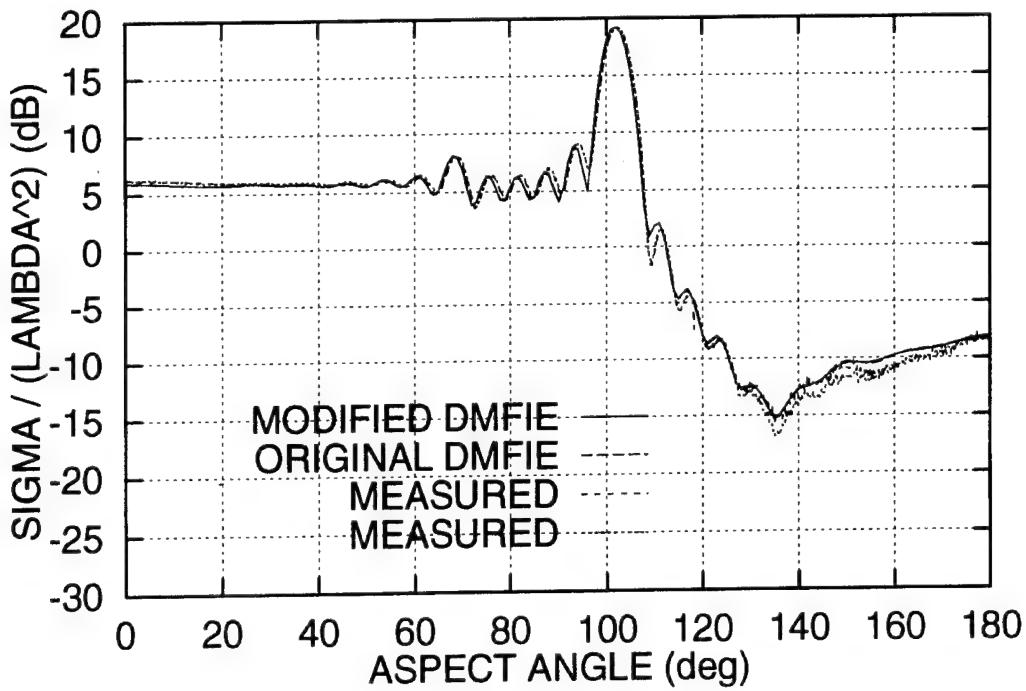
Figure 48. H-Plane Monostatic RCS for Conesphere for the Modified DMFIE using J_ν Current Dependence, Original DMFIE, and Measurements; $ka = 6.86$.
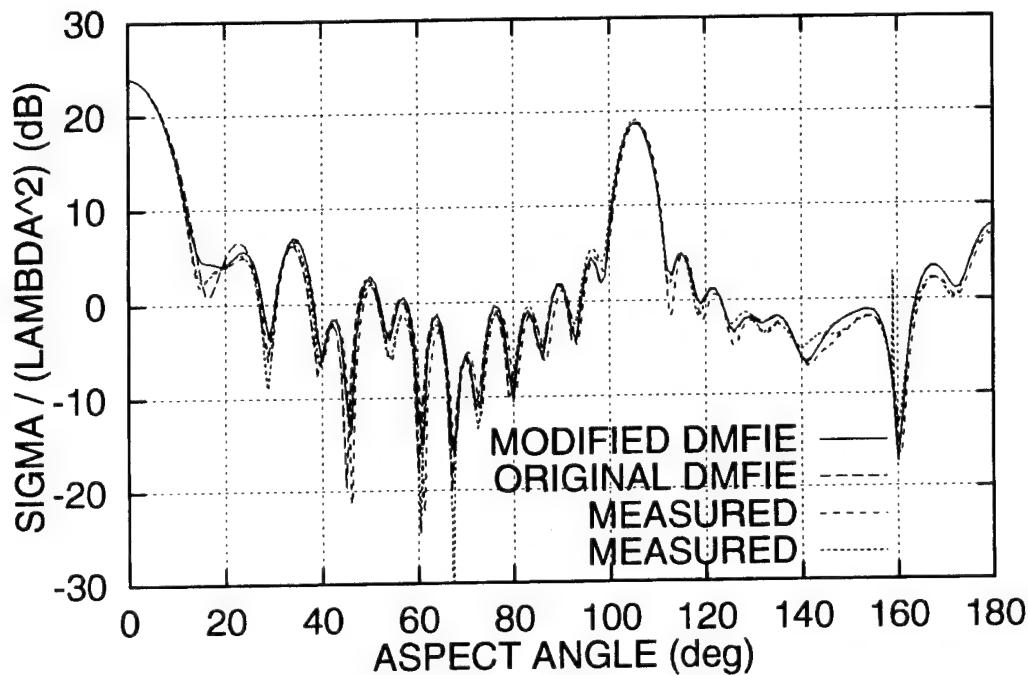
Figure 49. E-Plane Monostatic RCS for Flat-Backed Cone for the Modified DMFIE using J_ν Current Dependence, Original DMFIE, and Measurements; $a = 1.18\lambda$, $l = 4.33\lambda$, $\alpha = 15.26°$.
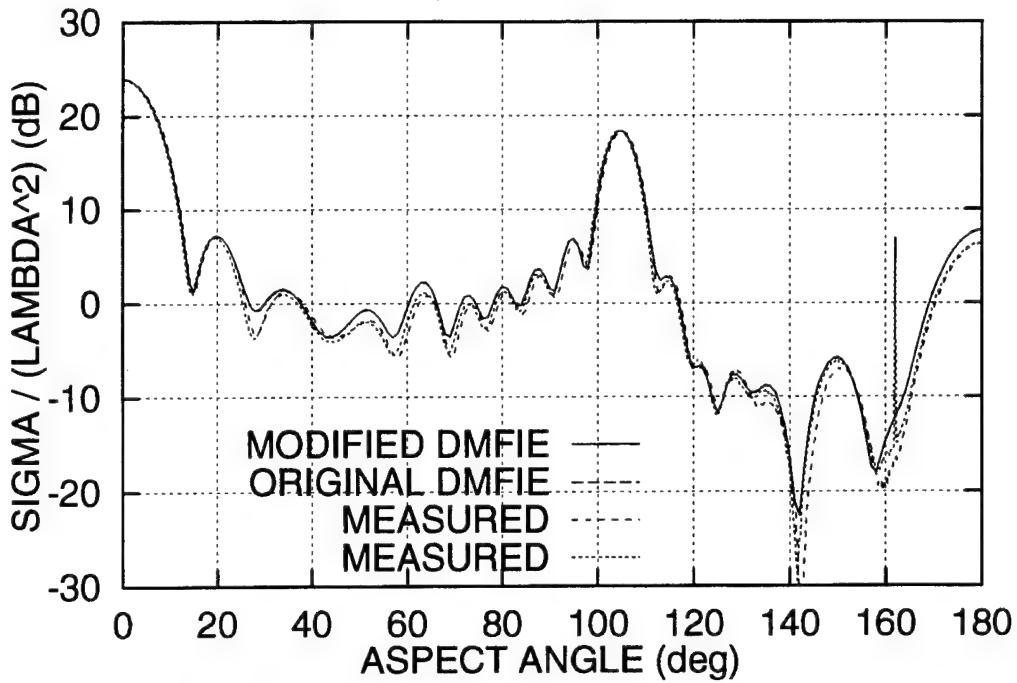
Figure 50. H-Plane Monostatic RCS for Flat-Backed Cone for the Modified DMFIE using j_ν Current Dependence, Original DMFIE, and Measurements; $a = 1.18\lambda$, $l = 4.33\lambda$, $\alpha = 15.26°$.
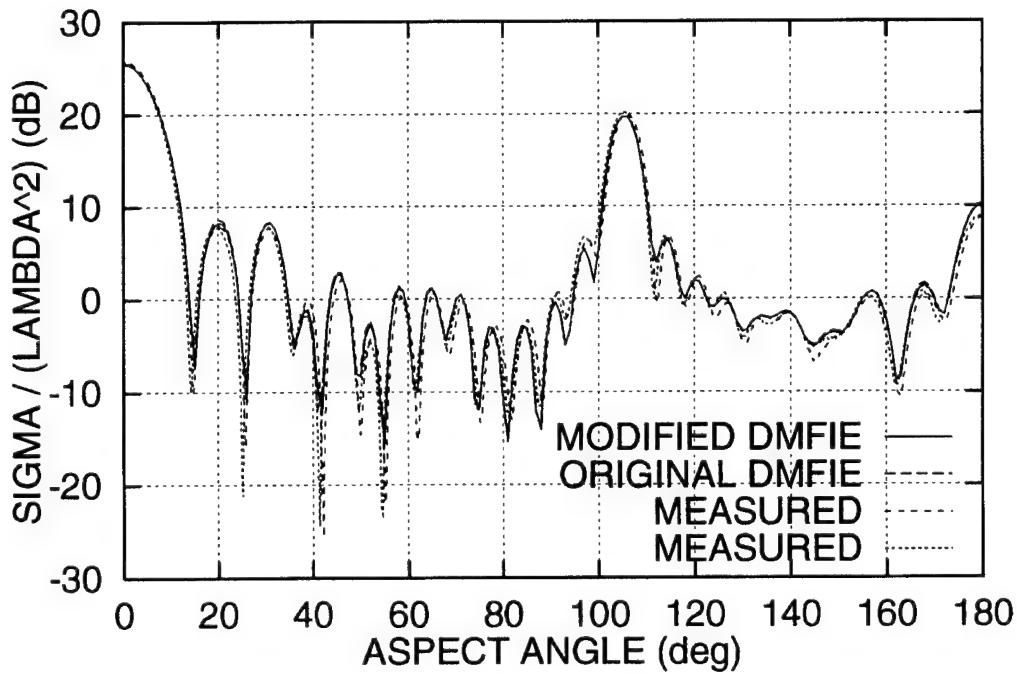
Figure 51. E-Plane Monostatic RCS for Flat-Backed Cone for the Modified DMFIE using j_ν Current Dependence, Original DMFIE, and Measurements; $a = 1.29\lambda$, $l = 4.72\lambda$, $\alpha = 15.26°$.

43
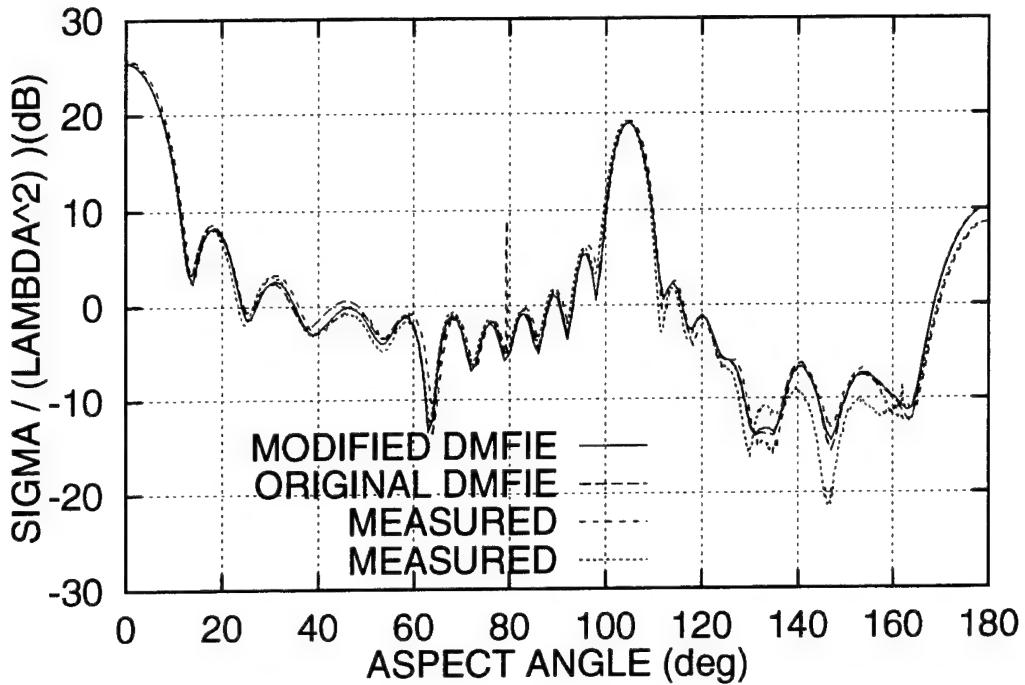
Figure 52. H-Plane Monostatic RCS for Flat-Backed Cone for the Modified DMFIE using j_ν Current Dependence, Original DMFIE, and Measurements; $a = 1.29\lambda$, $l = 4.72\lambda$, $\alpha = 15.26°$.
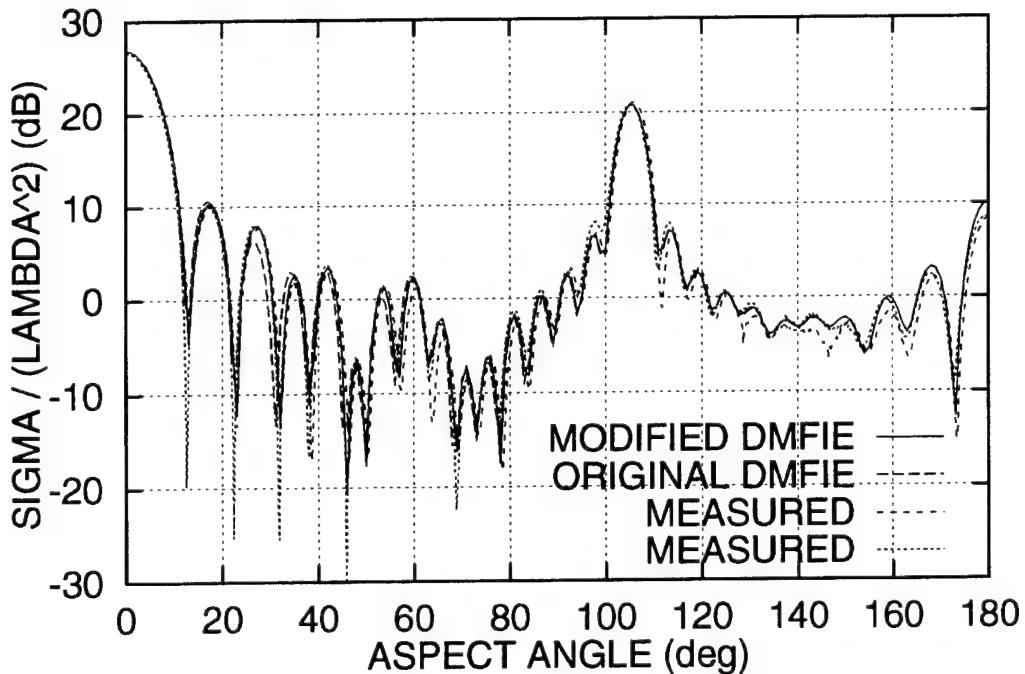
Figure 53. E-Plane Monostatic RCS for Flat-Backed Cone for the Modified DMFIE using j_ν Current Dependence, Original DMFIE, and Measurements; $a = 1.39\lambda$, $l = 5.11\lambda$, $\alpha = 15.26°$.
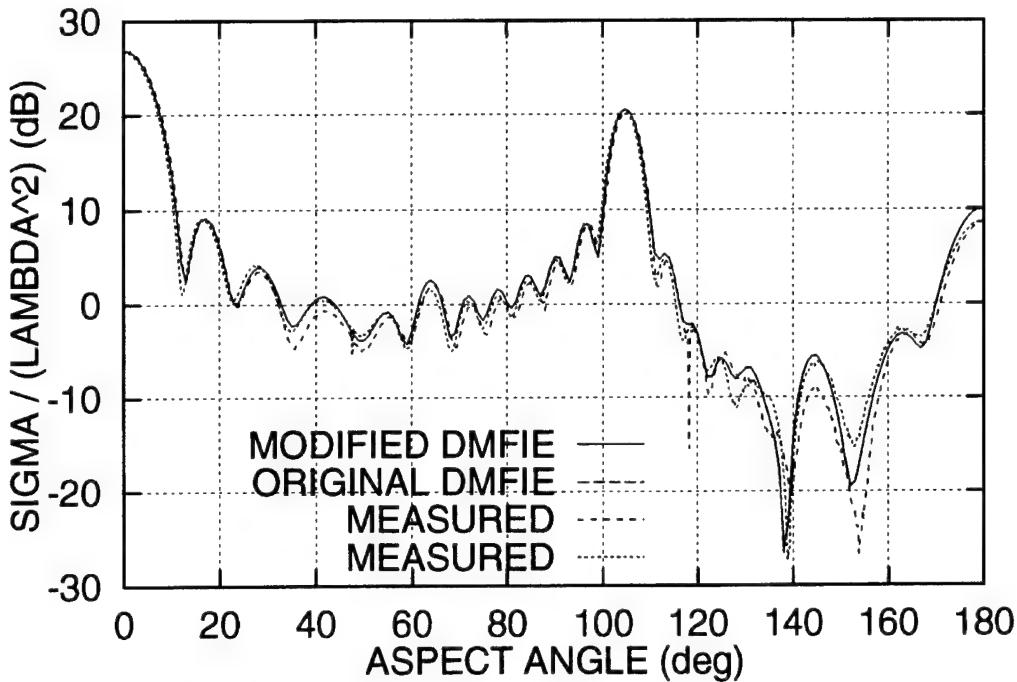
Figure 54. H-Plane Monostatic RCS for Flat-Backed Cone for the Modified DMFIE using j_ν Current Dependence, Original DMFIE, and Measurements; $a = 1.39\lambda$, $l = 5.11\lambda$, $\alpha = 15.26°$.
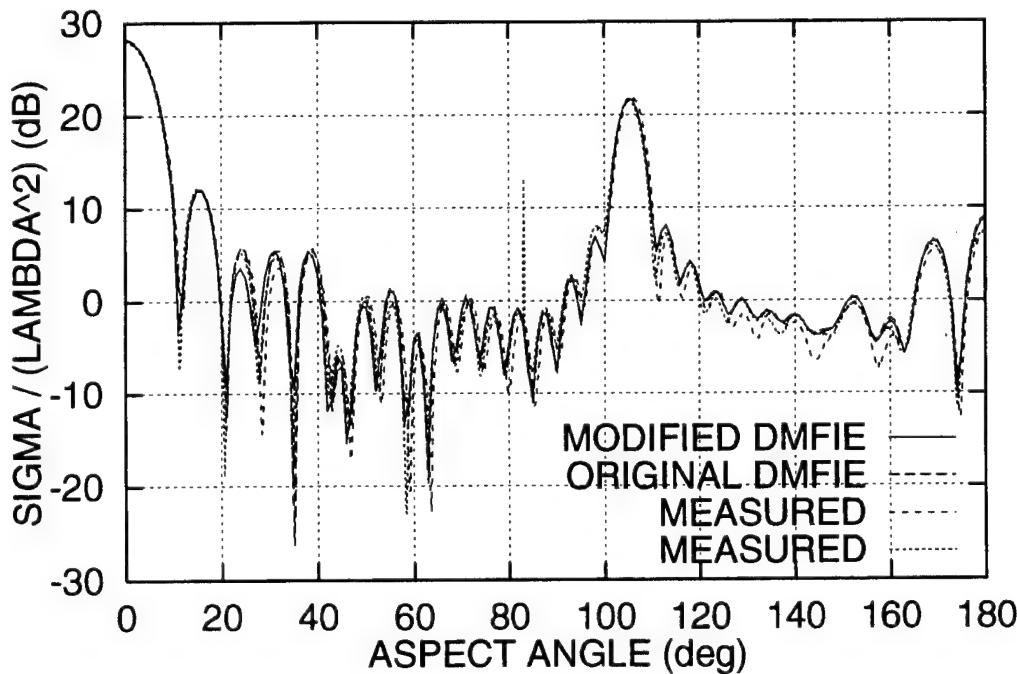

Figure 55. E-Plane Monostatic RCS for Flat-Backed Cone for the Modified DMFIE using j_ν Current Dependence, Original DMFIE, and Measurements; $a = 1.5\lambda$, $l = 5.51\lambda$, $\alpha = 15.26°$.
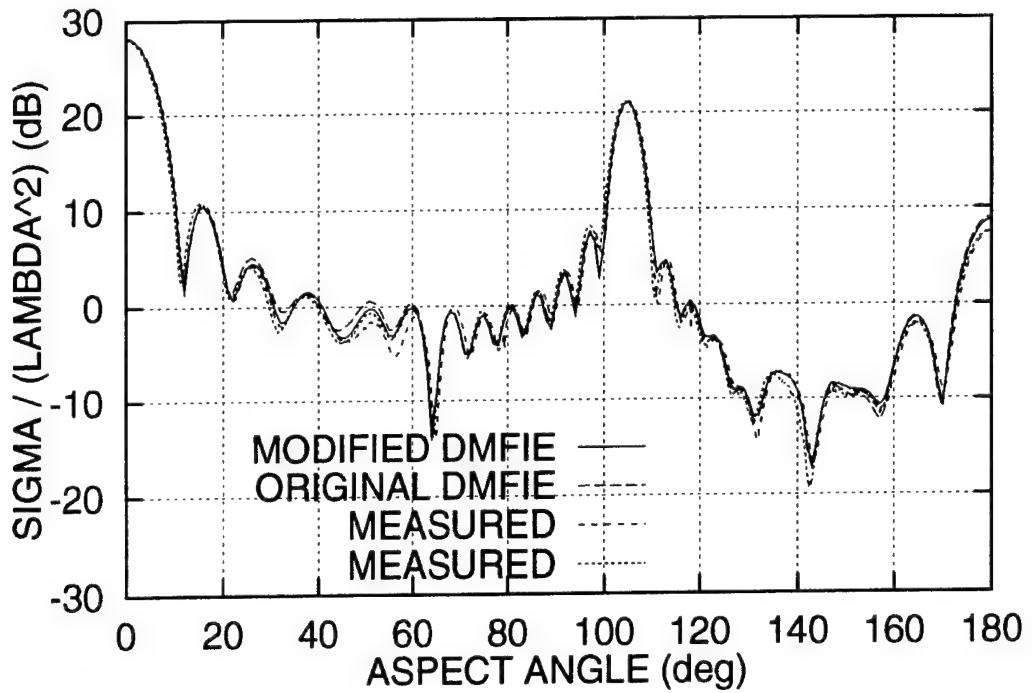
Figure 56. H-Plane Monostatic RCS for Flat-Backed Cone for the Modified DMFIE using j_ν Current Dependence, Original DMFIE, and Measurements; $a = 1.5\lambda$, $l = 5.51\lambda$, $\alpha = 15.26°$.
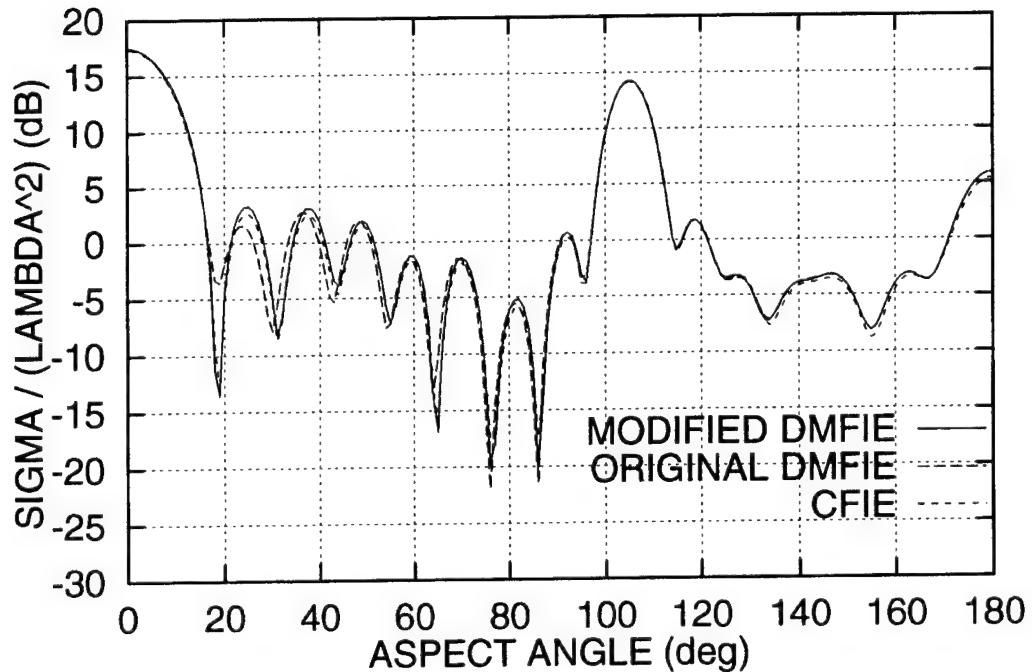

Figure 57. E-Plane Monostatic RCS for Flat-Backed Cone for the Modified DMFIE using j_ν Current Dependence, Original DMFIE, and CFIE; $a = 0.808\lambda$, $l = 3.042\lambda$, $\alpha = 15°$.
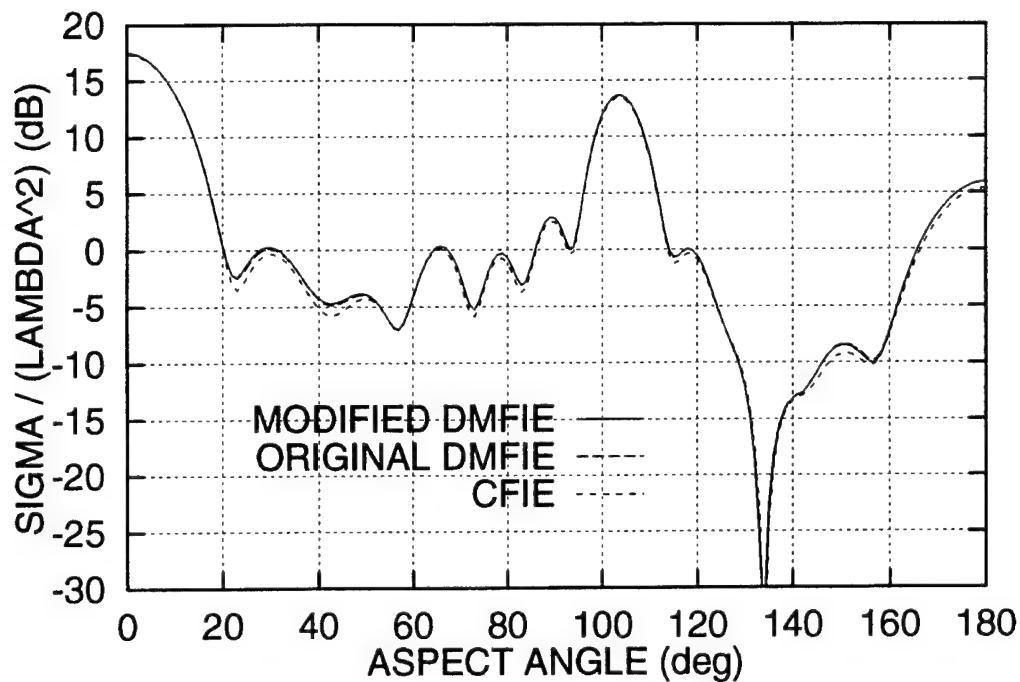
Figure 58. H-Plane Monostatic RCS for Flat-Backed Cone for the Modified DMFIE using j_ν Current Dependence, Original DMFIE, and CFIE; $a = 0.808\lambda$, $l = 3.042\lambda$, $\alpha = 15°$.
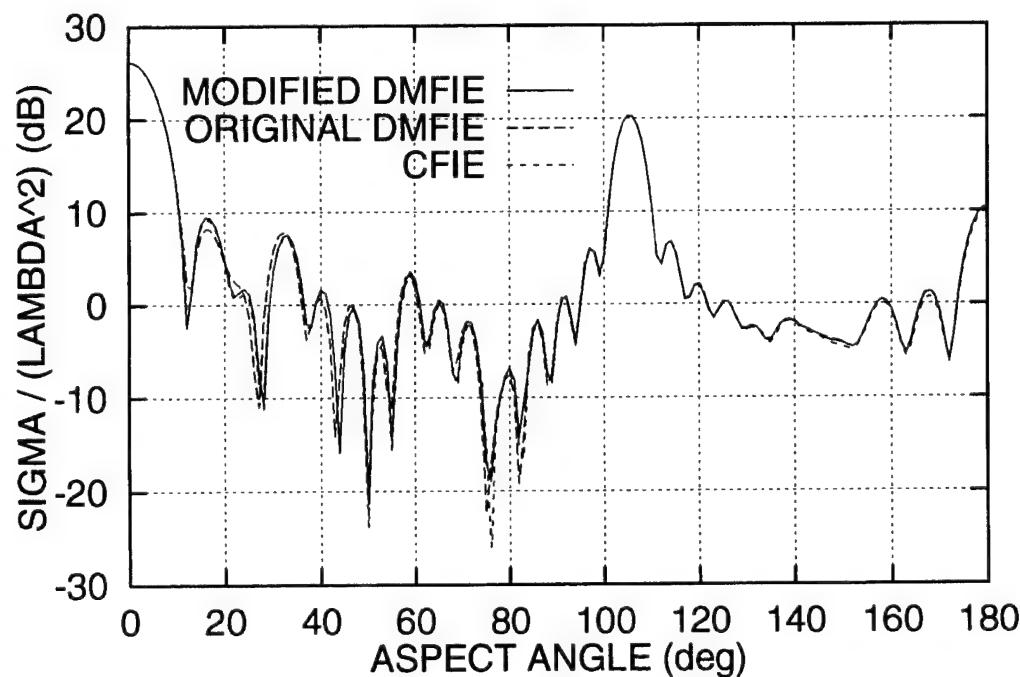

Figure 59. E-Plane Monostatic RCS for Flat-Backed Cone for the Modified DMFIE using j_ν Current Dependence, Original DMFIE, and CFIE; $a = 1.342\lambda$, $l = 4.921\lambda$, $\alpha = 16°$.
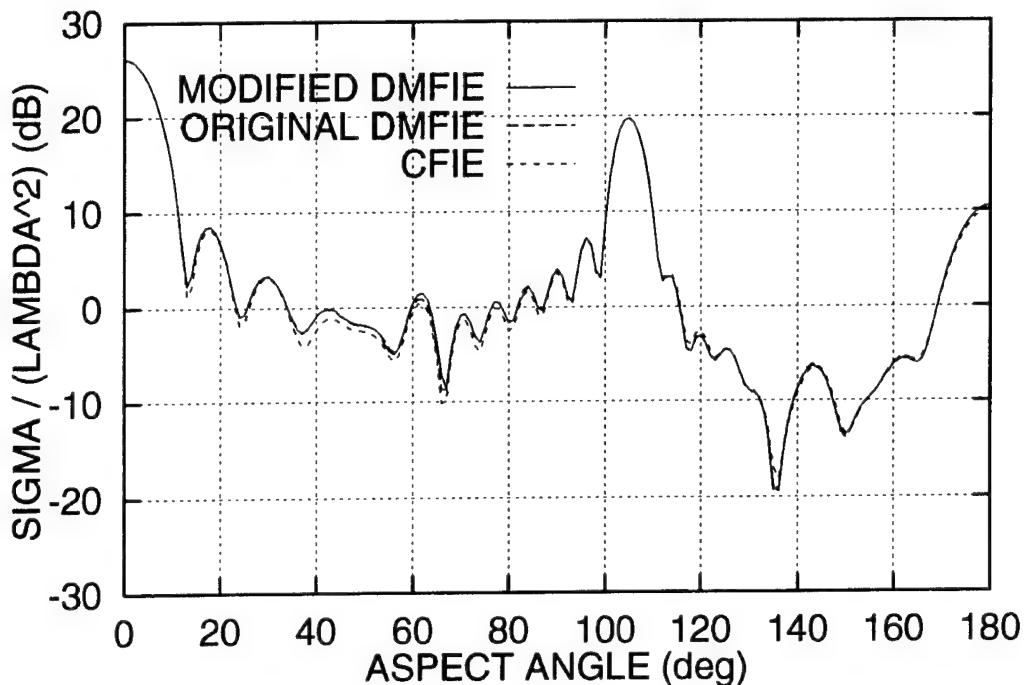
Figure 60. H-Plane Monostatic RCS for Flat-Backed Cone for the Modified DMFIE using j_ν Current Dependence, Original DMFIE, and CFIE; $a = 1.342\lambda$, $l = 4.921\lambda$, $\alpha = 16°$.
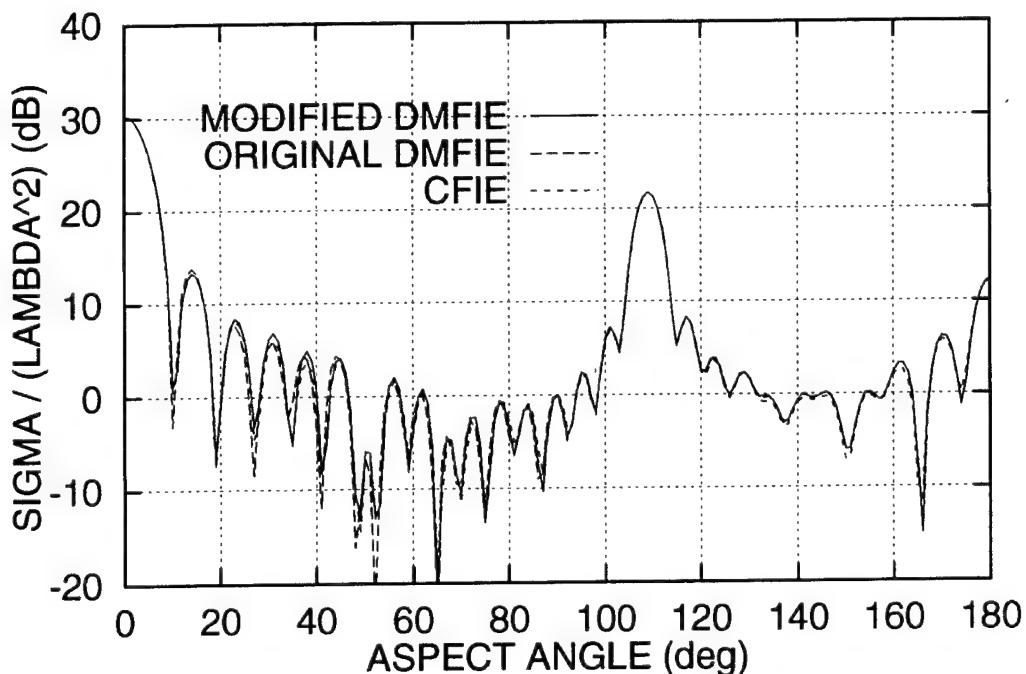

Figure 61. E-Plane Monostatic RCS for Flat-Backed Cone for the Modified DMFIE using j_ν Current Dependence, Original DMFIE, and CFIE; $a = 1.71\lambda$, $l = 5.0\lambda$, $\alpha = 20°$.
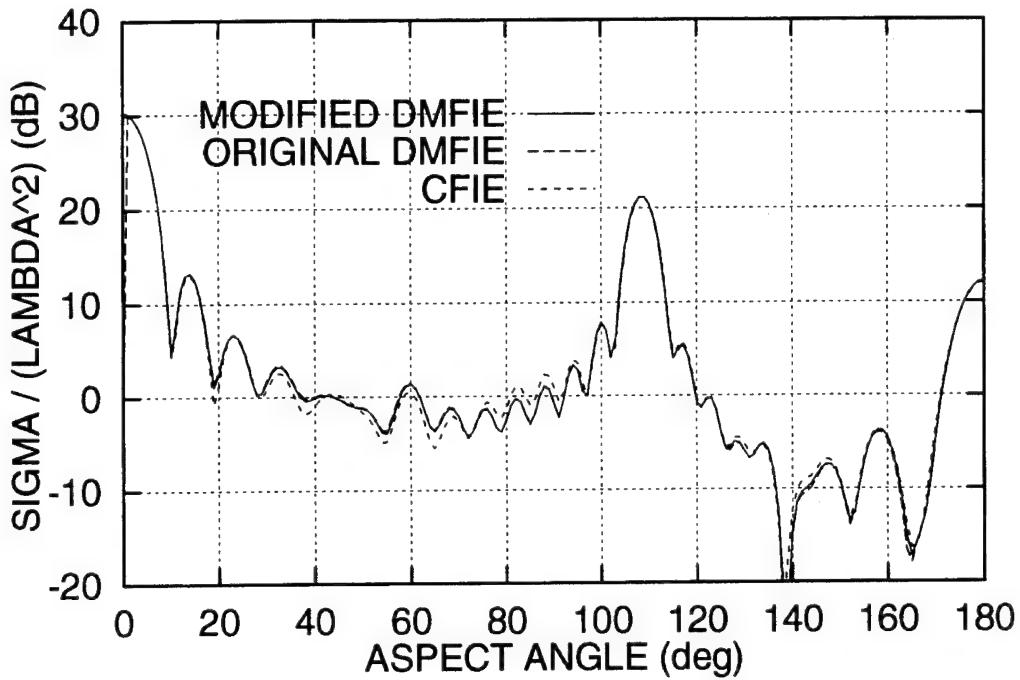
Figure 62. H-Plane Monostatic RCS for Flat-Backed Cone for the Modified DMFIE using j_ν Current Dependence, Original DMFIE, and CFIE; $a = 1.71\lambda$, $l = 5.0\lambda$, $\alpha = 20°$.
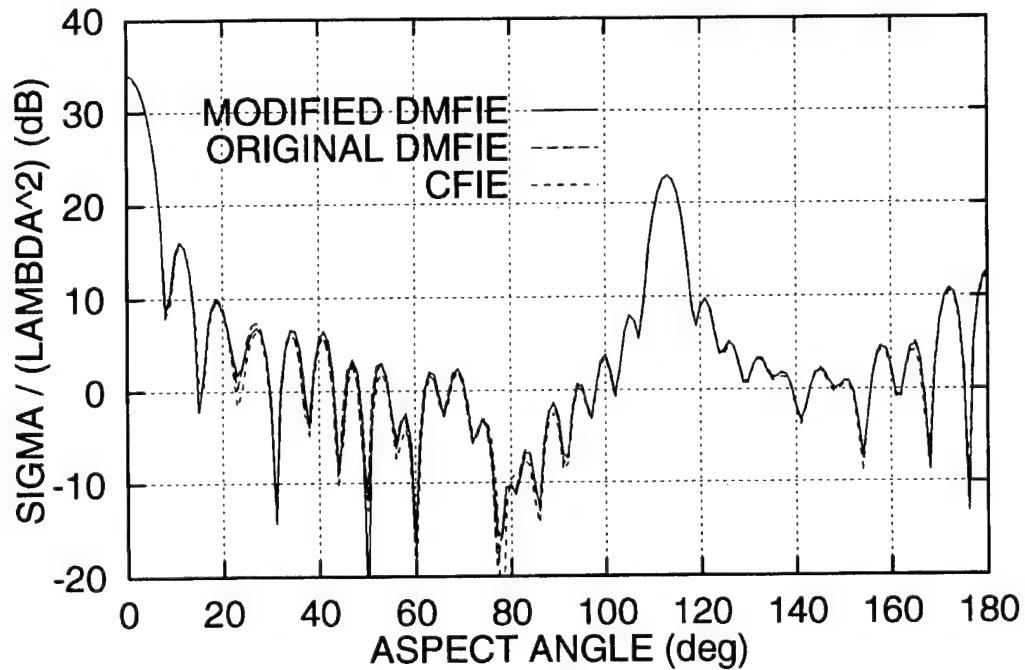
Figure 63. E-Plane Monostatic RCS for Flat-Backed Cone for the Modified DMFIE using j_ν Current Dependence, Original DMFIE, and CFIE; $a = 2.11\lambda$, $l = 5.0\lambda$, $\alpha = 25°$.
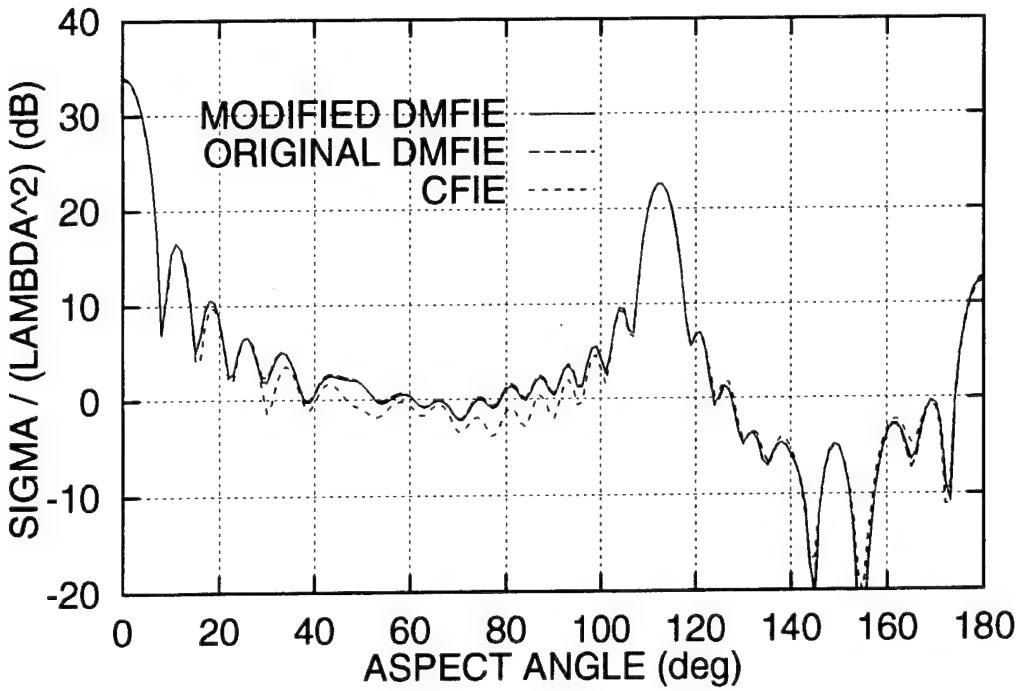
Figure 64. H-Plane Monostatic RCS for Flat-Backed Cone for the Modified DMFIE
using j_ν Current Dependence, Original DMFIE, and CFIE; $a = 2.11\lambda$, $l = 5.0\lambda$, $\alpha = 25°$.
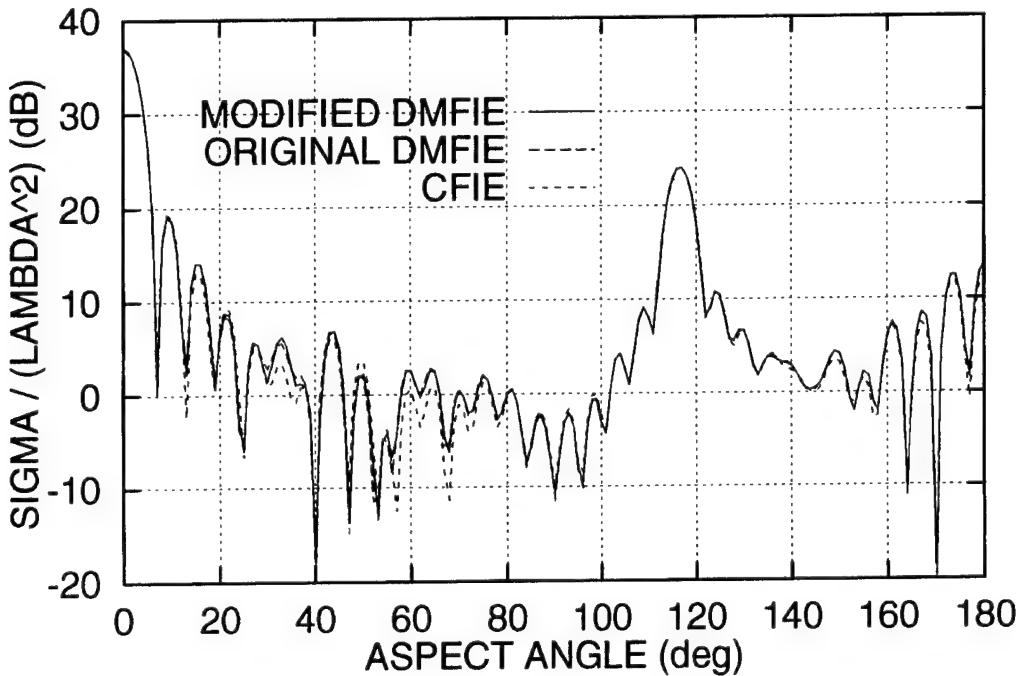
Figure 65. E-Plane Monostatic RCS for Flat-Backed Cone for the Modified DMFIE
using j_ν Current Dependence, Original DMFIE, and CFIE; $a = 2.5\lambda$, $l = 5.0\lambda$, $\alpha = 30°$.
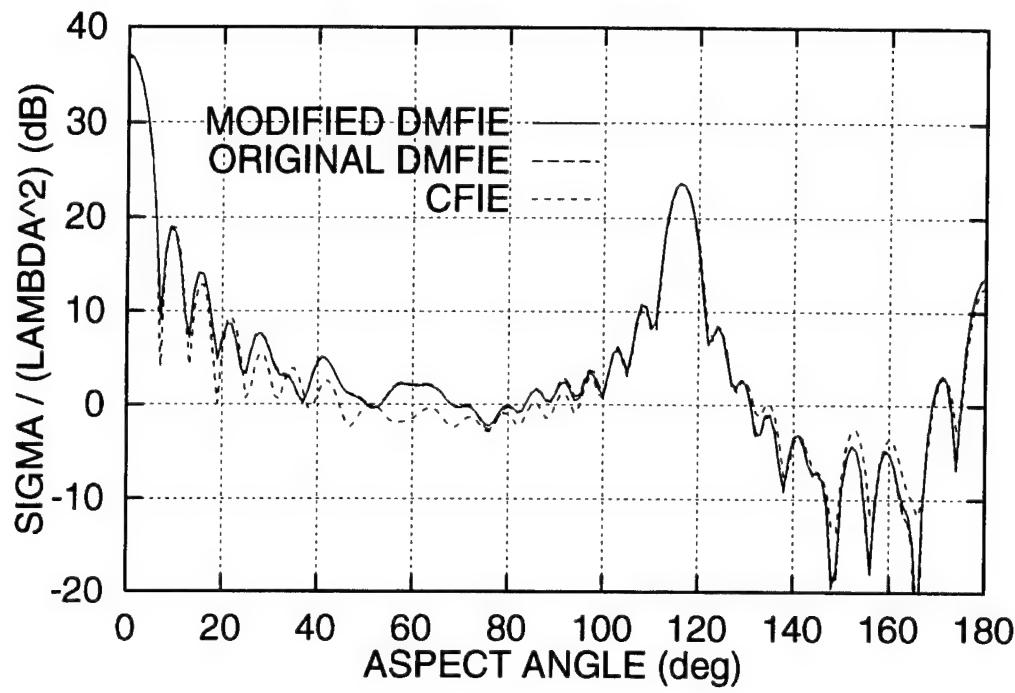
Figure 66. H-Plane Monostatic RCS for Flat-Backed Cone for the Modified DMFIE using j_ν Current Dependence, Original DMFIE, and CFIE; $a = 2.5\lambda$, $l = 5.0\lambda$, $\alpha = 30°$.

7 CONCLUSIONS

It was shown that the DMFIE eliminates the spurious resonances from the MFIE for plane wave scattering from bodies of revolutions. The results were excellent for as few as seven segments per wavelength for the right circular cylinder, using simple pulse basis and impulse testing functions.

The reduction of total solution time of electrically large bodies of revolution by the FFT and CG method is clearly demonstrated. The solution times using Gaussian elimination were proportional to $(d/\lambda)^3$ for axial incidence for a scatterer with equal width and length, and proportional to $(d/\lambda)^4$ for broadside incidence. For broadside incidence, the FFT reduced the matrix fill time from a $(d/\lambda)^4$ to a $(d/\lambda)^3 \log_2(d/\lambda)$ functional dependence, and the use of the CG iterative method reduced the solution time from $(d/\lambda)^4$ to $(d/\lambda)^3$. Therefore, the total computer time required for electrically large bodies of revolution is proportional to $(d/\lambda)^3$ for axial incidence and $(d/\lambda)^3 \log_2(d/\lambda)$ for broadside incidence. However, use of the FFT increased the amount of computer storage required from a $(d/\lambda)^2$ proportionality to a $(d/\lambda)^3$ proportionality.

It was demonstrated that the MFIE and the original DMFIE do not correctly produce the dominant current for scatterers with narrow tips and therefore gave incorrect results for scatterers with narrow tips. By inserting the exact tip current near the tip of an infinite cone into the DMFIE computer program, the DMFIE was made to accurately calculate the scattering from bodies with narrow tips. This allows the DMFIE to be applied to bodies of revolution with much narrower tips than the original DMFIE solution and thus increases the number of scatterers to which it can be applied. This improved solution for cone tips has been incorporated into the original DMFIE computer program in a way that is transparent to the user.

Our future plans are to implement the dual-surface electric-field integral equation for perfectly conducting bodies·of revolution. The dual-surface electric-field integral equation would serve as an independent check on the solution to bodies of revolution and would allow us to compute the RCS from infinitesimally thin conductors for which the DMFIE cannot be applied.

References

1. Murray, F.H. (1931) Conductors in an electromagnetic field, *Am. J. Math.*, **53**:275-288.

2. Maue, A.W. (1949) On the formulation of a general scattering problem by means of an integral equation, *Zeitschrift fur Physik*, **126(7/9)**:601-618.

3. Yaghjian, A.D. (1981) Augmented electric and magnetic field integral equation, *Radio Science*, **16**:987-1001.

4. Tobin, A.R., Yaghjian, A.D., and Bell M.M. (1987) Surface integral equations for multi-wavelength, arbitrarily shaped, perfectly conducting bodies, *Digest of the National Radio Science Meeting*, (URSI), Boulder CO

5. Woodworth, M.B., and Yaghjian, A.D. (1991) Derivation, application and conjugate gradient solution of the dual-surface integral equations for three-dimensional, multi-wavelength perfect conductors, in *PIERS-5: Applications of the Conjugate Gradient Method to Electromagnetic and Signal Analysis*, Sarkar, T.K. and Kong, J.A., eds., Elsevier, ch. 4. Also, *J. Opt. Soc. Am. A*, **11**, April 1994.

6. Mautz, J.R. and Harrington, R.F. (1987) H-field, E-field, and combined-field solutions for bodies of revolution, *Arch. Elecktron. Ubertragungstech. (Electron. Commun.)*, **32(4)**:157-164.

7. Schmitz, J.L. (1991) *Dual-Surface Magnetic-Field Integral Solution for Bodies of Revolution*, RL-TR-91-139, Hanscom AFB, MA, ADA260725.

8. Yaghjian, A.D. (1977) *Near Field Antenna Measurements on a Cylindrical Surface: A Source Scattering Matrix Formulation*, NBS Technical Note 696.

9. Waterman, P.C. (1965) Matrix formulation of electromagnetic scattering, *Proc. IEEE*, **53**:805-812.

10. Gedney, S.D. and Mittra, R. (1990) The use of the FFT for the efficient solution of the problem of electromagnetic scattering by a body of revolution, *IEEE Trans. Antennas Propagat.*, **AP-38**:313-322.

11. Sarkar, T.K., and Arvas, E. (1985) On a class of finite step iterative methods (conjugate directions) for the solution of an operator equation arising in electromagnetics, *IEEE Trans. Antennas Propagat.*, **AP-22**:1058-1066.

12. Poggio, A.J., and Miller, E.K. (1987) Solution of Three-Dimensional Scattering

Problems, in *Computer Techniques for Electromagnetics*, Mittra, R., ed., Springer-Verlag, p. 168.

13. Sadasiv, M.R., Wilton, D.R., and Glisson, A.W. (1982) Electromagnetic Scattering by Surfaces of Arbitrary Shape, *IEEE Trans. Antennas Propagat.*, **AP-30**:409-418.

14. Glisson, A.W., and Wilton, D.R., (1980) Simple and Efficient Methods for Problems of Electromagnetic Radiation and Scattering from Surfaces, *IEEE Trans. Antennas Propagat.*, **AP-28**:593-603.

15. Sancer, M.I., McClary, R.L., and Glover, K.J. (1990) Electromagnetic Computation using Parametric Geometry, *Electromagnetics*, **10**:85-103.

16. Phone discussion with D. Wilton, University of Houston, Houston, TX.

17. Larose, C. and Shantnu, M., of David Florida Laboratory, Canadian Space Agency, Ottawa, Ontario, performed the RCS measurements. One measurement was performed from $0 - 360°$ in aspect angle, but the symmetry of the conesphere allows the measurement data from $180 - 360°$ to be plotted from $0 - 180°$ aspect angle.

18. Wing, R. and Cote, M., of Rome Laboratory, Hanscom AFB, Ma, performed a second set of measurements on the conesphere.

19. Putnam, J.M. and Medgyesi-Mitschang, L.N. (1987) *Combined Field Integral Equation Formulation for Axially Inhomogeneous Bodies of Revolution*, McDonnell Douglas Corporation Report No. QA003, Volume I: Final Technical Report, St. Louis, MO., Sandia National Laboratory Contract No. 33-4257.

20. This approach was suggested by J.M. Putnam of McDonnell Douglas Research Laboratories, St. Louis, MO.

21. Van Bladel, J. (1983) Field singularities at the tip of a cone, *Proc. IEEE*, **71**:901-902.

22. DeSmedt, R. and Van Bladel, J. (1986) Fields at the tip of a metallic cone of arbitrary cross section, *IEEE Trans. Antennas Propagat.*, **34**:865-870.

23. Jackson, J.D. (1975) *Classical Electrodynamics*, Wiley, New York, 2nd ed., pp. 94-102.

24. Trott, K.D. (1986) *A High Frequency Analysis of Electromagnetic Plane Wave Scattering by a Fully Illuminated Perfectly Conducting Semi-Infinite Cone*, Dissertation at Ohio State University, Columbus, Ohio.

25. Hall, R.N. (1949) The application of non-integral Legendre functions to potential problems, *Journal of Applied Physics*, **20**:925-931.

26. Abramowitz, M. and Stegun, I.A. (1972) *Handbook of Mathematical Functions*, NBS

Appendix A

Dominant Term of Electrostatic Tip Current Variation for the Cone

The potential ϕ is expanded in spherical harmonics,

$$\phi(R, \theta, \phi) = \sum_{m=0}^{\infty} \sum_{\nu} A_{m\nu} P_\nu^m(\cos\theta) \begin{Bmatrix} \cos m\phi \\ \sin m\phi \end{Bmatrix} R^\nu. \tag{A1}$$

The value of the subscript ν is determined from the requirement that ϕ vanish on the cone, which leads to the condition

$$P_\nu^m(\cos\theta_0) = 0. \tag{A2}$$

Only the zero order mode ($m = 0$) is of interest as this is the mode that gives the incorrect current value.

Van Bladel in Reference 21 presents two singularities, the electric and magnetic. The electric field of the electric singularity is not bounded as is the magnetic field. The outward normal crossed into the magnetic field results in a current in the t–direction (u_R direction in Reference 21). The radial distance from the tip of the cone is t (R in Reference 21). The current varies as t^ν where ν is the degree of the Legendre function in Eq. (A2).

The right-hand side of Eq. (13) for the $\hat{u}_t$ component of J^t, J^{tt}, can be written as

$$J^{tt}(t, t', \phi') = J_{ave} \int dt' \int_0^{2\pi} d\phi' B g t' r^{1.5} \tag{A3}$$

where

$$g = (1 + jkr), \tag{A4}$$
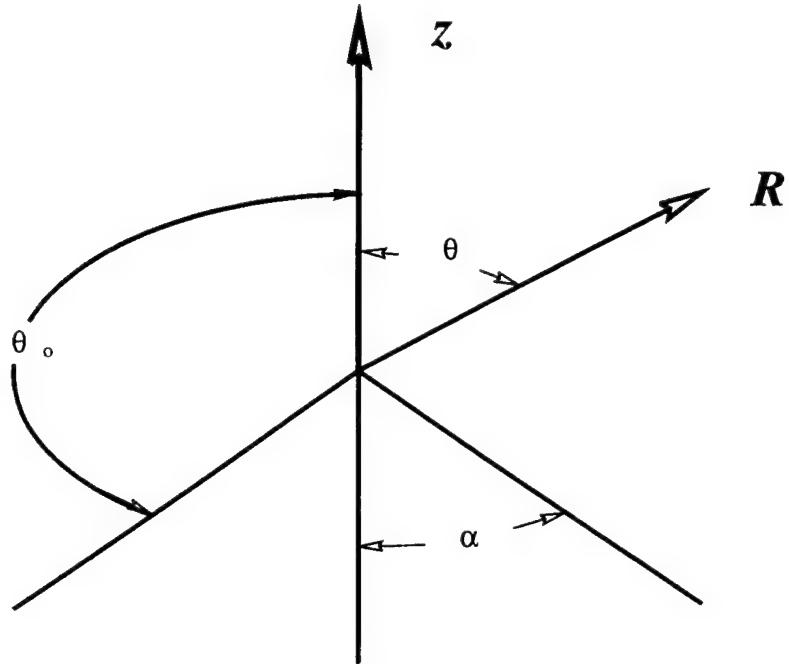
Figure A1. Geometry for Cone.

$$r = (t'^2 + t'tA + t^2) \tag{A5}$$

$$A = \{4\sin^2(\alpha)\sin^2(\phi'/2) - 2\} \tag{A6}$$

and

$$B = \frac{-t\sin^2(\alpha)\cos(\alpha)\sin^2(\phi'/2)}{2\pi}. \tag{A7}$$

This assumes that the last patch on the tip of the cone is small and the current can be approximated by the electrostatic case. Letting the current on this patch be J_{ave} times the length of the patch in the $t-$direction

$$J_{ave}\triangle t = \int_0^{\triangle t} J dt = a \int_0^{\triangle t} t^\nu dt = \frac{t^{\nu+1}}{\nu+1} \Big|_0^{\triangle t}. \tag{A8}$$

Therefore

$$a = \frac{(\nu + 1)J_{ave}}{(\triangle t)^{\nu}} \tag{A9}$$

and

$$J = \frac{\nu + 1}{(\triangle t)^{\nu}}t^{\nu}J_{ave} \tag{A10}$$

Using Eq. (A10) in Eq. (A8) one obtains

$$J^{tt} = J_{ave}\frac{\nu + 1}{(\triangle t)^{\nu}} \int dt' t'^{\nu} \int_0^{2\pi} d\phi' Bgt'r^{1.5} \tag{A11}$$

which now can be substituted into the right-hand side of Eq. (13). The value of ν can be determined from the asymptotic formula

$$\nu = \frac{1}{2\ln\left(\frac{2}{\alpha}\right)}. \tag{A12}$$

Appendix B

Dominant Term of Tip Current Variation for the Semi-Infinite Cone

Starting with Eq. (4.48) in Reference 24

$$J_{sR}^{\phi'}(R_0) =$$

$$\frac{jk^2}{2\pi}\left[\sum_p \frac{\epsilon_m h_\nu^{(2)}(kd)}{\nu(\nu+1)I_{m\nu}}\left\{\begin{matrix} S(\nu,m,\beta)\cos m\phi \\ T(\nu,m,\beta)\sin m\phi \end{matrix}\right\}\left\{J_\nu'(kR_0) + \frac{J_\nu(kR_0)}{kR_0}\right\}\frac{mP_\nu^m(\cos\theta_0)}{(\sin\theta_0)}\right. \quad \text{(B1)}$$

$$\left. -\sum_q \frac{\epsilon_m J_\gamma(kR_0)}{\gamma(\gamma+1)I_{m\gamma}}\left\{\begin{matrix} T(\gamma,m,\beta)\cos m\phi \\ S(\gamma,m,\beta)\sin m\phi \end{matrix}\right\}\left\{h_\gamma^{(2)\prime}(kd) + \frac{h_\gamma^{(2)}(kd)}{kd}\right\}\frac{d}{d\theta}P_\gamma^m(\cos\theta_0)\right]$$

where the geometry for the semi-infinite cone and the application of a point source are shown in Figures B1 and B2. The radial distance from the cone tip is R_0 and the incident angle β is chosen such that $0 \le \beta < \theta_0 = \pi - \alpha$, where α is the cone half-angle. We are solving only for the E-plane, $t-$directed current for mode zero. This reduces Eq. (B1) to

$$J_{sR}^{\theta'}(R_0) =$$

$$\frac{-jk^2}{2\pi}\left[\sum_q \frac{J_\gamma(kR_0)}{\gamma(\gamma+1)I_{0\gamma}}\left\{T(\gamma,0,\beta)\right\}\left\{h_\gamma^{(2)\prime}(kd) + \frac{h_\gamma^{(2)}(kd)}{kd}\right\}\frac{d}{d\theta}P_\gamma^0(\cos\theta_0)\right] \quad \text{(B2)}$$

where

$$T(\gamma,0,\beta) = \frac{\{P_\gamma^{-1}(\cos\beta)(\gamma-1)(\gamma) - P_\gamma^1(\cos\beta)\}}{2} \quad \text{(B3)}$$
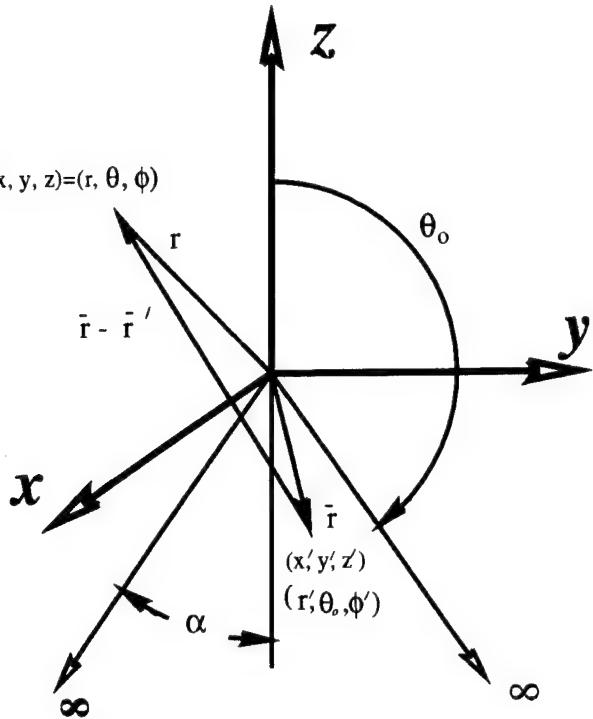
Figure B1. Geometry for semi-infinite cone.[23]

$$I_{0\gamma} = \int_0^{\theta_0} d\theta [P_\gamma^0(\cos\theta)]^2 \sin\theta \tag{B4}$$

$$q = \gamma \tag{B5}$$

and gamma is the value of the zeros for the solution of $P_\gamma(\cos\theta_0) = 0$. The source will be placed in the far field. This facilitates the use of the large argument form of the Hankel function given by

$$\lim_{x\to\infty} h_\nu^{(2)}(x) \to j^{\nu+1}\left(\frac{e^{-jx}}{x}\right) \tag{B6}$$

and therefore

$$\lim_{kR\to\infty} [kRh_\nu^{(2)}(kR)]' \to j^\nu\left(\frac{e^{-jkR}}{kR}\right). \tag{B7}$$

The solution is now specialized to the case of plane wave incidence by moving the point source far away and letting

$$E^i = jkZ_c\frac{e^{-jkd}}{4\pi d} \tag{B8}$$

60
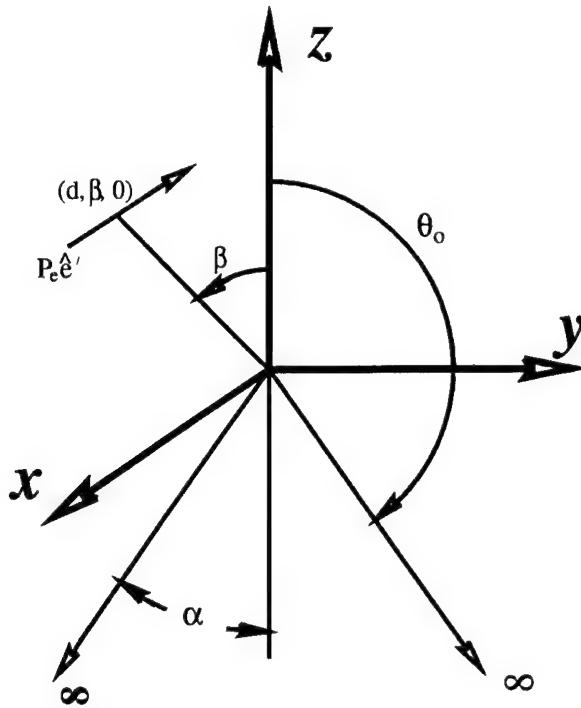
Figure B2. Geometry for application of dipole moment.[23]

Applying this to Eq. (B2)

$$J_{sR}^{\theta'}(R_0) = -2Y_0\left(\sum_{\gamma} \frac{\jmath_\gamma(kR_0)(2\gamma+1)\jmath^\gamma\{d/d\beta[P_\gamma^0(\cos\beta)]\}}{\gamma(\gamma+1)\sin\theta_0\{d/d\gamma[P_\gamma^0(\cos\theta_0)]\}}\right).$$ (B9)

The numerical solution of Eq. (B9) requires the evaluation of Eq. D.15 in Reference 24, a recursion relationship for Legendre polynomials, at $m = 0, \theta = \beta$, and $\nu = \gamma$, yielding

$$\frac{d}{d\beta}P_\nu(\cos\beta) = \frac{(\gamma+1)P_{\gamma+1}(\cos\beta) - (\gamma+1)P\gamma(\cos\beta)}{\sin\beta}.$$ (B10)

Differentiating Eq.(D.13) in Reference 24, an integral equation representation for the associated Legendre polynomial, with respect to gamma and evaluating at $m = 0, \theta = \theta_0$, and $\nu = \gamma$, is also necessary for the evaluation of Eq. (B9) and results in

$$\frac{\partial}{\partial\gamma}P_\gamma(\cos\theta_0) = \frac{\sqrt{2}}{\pi}\int_0^\theta \frac{-\sin[(\gamma+.5)x]}{(\cos x - \cos\theta)^{(.5)}}dx.$$ (B11)

The substitution of Eqs. (B10) and (B11) into Eq. (B9) facilitates its numerical evaluation.

The first zero can be determined from Eq. (A12), tables[25] or computer programs. The third approach was used for a cone half-angle α of $12.5°$ resulting in $\nu_0 = 0.226$, $\nu_1 = 1.326$,

---

[25] Hall, R.N. (1949) The application of non-integral Legendre functions to potential problems, *Journal of Applied Physics*, **20**:925-931.
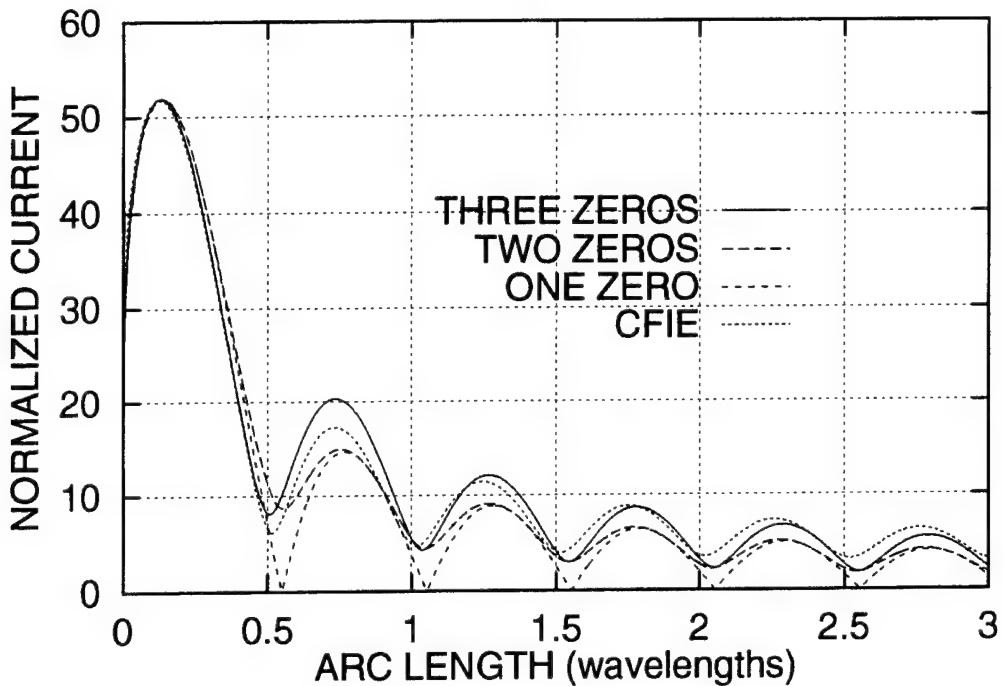
Figure B3. Amplitude of the E-Plane Current From the Semi-Infinite Cone Formulation for Three Zeros and CFIE Solution for Conesphere for an Arc Length of Three Wavelengths; $ka = 6.36$, $\theta_t = 20°$.

and $\nu_2 = 2.415$. Figs. B3 and B4 show the current that results using the first three values of ν in Eq. (B9) compared with the CFIE solution of the conesphere at $\alpha = 12.5$ and $\theta_t = 20°$. The semi-infinite solution using three zeros is the best fit to the CFIE at a distance of approximately one-half wavelength from the tip of the body. It would seem that one should use this solution, but further investigation shows that Eq. (B9) for multiple values of ν is a function of cone and incident angles with a complex phase. This requires the use of only one ν in solving Eq. (B9) and Figure B4 shows the agreement to be acceptable to the first maximum of the current.
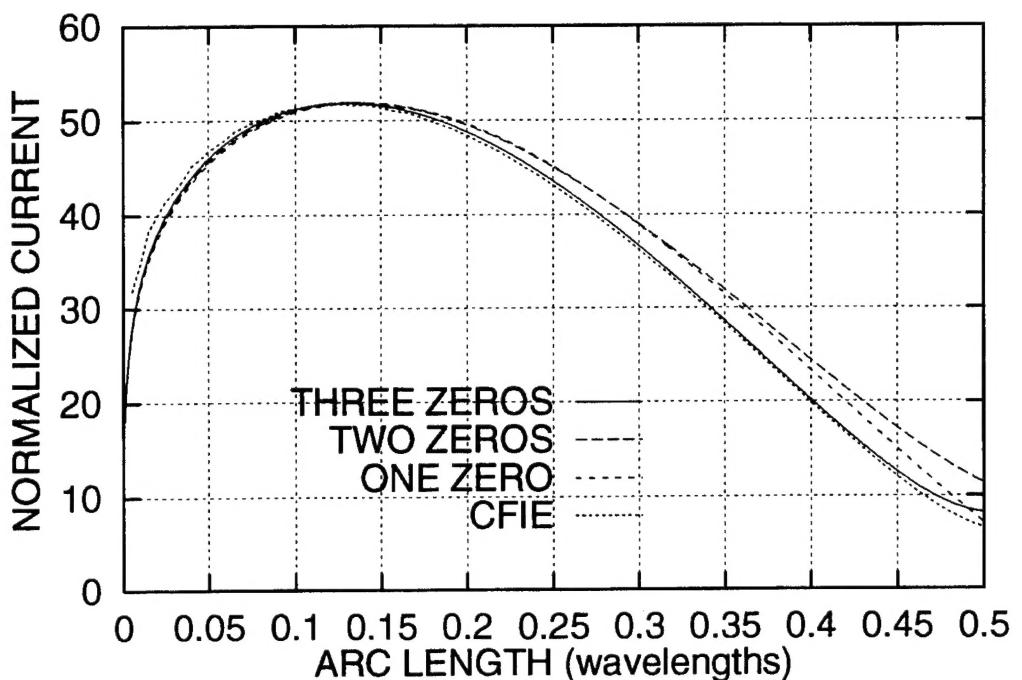
Figure B4. Amplitude of the E-Plane Current From the Semi-Infinite Cone Formulation for Three Zeros and CFIE Solution for Conesphere for an Arc Length of One-Half Wavelength; $ka = 6.36$, $\theta_t = 20°$.

First Maximum of Spherical Bessel Function

The need for the maximum of the Spherical Bessel function $j_\nu(z)$ was demonstrated in Appendix B. There are a number of available schemes to calculate the value of this function. We chose one that was computationally fast and easy to implement. We decided to use the series representation of $j_\nu(z)$[26] where

$$J_\nu(z) = (\frac{z}{2})^\nu \sum_{k=0}^{\infty} \frac{(-z^2/4)^k}{k!\Gamma(\nu+k+1)} \tag{C1}$$

and

$$j_n(z) = \sqrt{\frac{\pi}{2z}} J_{n+1/2}(z). \tag{C2}$$

Taking the first two terms of the series, we have

$$j_n(z) = (\frac{z}{2})^{(\nu+1/2)} \sqrt{\frac{\pi}{2z}} \left\{ \frac{1}{\Gamma(\nu+1.5)} - \frac{z^2}{4\Gamma(\nu+2.5)} \right\}. \tag{C3}$$

After some algebraic reduction

$$j_n(z) = \sqrt{\pi} \left\{ \frac{z^\nu}{2^{(\nu+1)}\Gamma(\nu+1.5)} - \frac{z^{(\nu+2)}}{\Gamma(\nu+2.5)2^{(\nu+3)}} \right\}. \tag{C4}$$

The derivative of $j_n(z)$ is defined as

---

[26] Abramowitz, M. and Stegun, I.A. (1972) *Handbook of Mathematical Functions*, NBS

$$j_n'(z) = \sqrt{\pi} \left\{ \frac{\nu z^{(\nu-1)}}{2^{(\nu+1)}\Gamma(\nu+1.5)} - \frac{(\nu+2)z^{(\nu+2)}}{\Gamma(\nu+2.5)2^{(\nu+3)}} \right\}. \tag{C5}$$

Set $j_n'(z)$ equal to zero and solve for z to get

$$z = \sqrt{\frac{\Gamma(\nu+2.5)4\nu}{(\nu+2)\Gamma(\nu+1.5)}} \tag{C6}$$

where z is the radial distance in wavelengths from the cone tip for our case.

MISSION

OF

ROME LABORATORY

Rome Laboratory plans and executes an interdisciplinary program in research, development, test, and technology transition in support of Air Force Command, Control, Communications and Intelligence (C^3I) activities for all Air Force platforms. It also executes selected acquisition programs in several areas of expertise. Technical and engineering support within areas of competence is provided to ESD Program Offices (POs) and other ESD elements to perform effective acquisition of C^3I systems. In addition, Rome Laboratory's technology supports other AFSC Product Divisions, the Air Force user community, and other DOD and non-DOD agencies. Rome Laboratory maintains technical competence and research programs in areas including, but not limited to, communications, command and control, battle management, intelligence information processing, computational sciences and software producibility, wide area surveillance/sensors, signal processing, solid state sciences, photonics, electromagnetic technology, superconductivity, and electronic reliability/maintainability and testability.